October 2022

Experimental Investigation of Clay Aggregate and Granular Biofilm Behavior

Tao Jiang
University of Massachusetts Amherst

Recommended Citation

Jiang, Tao, "Experimental Investigation of Clay Aggregate and Granular Biofilm Behavior" (2022). *Doctoral Dissertations*. 2638.
https://doi.org/10.7275/30957909 https://scholarworks.umass.edu/dissertations_2/2638

EXPERIMENTAL INVESTIGATION OF CLAY AGGREGATE AND GRANULAR BIOFILM BEHAVIOR

A Dissertation Presented

by

TAO JIANG

Submitted to the Graduate School of the
University of Massachusetts Amherst in partial fulfillment of
the requirements for the degree of

DOCTOR OF PHILOSOPHY

September 2022

Civil and Environmental Engineering

EXPERIMENTAL INVESTIGATION OF CLAY AGGREGATE AND GRANULAR BIOFILM BEHAVIOR

A Dissertation Presented

by

TAO JIANG

Approved as to style and content by:

Guoping Zhang, Chair

Andrew J. Whittle, Member

Ching S. Chang, Member

Shuang Zhou, Member

John E. Tobiason, Department Head
Department of Civil and Environmental
Engineering

ACKNOWLEDGMENTS

My sincerest gratitude first goes to my advisor, Prof. Guoping Zhang, who has been continuously supporting me for the past five years. His constant guidance was an indispensable part of completing my dissertation. I am extremely thankful for not only his enlightening on my academic path but also the advice about how to become a person with good citizenship, which encourages me to grow in the future. I am thankful to Prof. Andrew J. Whittle for his valuable advice and discussion throughout my research. His brilliant understanding of soil behavior and expertise in numerical simulation significantly inspires me and provides a lot of insights into my research. I would also like to extend my gratitude to my committee members, Prof. Ching S. Chang and Prof. Shuang Zhou for their valuable advice on my dissertation.

This research was generously funded by the U.S. National Science Foundation (NSF) under Award No. CMMI 1702881. Additional support from the Charles F. Perrell Scholarship was also gratefully acknowledged.

I would also like to thank all my past and present fellow students for their continuous help and advice throughout my research.

Finally, I would like to thank my parents, Shaoan Jiang and Guoqin Huang, for their unselfish love and unconditional patience during the tough times. I could not have completed my dissertation without their love and encouragement.

ABSTRACT

EXPERIMENTAL INVESTIGATION OF CLAY AGGREGATE AND GRANULAR BIOFILM BEHAVIOR

SEPTEMBER 2022

TAO JIANG, B.Sc., WUHAN UNIVERSITY OF ENGINEERING SCIENCE
M.S.C.E., UNIVERSITY OF MASSACHUSETTS AMHERST
Ph.D., UNIVERSITY OF MASSACHUSETTS AMHERST
Directed by: Professor Guoping Zhang

Clay minerals are a class of phyllosilicates as the major solid constituents in cohesive fine-grained soils (e.g., clays). Owing to their tiny size (i.e., < 2 μm), high aspect ratio, and active surface properties that inherit from the geological process, clay minerals can extensively interact with other suspended matter (e.g., exoployemers, microorganisms) and dissolved ions via the process of flocculation and aggregation, resulting in the formation of larger, porous cohesive particulate aggregates or flocs. Such a complex mechanism of microscale particle interaction generates significant challenges for understanding the bulk clay behavior as a particulate system. In order to better characterize the flocculation and aggregation of clay minerals under various stimuli and to understand the underlying mechanism of particle interactions, particle/aggregate size kinetics of flocculated suspensions of illite, a representative 2:1 clay mineral abundant in marine soils, are studied with varied ionic strength induced by monovalent salt (NaCl), pH, and hydrodynamic shearing in the first phase of this research. Furthermore, a new statistical data binning method termed "bin size index" (BSI) was employed to determine the probability density function (PDF) distributions of flocculated illite suspensions. The statistical results demonstrate that the size kinetics of flocculated illite suspensions is chiefly controlled by the face-to-face and edge-to-face interparticle interactions under the mutual effects of ionic strength and pH, while the hydrodynamic shearing has minimal effects on the variation of particle size groups.

In the second phase of this research, the mechanics of clay aggregates are studied using an innovative measurement technique and analytical approach. Individual clay minerals prepared with different mineralogy and salinities are tested via unconfined compression, which shows that the increasing ionic strength can improve the strength and stiffness of clay aggregates, which are further affected by the mineralogical compositions and dominant microfabric in different water chemistry.

In the final phase of this research, a collaborative study with an environmental engineer on an NSF CAREER project was conducted to investigate the mechanical behavior of macroscale, light-induced oxygenic granules (biofilm aggregates) using the same technique and analytics developed for the individual clay aggregates. The findings are expected to provide reference values to subsequent studies and engineering practices associated with the water treatment process

TABLE OF CONTENTS

Page

LIST OF TABLES

Page

LIST OF FIGURES

Page

CHAPTER 1

INTRODUCTION

1.1 Background

Soils as typical particulate materials are characterized by their highly complex internal structure which involves the microstructure of soil particles (soil fabric) as well as the specific interactions developing between individual soil particles through forces (e.g., friction, cohesion) (Mitchell and Soga 2005). This feature is further complicated by the inherent multiscale particle-size system ranging from micro-and meso- (O[10^{-6}]-O[10^{-5}]m) and macroscale (O[10^{-3}]-O[10^{-2}]m). As such, the macroscopic engineering properties of soils (e.g., consolidation, shearing and creep) essentially originate from the particle-level interactions at micro-sized or meso-sized scales under different external loading conditions. Based on the unique particulate nature of soils, numerous efforts have been made to investigate the soil behaviors by developing particle-based constitutive models at the micro- or mesoscale level. For cohesionless granular soils (i.e., sands and gravels with individual particle length scales of ~ mm), significant advances have been achieved on the development of micromechanics through both (1) numerical simulations, notably the Discrete Element Method (DEM) (Cundall and Strack 1979) for explicit modelling of particle-level interactions (e.g., interparticle contact forces, particle crushing); DEM analyses assume relatively simple constitutive laws (e.g., elastic Hertz contact and Coulomb friction) (L.Johnson 1985), and (2) experimental measurements involving uniaxial compression testing on individual particles or particle agglomerates (granular assembly composed of a group of individual particles). These experiments are used to obtain mechanical properties such as elastic modulus, yield strength, and crushing strength which in turn can be used as necessary input parameters for DEM simulation (e.g., mechanical properties of rigid spherical sub-particles and cementing strength for bonding these sub-particles to form an individual agglomerate as the object particle for modelling). Classical examples associated with the research procedures discussed above can be found from the work of Alshibli's research group (Alshibli et al. 2013; Cil and Alshibli 2012, 2014). In these studies, synchrotron microcomputed tomography (SMT), a non-destructive high-resolution imaging technique using high-energy X-ray transmission, was used for scanning each Ottawa quartz sand grain to generate a 3D map of the specimen which can then be used as the reference data for DEM validation and permits monitoring deformation behaviors of particles during compression at microscale level. As schematically shown in Figure 1.1, DEM simulations of single particle, column of three particles and laboratory-size specimen are performed based on the 3D renderings of sand particles from SMT images, generating images containing the contact force network distribution (CFND) after initial particle contact (Figure 1.1(a)), before particle fracture (Figure 1.1(b)), and after particle fracture (Figure 1.1(c)), of which the simulated data is further compared to the experimental results (Figure 1.1(d)) at different load levels. These results demonstrate that the fracture of sand originates from the tensile stress failure of compression-induced crack propagation due to the dominant tensile cracks developed in the bond breakage (BB) in the DEM agglomerates (shown in red in the CFND & BB part of Figure 1.1(c)).

In addition to the studies in terms of micromechanics of granular soils, significant amount of research has been conducted on the constitutive laws of index properties (i.e., limiting void ratios, particle size distribution, morphological properties) of granular soils as well, which indirectly provides insights into the development of micromechanical studies of granular soils (Chang et al. 2017, 2018; Zheng and Hryciw 2016).

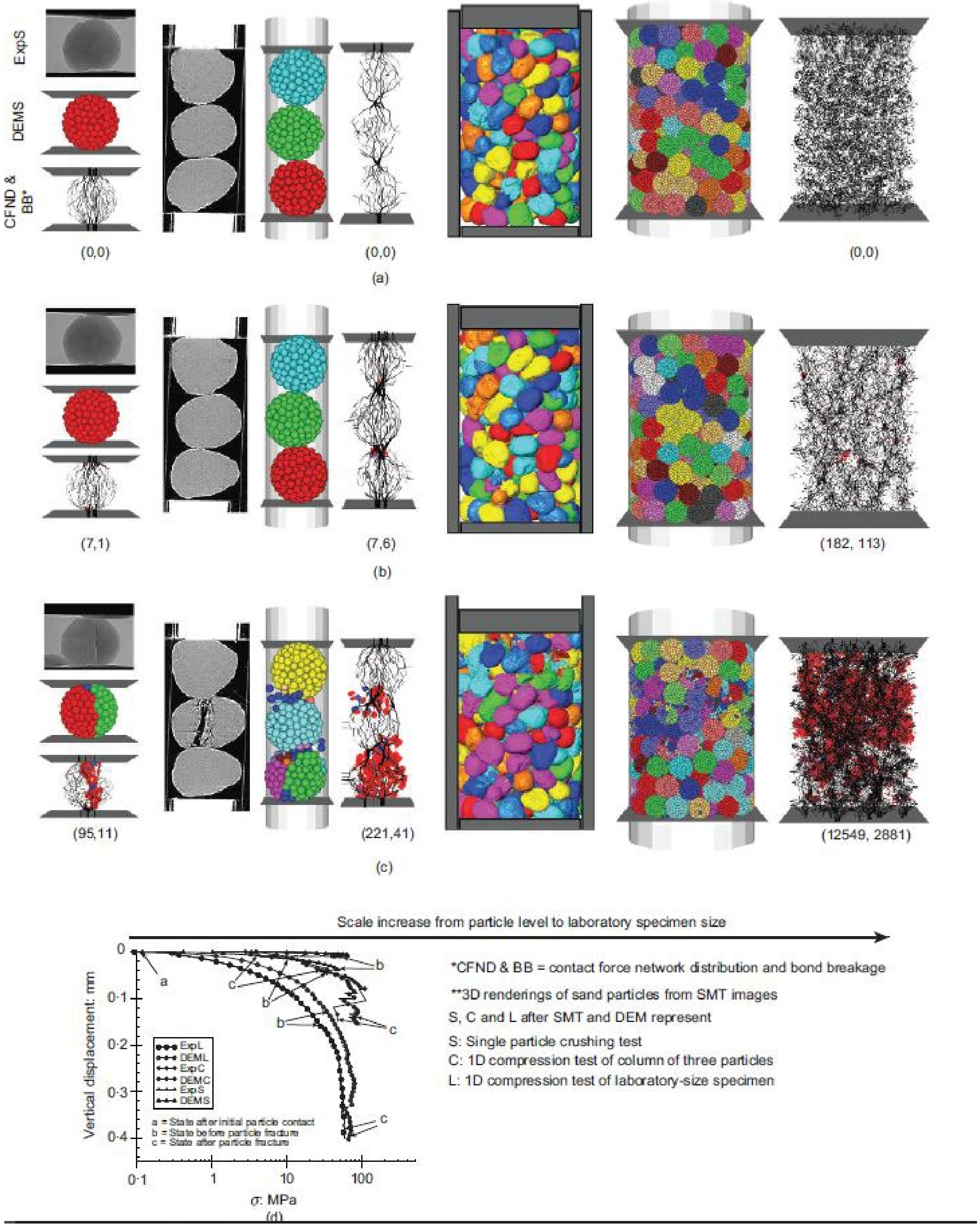

Figure 1.1 SMT and DEM images of single sand particle, column of three sand particles and laboratory-size compression tests captured at different load levels (Cil and Alshibli 2012)

In comparison with the intensive and successful works on granular soils, however, much less progress has been achieved in understanding the behavior of fine-grained cohesive soils (clays) as a particulate system. A brief explanation for this difference follows. Compared with cohesionless granular soils which have low specific surface area (SSA), relatively mineral compositions (basically quartz/silica sands), and simple interparticle force fields (monopolized by coulomb frictions), clays are characterized by their diverse particle size and shape for primary particles (smaller than 2 μm) with high SSA so that direct mechanical testing on the individual clay particles is challenging, and various mineral compositions with chemically active surface properties (e.g., inherent surface charge caused by crystal defects and isomorphous substitutions) which results in complex surface/interfacial interactions with water and ions to form electrical double layer in natural aquatic environments, thus making numerical simulations more difficult on modelling the clay-water-ions systems than that conducted on the granular soils (Bergaya and Lagaly 2006; Çelik 2004). Given this fact, the active microscale surface interactions and resulting clay microstructures need to be considered to develop new particulate-based understandings of clay behavior. As mentioned above, the chemically active surface properties of clay particles impart their extensive potentials of interacting with a variety of substances through transport/sedimentation in natural aquatic environments, leading to a change in particle size and microstructure by forming group of clay particles with wide range of size ranging from 0.2 μm to > 200 μm (aggregation/flocculation) associated with face-to-face or face-to-edge particle arrangements, depending upon the environmental flowing and chemistry conditions (i.e., hydrodynamic flow energy, the types and concentrations of dissolved salts or ions, pH) (Verwey and J. T. G. Overbeek 1955). As such, the large-sized clay particles (> 50 μm) with certain microstructures formed via small-scale surface/interfacial forces can be used as the basic structural unit (e.g., aggregate) that characterizes the microscale properties of clays.

In summary, sands and clays are both typical particulate materials whose macroscopic engineering properties are determined by the micro- and meso-level particle interactions. Even though encouraging understandings have been developed on sands, more efforts are still needed on the development of clay behavior as a particulate system, which warrants a systematic study to characterize the multiscale properties of clay and unravel the underlying mechanisms.

1.2 Research Objectives

The primary goal of this research is to understand the underlying mechanism of flocculation and aggregation of clay minerals under various environmental stimuli using newly developed data analytics, and to characterize the mechanical properties of clay aggregates and light-induced, oxygenic granules that can be regarded as a type of macroscale biofilm aggregates. Specific research objectives are as follows:

- Develop a new data binning method to accurately measure the statistical distribution obtained from multiscale, composite materials such as clay aggregates.
- Characterize the size kinetics of flocculated suspensions of clay minerals under various environmental stimuli and understand the underlying mechanism of particle interaction modes.

- Measure the mechanical properties of individual clay particles and understand the effects of mineralogical compositions, water chemistry, and microfabric patterns on the behavior of clay aggregates.
- Measure the mechanical properties of macroscale biofilm aggregates, which is also an examination process of the method newly developed for the individual clay aggregates.

1.3 Dissertation Organization

The dissertation consists of eight chapters and is formatted as a series of standalone papers. A brief outline of each chapter is given below:

(1) Chapter 1 (current chapter) is an introduction to this research, including the background, research objectives, and dissertation organization.

(2) Chapter 2 summarizes a comprehensive review of the clay minerals and their interactions that form a group of clay particles (i.e., clay aggregate) as the basic structural unit of soft clays, followed by the techniques and analytics on such structural unit. The background of the granular biofilms is also summarized in this chapter.

(3) Chapter 3 presents a new data binning method developed for the characterization of the particle size distribution of multiscale, composite materials. In this chapter, a rational histogram was constructed by selecting the optimal bin size of this new method, leading to the determination of the PDF for accurate statistical measurements in the future. This paper was submitted to the Annals of Applied Statistics.

(4) Chapter 4 presents the kinetics of particle size distributions of flocculated illite suspensions using the new method developed in Chapter 3 to construct the PDF of suspensions under various environmental stimuli, including ionic strength, pH, and hydrodynamic shearing. This paper has been accepted by the Applied Clay Science.

(5) Chapter 5 presents a systematic experimental study of individual clay aggregate's mechanics using newly developed technique and data analytics. Different mineralogical compositions were used to prepare individual clay aggregates under a series of saltwater that accounts for the ionic strength. Interpretation of microfabric patterns of clay aggregates under these conditions were also conducted.

(6) Chapter 6 presents an experimental study on the mechanical behavior of light-induced oxygenic granules whose formation process is very close to that of the clay aggregates. The measurement techniques and data analytics developed in Chapter 5 were employed in this study.

(7) Chapter 7 is a concluding chapter that summarizes the significant findings of this dissertation research and provides recommendations for future research on the behavior of clay aggregates and granular biofilms.

CHAPTER 2

LITERATURE REVIEW

This chapter includes a summary of the literature that was conducted for this dissertation. Firstly, the literature review begins with the general introductions of structure and property of clay minerals, and definitions of clay aggregates, flocs, and clusters. In the following section, previous studies on the stability of clay flocs in aqueous system are particularly reviewed and discussed, and methods for measuring particle size distributions (PSDs) of clay flocs, together with a general review of microstructure of clay flocs investigated by indirect measurement and direct observation techniques. Next, a systematic review on the methods and techniques that have been conducted on the strength of clay aggregates and granular biofilms are presented and discussed.

2.1 Clay Minerals, Aggregates, Flocs, and Clusters

2.1.1 General Structure and Properties of Clay Minerals

Considerable investigations have been conducted on the research of clay minerals because of their prevalence in fine-grained suspended sediment, cohesive soils and rocks (i.e., clay minerals are the major solid constituents of these geomaterials), and their great significance in various environmental , industrial, and domestic applications (e.g., water quality monitoring, oil well drilling, environmental abatement, clay-polymer nanocomposites, nanoclay catalysts) (Bergaya and Lagaly 2006; Harvey and Murray 1997; Kiliaris and Papaspyrides 2010; Walling and Moorehead 1989). As the dominant constituents of the phyllosilicate family of minerals, clay minerals are composed of diverse group of hydrous layer aluminosilicates with primarily two basic structural units, i.e., Si-O tetrahedron and Al-OH octahedron which are mainly involved with the coordination of Si^{4+} with three basal oxygen atoms and that of Al^{3+} with six hydroxyl groups, respectively. Two main crystalline sheets for clay minerals are herein formed, i.e., Si-O tetrahedral sheet is formed through linkage of one tetrahedron to three neighboring tetrahedrons by sharing three basal oxygen atoms, while Al-O octahedral sheet is formed through connection of one octahedron with adjacent units by sharing edges (Brigatti et al. 2006). Then, two types of sheet arrangements (layer) are formed, namely TO (1:1) layer with all the free apical oxygen atoms of tetrahedral sheet pointing to octahedral sheet and TOT (2:1) layer with all the unshared corners of each tetrahedral sheet pointing toward each other and connecting to each face of octahedral sheet. Finally, individual clay particles with specific types of layer are formed by the repetitious stacking and combination of each individual clay layer via interlayer/intermolecular forces such as hydrogen bonding (H-bonding), Coulomb forces, electrostatic attraction, and van der Waals forces (Figure 2.1).

Apart from their sophisticated crystalline structures, the featuring properties of clay minerals are also key factors rendering the unique characteristics of clay minerals. One of the most important features is the layer charge, which dictates physicochemical properties (e.g., swelling, activity of clay surface, cation exchange capacity) of bulk clays (Çelik 2004). During the process of re-precipitation or recrystallisation for the formation of clay minerals, there exists some defects developing inside the crystalline structure, leading to the change in electrical valance (isomorphous substitution) mainly arise from the replacement of Al^{3+} for Si^{4+} in the tetrahedral sheet and that of Mg^{2+} for Al^{3+} in the octahedral sheet on the face of clay minerals (face charge or 001 plane). Another type of charge is the pH-dependent edge charge generated by the broken bond or defects at the amphoteric edge site of clay minerals (100 plane). Considering the platy-like shape and high specific surface area (SSA with unit of m^2/g) for most clay particles (i.e., the area of clay face is much higher than that of the edge), the face surface of clay particle is thus always negative caused by the isomorphous substitution. Furthermore, the electrical negativity will be further enhanced by increasing the environmental pH that can result in a negatively-charged edge surface (Sposito et al. 1999). To maintain the overall electrical neutrality of clay particle, interlayer bonding between two crystal layers exist to balance the resulting charge deficiency caused by the isomorphous substitution. Besides, the existence of interlayer bonding highly controls the behavior of clay minerals. For instance, the strong H-bond and potassium ionic bond existing between the kaolinite and illite layers, respectively, prevent them from the expansion of the interlayer space (non-swelling clay minerals) in the presence of water, while the relatively weaker interlayer bonds (interlayer water, hydrated cations) of smectite (e.g., Na- and Ca-Smectite) impart them high swelling capacity, i.e., Na-Smectite and Ca-Smectite can form individual 2:1 layers as single particles and stacks of parallel 2:1 layers (also called tactoids or domains), respectively (Kleijn and Oster 1982; Quirk; and Aylmore 1971; Tan et al. 2014a).

To summarize, clay minerals are a group of phyllosilicate minerals characterized by their sophisticated crystal structure and complex physiochemical properties, which are further complicated by the colloidal size range (< 2 μm) and large aspect ratio that results in a very high SSA. These features comprehensively enable clay minerals to interact intensively with various active or charged particles and substances in the natural environment or laboratory conditions due to their active surface properties

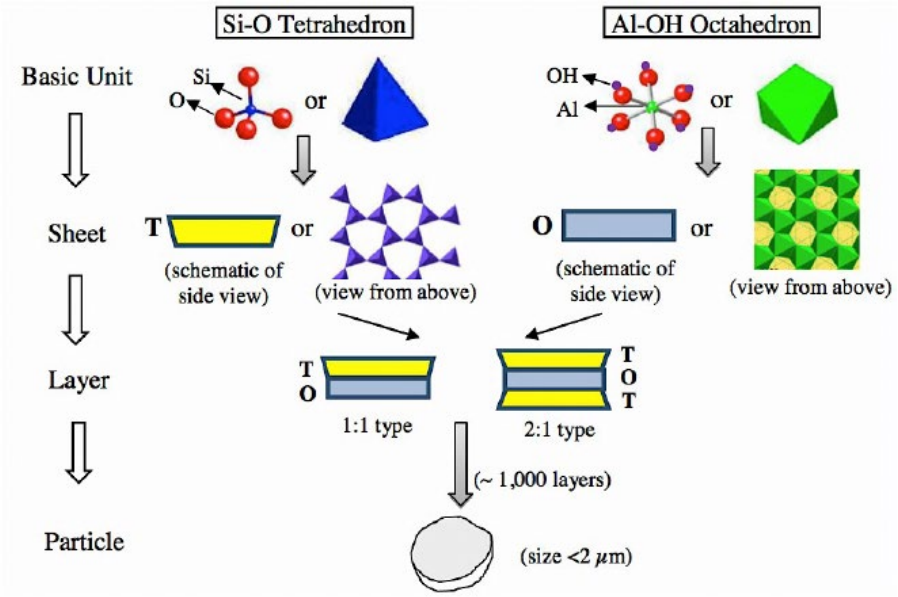

Figure 2.1 Schematic illustration of crystal structure hierarchy of clay minerals (Tan, 2013)

2.1.2 Comparison of definitions between Clay Aggregate, Floc, and Cluster

To date, three different terms, namely aggregate (Delage et al. 1996; Gens and Alonso 1992; Zhang et al. 2004a), floc (Lee et al. 2012; Zhang et al. 2013b), and cluster (Chang et al. 2009) have been used in the literature to describe the groups of clay particles. Even though they all denote similar structural units of clay, there are still some minor differences for them in terms of specific environmental scenarios. Generally, *aggregate* is the most frequent term that has been widely used in investigating both natural and laboratory-prepared fine-grained soils (including clays and silts) which possess aggregate-based microstructure. For instance, (Lefebvre and Delage 1986) employed the Scanning Electron Microscopy (SEM) and Mercury Intrusion Porosimeter (MIP) in parallel to investigate the structure of a medium sensitivity Champlain clay based on the observation from the intact, remolded, and oven-dried samples. Both methods show the existence of an aggregated structure characterized by an interaggregate and an intra-aggregate porosity. Same techniques (SEM and MIP) were also reported in (Delage et al. 1996) for the investigation of the microstructure of compacted silt at three points of the Proctor curve (dry, OMC, and wet). The results show that, with the development of compaction works, a well-developed granular aggregate structure with interaggregate porosity visible in porosimetry exists at the dry side, while less obvious aggregated structure and more developed wetter clay forming a matrix that envelops the silt grains and fills the intergranular voids at optimum side and wet side. These two studies both indicate that the micro-aggregated structure is either composed of clay platelets or silt grain groups linked together by clayey bridges, which can serve as the basic structural units of the studied fine-grained soils due to the resistance to mechanical remolding (i.e., remolding affects the interaggregate links but does not destroy aggregates); based on SEM observations reported by (Collins and Mcgown 1974), (McGown A; Collins K 1975), and (Collins 1984), (Gens and Alonso 1992) developed a microscale conceptual framework of unsaturated expansive clay which serves as an extension to the original numerical formulation that fails to model the large swelling strains exhibited by expansive soils (Figure 2.2).

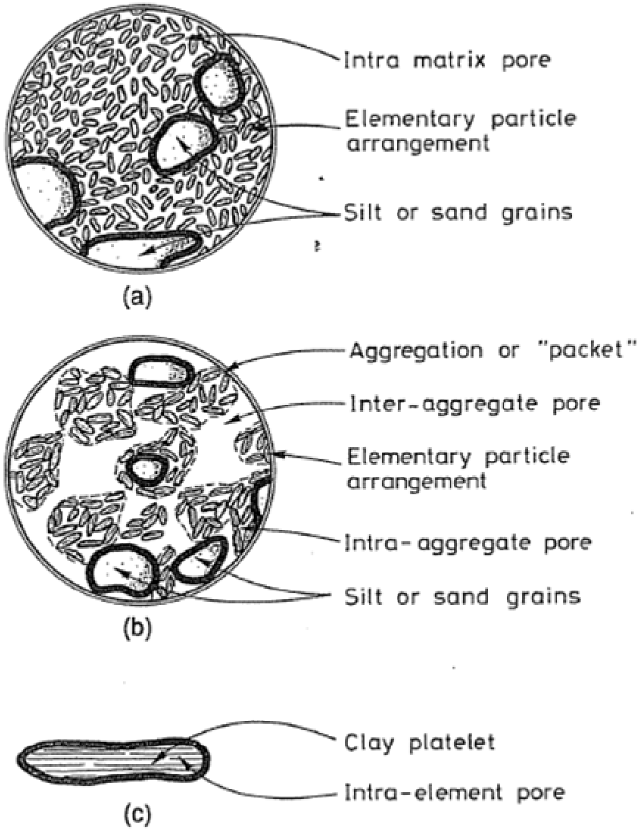

Figure 2.2 Microscale conceptual model of unsaturated expansive clay fabric proposed by Gens and Alonso (1992)

Building upon these findings, Zhang et al (2004a) further developed a conceptual microstructure model for highly weathered Old Alluvium (Figure 2.3). In this model, the basic structural functioning unit of the intact soils consists of aggregates of clay pellets (10-20 μm) that are cemented by iron oxides (the solid physical links formed through precipitation or recrystallisation between the contacts of clay platelets) and connected to form a higher level of stiff, spherical or semi-spherical mesoscale aggregates of 50-100 μm. Based on the results of oedometer tests, the existence of cementation controls the compressional properties of the intact soil. When the Old Alluvium is subjected to stress beyond yielding, there are increase in the swelling potential and decrease in the coefficient of consolidation that are related to the maximum past stress applied to the soil. This conceptual microstructural model of Old Alluvium clarified the definition of aggregate for highly structured soils; that is, the cementation of Fe-oxide serving as the small- scale surface/inter-particle forces to form groups of clay particles or other soils matrix (connection of stiff aggregates to silt and sand particles). Similar findings were also reported by Liu et al (2016) who investigated the microstructural characteristics of loess (a typical type of structured soil known for its severe collapse behavior upon inundation at certain vertical pressure) for elucidating the origin of collapsibility. They found that most silt particles in the loess are covered with clay coating and/or associated with clay particles to form hybrid silt-clay mixture aggregates in which the *calcite cementation* and *clay particles* act as the bridging agents (Figure 2.4). Feature of these bridges is the underlying mechanism for collapse properties of loess upon inundation or wetting.

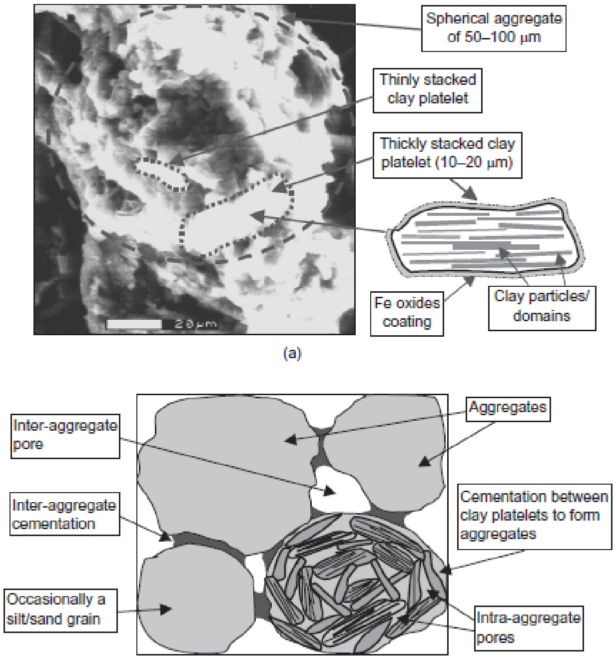

Figure 2.3 Conceptual microstructure unit of a highly weathered old alluvium (Zhang et al. 2004a)

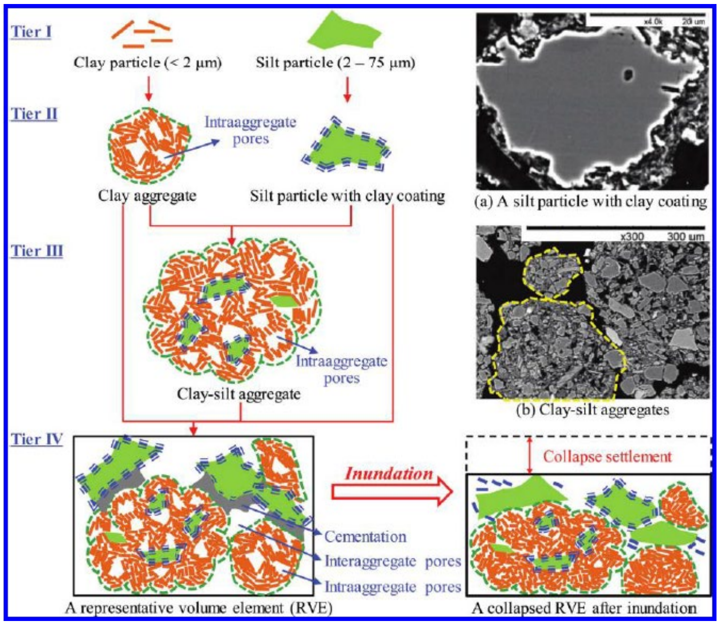

Figure 2.4 Conceptual microstructural model of four-tired hierarchy of loess (Liu et al. 2016)

One of the common features for the studies discussed above is that the aggregate structures of fine-grained soils are present in dry conditions with stiff structure. There is another term (i.e., *floc*), nevertheless, which is more specific or exclusive in describing the groups of clay particles only formed through the extensive interaction of clay particles with various types of suspended particulate matter in the natural water environments (Derjaguin and Landau 1993; Furukawa et al. 2014; Maggi 2005; Verwey and J. T. G. Overbeek 1955). As the abbreviation of flocculant mass, *flocs* refer to soft clusters formed through precipitation or aggregation of suspended particles in waters (American Heritage® Medical Dictionary, 2007), which basically accounts for the origin of clay flocs. Natural water systems (e.g., rivers, esturaies, oceans) are usually loaded with various types of suspended particulate matters of which fine-grained cohesive sediments (mainly composed of different types of clay minerals) are one of the major constituents (Mehta et al. 1989). As stated in the Section 3.1, clay minerals are characterized by their chemically active surface properties (i.e., permanent negative face charge and pH-dependent edge charge) as well as the colloidal size scale and high SSA, rendering their intensive reactivity to form a colloidal system whose stability is guaranteed by the highly repulsive forces due to the formation of diffusive double layer (DDL). Such stabilization status can be changed by the presence of extracellular polymer substances (EPS, another important constituent of suspended particulate matter in natural waters), addition of salts or dissolved ions, and pH adjustment, which usually form the clay flocs with a size range (i.e., 10 to ~1000 μm) larger than the original clay particles (Gregory 1988; Harris and Mitchell 1973; Karthiga Devi and Natarajan 2015; Okaiyeto et al. 2016; Tan 2013).

Apart from the *aggregate* and *floc*, the *cluster* (Chang et al. 2009) is another term to numerically model the stress-strain behavior of bulk clays in a way analogous to granular material (i.e., if the clusters interact with each other mainly through mechanical forces yet neglecting the long-range forces). In this model, the constituents of clay contain the platy clay particle ranging from 0.01-1 μm, clay cluster which does not undergo large deformation under external stresses (thus can be considered as the basic structural unit), and clay material as an assembly of clusters. With the performance of this model on three different clays, the effects of confining stress, OCRs, and inherent anisotropy on the stress-strain behavior are completely investigated and successfully validated.

To summarize, the background is discussed of three terms for describing the basic structural units of clays. Although the geological origin or theoretical background vary among these terms, the basic idea is consistent, i.e., the basic functioning structural units of clays are physically and chemically stable and resistant to breakdown from remolding and other stressing processes. Since a standard or unified definition is still not available, this proposal will mostly use *aggregate* Particularly, clay aggregates and clay flocs will be used interchangeably when it is necessary to stress the importance of environment factors in natural aqueous systems.

2.2 Experimental Measurements of Particle Size Distributions of Clay Flocs

2.2.1 Environmental Effects on the PSDs of Fine-grained Cohesive Sediments

Fine-grained cohesive sediments are widely present in most suspended particulate matters in nearly all types of natural water systems, particularly in nearshore and estuarine areas resulting from the sediment transport process (Elfrink and Baldock 2002; Graf 1999; Lewis 2009; Partheniades 2009; Seo et al. 2009). Different types of clay minerals make up the main components of cohesive sediments, leading to a variety of interesting phenomena in consideration of the intensive reactivity of clay minerals with other suspended substances (e.g., EPS) in waters due to their active surface properties (e.g., permanent negative face charge, pH-dependent edge, charge, High SSA). One representative phenomenon is that most fine-grained cohesive sediments exhibit multi-modal particle size distributions (PSDs) through transport/sedimentation in marine/coastal environments, because of the flocculation of fine-grained cohesive sediments mainly dictated by the clay minerals. A four-level ordered conceptual structure has been developed as a basic framework in prior studies to describe the particle groups composed of fine-grained cohesive sediments which is similar to the four-level structural hierarchy proposed by (Gens and Alonso 1992) for the aggregates in unsaturated expansive clays: (1) Primary particles including dispersed clay minerals, organic and calcareous particles, picophytoplankton and heterotrophic bacteria all with a wide size range of 0.25 to 2.5 μm; (2) Flocculi with a size range of 10 to 20 μm which is regarded as the basic structural units of cohesive sediments; (3) Microflocs with a size range of 50 to 200 μm consisting of floccule and primary particles; (4) Macroflocs with a size range of hundreds to thousands of micrometers built from primary particles, flocculi, and microflocs (Alldredge and Silver 1988; Lee et al. 2012; Van Leussen 2011; Manning and Bass 2006; Mikkelsen et al. 2006). Given the active physiochemical properties of clay minerals and the abundance of chemical substances in the natural aqueous systems, the flocculation process of fine-grained cohesive sediments is complexly varied depending upon several environmental effects, such as the type and concentration of EPS. For example, (Zhang et al. 2013b) investigated the particle size kinetics of suspended cohesive sediments (mainly composed of pure clay minerals, namely kaolinite, illite, Na-montmorillonite and Ca-montrmoillonite) affected by two types of EPS (xanthan and guar). They found that both pure clay and clay-EPS suspensions exhibit multimodal PSDs of which each statistical fraction corresponds to characteristic particle group following unimodal lognormal distributions with different size range of particles, i.e., primary particles, flocculi, microflocs, and macroflocs (Figure 2.5).

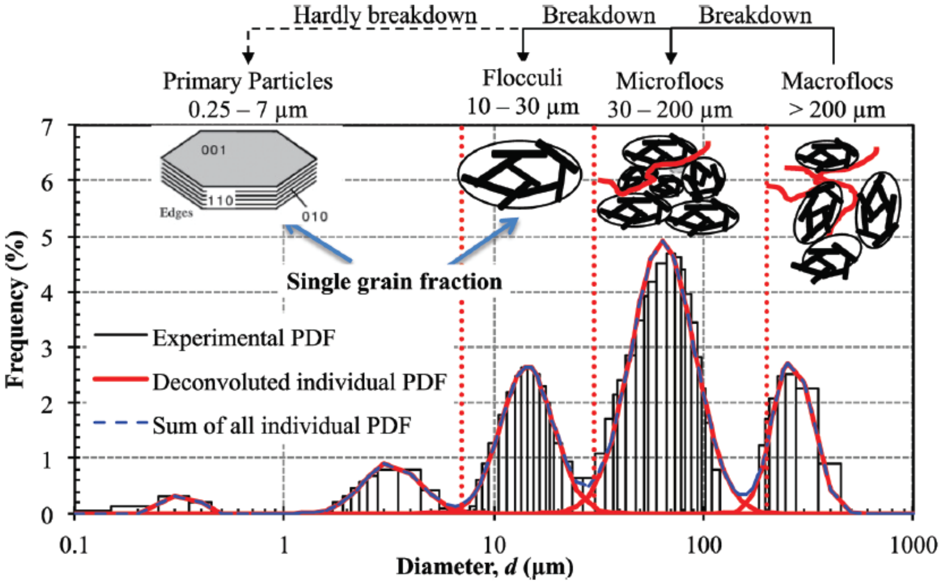

Figure 2.5 Schematic illustration of multimodal PSDs of clay-EPS flocs composed of four different particle groups (Zhang et al. 2013b)

While pure clay suspensions consist of mainly particles and flocculi, adding EPS to a clay suspension can cause the formation of microflocs and macroflocs, which, however, is dependent upon the polarity of clay minerals and EPS as well as the EPS concentration. The variation of ionic strength induced by the addition of dissolved salts or ions is another important environmental factor that affects the flocculation of suspended cohesive sediments, including two main mechanisms, i.e., compression of electric double layer due to the increasing concentrations of counterions thus decreasing the repulsive forces between clay particles and sweep flocculation caused by the presence of metal ions (such as Al^{3+} and Fe^{3+}) in water forming entangled units that assemble clay particles together (García-García et al. 2006; Israelachvili 2011; Luckham and Rossi 1999; Sincero and Sincero 2002; Tan et al. 2014a). In particular, the extent of flocculation facilitated by the EPS or other types of polyelectrolytes is interestingly affected by the suspension ionic strength/salinity. At lower ionic strength, the reduction in the repulsion between polymers on the particle surface increase adsorption (screening-enhanced regime), while at higher ionic strength, the reduction of electrostatic attraction between the polymer and the particles reduces polymer adsorption (screening-reduced regime) (Dobrynin and Rubinstein 2005; Gittings et al. 2001). In addition to the effects of EPS and ionic strength, the pH of suspensions is also an important factor on the flocculation of fine-grained cohesive sediments. Generally, as the environment pH is lower than the pH_{PZC} (pH of point of zero charge) of specific clay minerals, flocculation of clay particles will be promoted with edge-to-face particle associations, due to the positively pH-dependent edge charge; otherwise, dispersion which is originally strong between clay particles will be strengthened resulting from the both permanently negative face charge and negatively pH-dependent edge charge (Gupta et al. 2011; Mietta et al. 2009; Wilkinson et al. 2018).

The effects of EPS or other types of polyelectrolytes, ionic strength, and pH all significantly impact the process of flocculation by changing the interactive abilities (e.g., surface potential, electrostatic force fields) of clay particles, which results in a change in the PSD of suspended cohesive sediments. Furthermore, in natural aqueous environments where flow occurs dynamic, such change is further affected by the shear stress exerted by the hydrodynamic flow regime. Generally, the change of PSD affected by hydrodynamic flow is the outcome of dynamic balance between two simultaneous, competing effects: (1) flocculation which transfers coagulated particles (primary clay particles whose surface properties have been chemically changed) into contact with each other to form larger clay particles (e.g., flocculi, microflocs, macroflocs) and (2) breakup of existing clay flocs into smaller particles or fragments, as schematically illustrated in Figure 2.6 (Jarvis et al. 2005a).

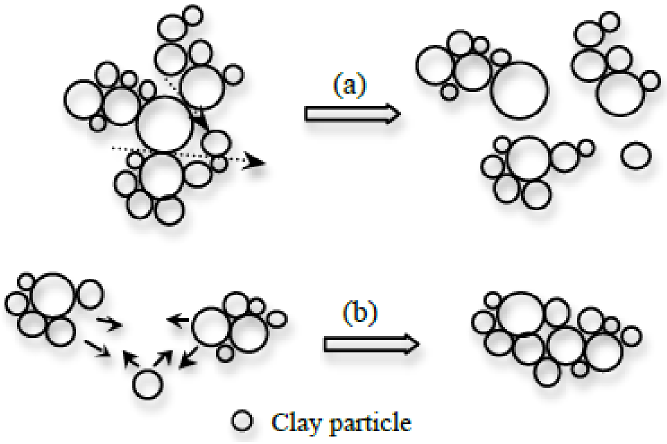

Figure 2.6 Schematic illustration of effects of shear stress on the flocculation and aggregation of clay particles and flocs in aqueous flow: (a) flocs break into smaller flocs or particles due to flow induced shear force; (b) flocculation by the increased collision possibility (Jarvis et al. 2005a)

Apparently, it is the flow-induced shear stress that determines the fate of the newly formed clay flocs. In other words, if the newly formed clay flocs have higher shear strength than the exerted shear stress, then a PSD with higher fraction of larger-sized particles is expected due to the effective flocculation; otherwise, the breakup of newly formed flocs and reduction of total particle size if flocs are not strong enough to resist the shear stress. With the evolution of flocculation, a steady state will be finally achieved in which the PSD and mean flocs/particles size remain constant even during the continuous process of flowing (Moruzzi et al. 2017; Spicer and Pratsinis 1996) (Spicer and Pratsinis, 1995; Moruzzi et al., 2017). However, owing to the varying hydrodynamic conditions in natural aqueous systems (e.g., multiple tidal cycles), such equilibrium will be disrupted if the hydrodynamic shear stress rapidly increases resulting from the more turbulent flow rate, leading to the significant breakage of the existing flocs which fail to resist the increasing shear rate, followed by the regrowth of large flocs when the shear rate restore to that of the steady state (Keyvani and Strom 2014; Tran and Strom 2019; Vaezi G. et al. 2011a; Yu et al. 2011). Figure 2.7 shows a good example of regrowth behavior of broken flocs. It is worthwhile that there is only a partial recovery of the flocculation index (a sensitive measure of flocculation behavior which indirectly represents the regrowth of flocs) after breakage, implying that the broken flocs can only re-grow to a limited extent.

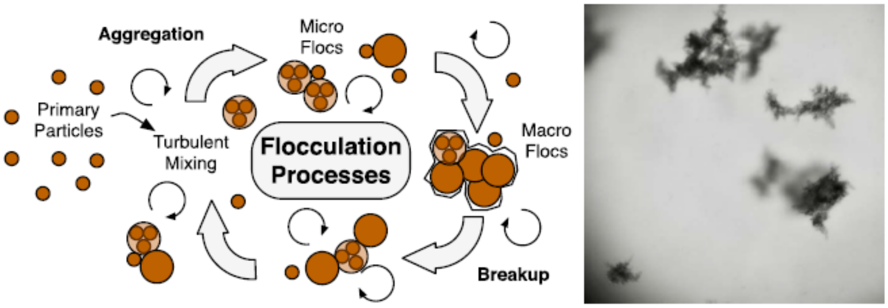

Figure 2.7 Schematic illustration of growth-breakup cycle of clay minerals flocculation process (Keyvani and Strom 2014)

In summary, the flocculation and PSD of suspended cohesive sediments is mainly controlled by the reactivity of main solid constituents, clay minerals whose physicochemical properties are significantly affected by the environmental factors such as the type and concentrations of polyelectrolytes (e.g., EPS), ionic strength, and pH in most natural waters. Such process is further complicated by the dynamic hydrodynamic flow conditions that dictates the collisions, breakup, and regrowth of flocs. It is of great importance to have advanced knowledge on the kinetics of flocculation of cohesive sediments because of the effects of PSD on the sediment transport, flocculation, and settling (Chen et al. 2005a).

2.2.2 Characterization Techniques for PSD of Clay and Clay-EPS Flocs

To measure the PSD of clay or clay-EPS flocs existing in natural aqueous or laboratory-based environments (e.g., clay suspensions), numerous techniques have been developed and applied in previous studies, mainly including laser particle size analyzer, focused beam reflectance measurement (FBRM), and imaging analysis under microscope, using dynamic image analysis (DIA) and particle vision measurement (PVM), which will be introduced respectively as follows:

- Laser Particle Size Analyzer: laser particle size analyzer is a widely used tool (either laboratory-based or in-situ) for the measurement of particle size of various types of cohesive sediments such as clay and mud, of stability for soil aggregation and clay dispersion, and of erythrocyte deformability under shear (McCave et al. 1986; Viallat and Abkarian 2014; Westerhof et al. 1999). The basic principle of this technique is to utilize a laser beam with characteristic diffraction pattern to pass through specific objects with the size range of nm to mm, such that the geometrical dimensions of the object can be measured. Depending upon the object particles, the laser particle size analyzer can be categorized as dynamic light scattering which is usually applied for nanoparticles or nanodroplets featured with a size range of < 1 nm that render them to undergo Brownian movement, and static light scattering which is more suitable for measurement of clay flocs whose size is generally larger than 2 µm (De Boer et al. 2002). The main components of laser particle size analyzer are schematically illustrated in Figure 2.8, including the laser source injecting laser beam passing through particles, laser beam expander increasing the diameter of a collimated input beam to a larger collimated output beam, and multi-element detector generating diffraction patterns of measure particles after Fourier transformations (Govoreanu et al. 2009; Song and Trass 1997; Šulc et al. 2012; Zhou and Franks 2006). Figure 2.9 shows an example employing the Cilas 1190 particle size analyzer inside which the laser beam scans each clay flocs to generate diffraction patterns in the signal detector, thus the PSD of tested clay suspensions can be measured (Zhang et al. 2013b).

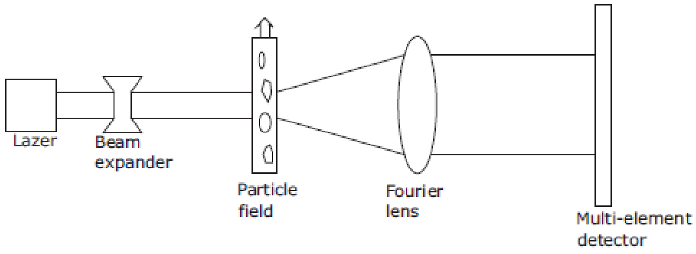

Figure 2.8 Schematic of the laser particle size analyzer

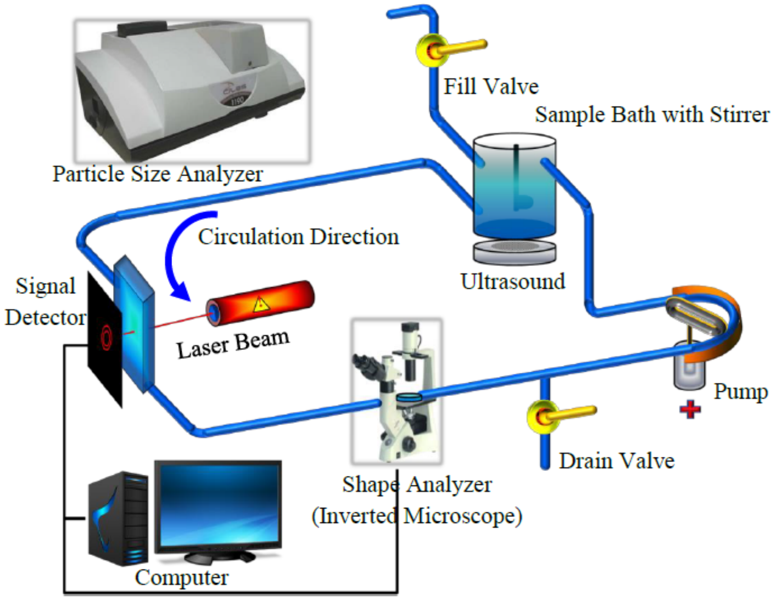

Figure 2.9 Example of laser beam used for PSD quantification in the Cilas 1190 particle size analyzer (Zhang et al. 2013b)

- Focused Beam Reflectance Measurement (FBRM): FBRM is also a light-scattering based technique for particle size analysis. Figure 2.10 shows the schematic of a typical FBRM instrument and the measurement of particle chord length through FBRM, which illustrates the basic principle of this technique. The background scattering light is collected by the optical detector when the measured particles are contacted by the light beam moving around the circumference of sapphire window at a high speed (2-6 m/s), and then the particle size is reflected by the time period between two collected backward scattering lights by obtaining the distance (chord length of a particles) through multiplying the time period with the scan speed of the focused beam. The primary chord length distribution can then be used as the indication of particle size if the size of small particles of interest (Heath et al. 2002; Senaputra et al. 2014). Compared with the laser particle size analyzer, the routine sampling procedure as used in the laser particle size analyzer is avoided, which prevents the breakage of flocs. Also, the variation of floc size versus time can be recorded, which can quantitatively characterize the floc growth over the time (Figure 2.10b).

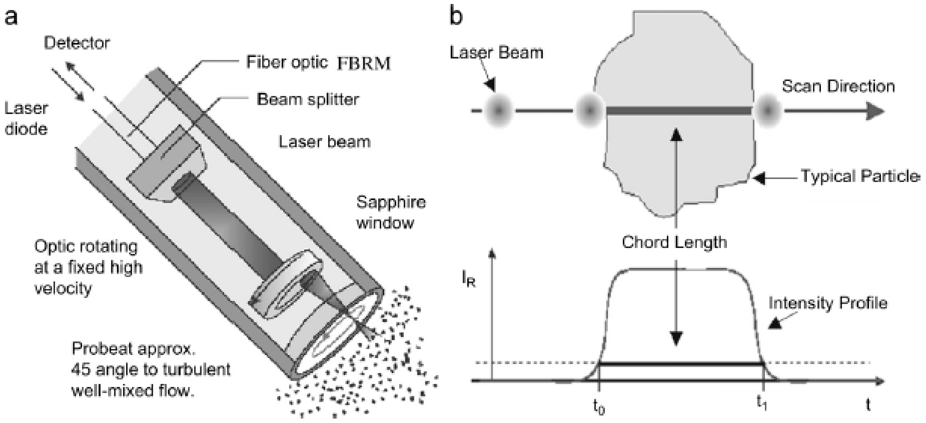

Figure 2.10 (a) Schematic of FBRM instrument and (b) the measurement of particle chard length through FBRM (Greaves et al. 2008)

- Microscope: laser particle size analyzer and FBRM are both powerful techniques for measuring particle size of cohesive sediments in laboratory or in-situ conditions, however, the purchasing costs for them are usually quite expensive so that access to these techniques, sometimes, is limited. Fortunately, there is an alternative by performing image analysis with specific image analysis software (e.g., image J, an open-source java-based platform developed by national institute of health for image processing) to directly measure each particle size in suspensions. To obtain accurate and representative result, a large amount of sampling and measurement need to be repeated due to the small areas of containers (e.g., culture dish) for holding the clay suspensions. General procedure of image analysis is schematically illustrated in

Figure 2.11, which includes, but not limited to, background subtraction of raw image (8-bit gray scale), complementation, hole filling, separation and clearing under certain thresholding value, and finally the particle size analysis (Li et al. 2005).

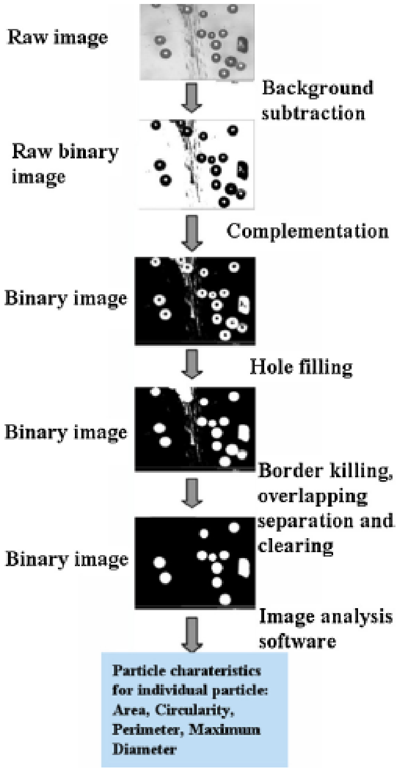

Figure 2.11 General procedure of particle image processing (Li et al. 2005)

- Digital Image Analysis (DIA): DIA is another image-analysis based technique used for the characterization of PSD. Compared with the traditional image analysis with the aid of microscope, DIA has the advantage of continuously obtaining images by image acquisition instruments such as CCD camera, allowing for quicker and larger amount of imaging processing performed automatically, thus sharing similar procedure of image processing with the microscope method (Li et al. 2008)

- Particle Video Microscope (PVM): As another type of image-based analysis technique, PVM is however very similar to FBRM which has been used together for in-situ determination of particle size distribution and particle structure in slurry (Liu and Peng 2014). Compared to DIA, the combination of PVM and FBRM has the advantage of not needing to pump out the slurry in the device, diminishing the inconsistency of flow conditions of primary system and measurement cell.

2.3 Characterization of Microfabric of Clay Flocs

Soil fabric refers to the particle arrangement and association, which combines with the interparticle forces to form the soil structure that is important in controlling the physicochemical behavior and engineering properties of soil as its composition and stress history (Lambe and Whitman 1969; Mitchell and Soga 2005). Advanced characterization techniques such as SEM has enabled researchers to directly observe the microfabric and associated morphology features (e.g., particle size, shape and boundary) (Kim and Palomino 2009; Kühnel 1990; Liu et al. 2016; Zhang et al. 2004a). For most studies conducted on the microstructural characteristics of clay aggregates, the prepared samples for characterization are usually in dry and densely packed conditions such that the environmental SEM or even ESEM can also be employed when the pore fluids in samples should be removed (Lin and Cerato 2014). For clay flocs, however, significant challenge exists in the observation of microstructure using SEM or ESEM since clay flocs are usually present in the form of cluster-like particle groups featured with their complex tenuous, porous, and fractal properties, which renders the clay flocs with extremely high-water content and soft consistency (Furukawa et al. 2009; Kranenburg 1994). To address this issue, high-pressure freeze drying (a process that forces vitrification of water without formation of ice crystals) have been used to prepare floc samples for SEM observations. For example, (Tan 2013) developed a custom method for the preparation of pure clay and clay-EPS flocs, which basically involves subjecting the extracted floc suspensions fixed on the carbon tape to freeze drying in the freeze dryer, Model 35 XL Genesis, Virtis, Gardiner, NY, followed by conducting the SEM observation of the freeze-dried flocs using the FEI Quanta 3D FEG Dual Beam FIB/SEM (FEI Company, Eindhoven, the Neterlands), as schematically illustrated in Figure 2.12.

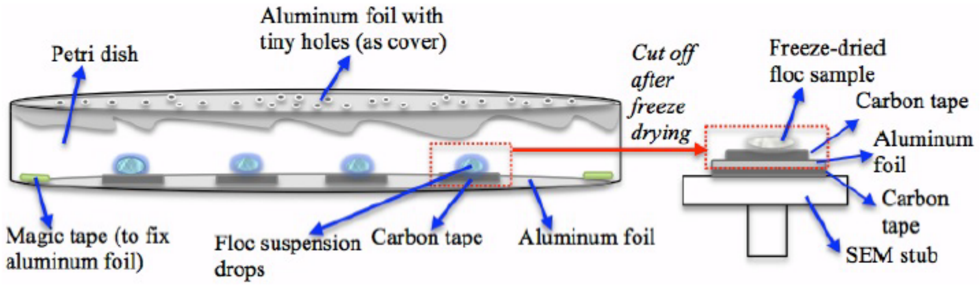

Figure 2.12 Schematic of custom sample preparation for SEM observation of freeze-dried clay flocs (Tan 2013)

Tan (2013) observed quite interesting microstructural characteristics of four freeze-dried pure clay samples (i.e., kaolinite, illite, Na-Montmorillonite, and Ca-Montmorillonite) and corresponding clay-guar gum (a water-soluble polysaccharide extracted from guar beans with a molecular weight of up to 2×10^6 Da) flocs prepared in Deionized water. As shown in Figure 2.13, individual, circularly or elliptically shaped flocculi of 10-30 μm (the basic structural unit for clay flocs) are widely present in four pure clay samples, while the morphology and arrangement of individual particles (e.g., face-to-face and face-to-edge particle associations) within flocculi for these samples are quite different from each other, which can be attributed to the different physicochemical properties for each clay sample, leading to the varying surface interaction forces between particles.

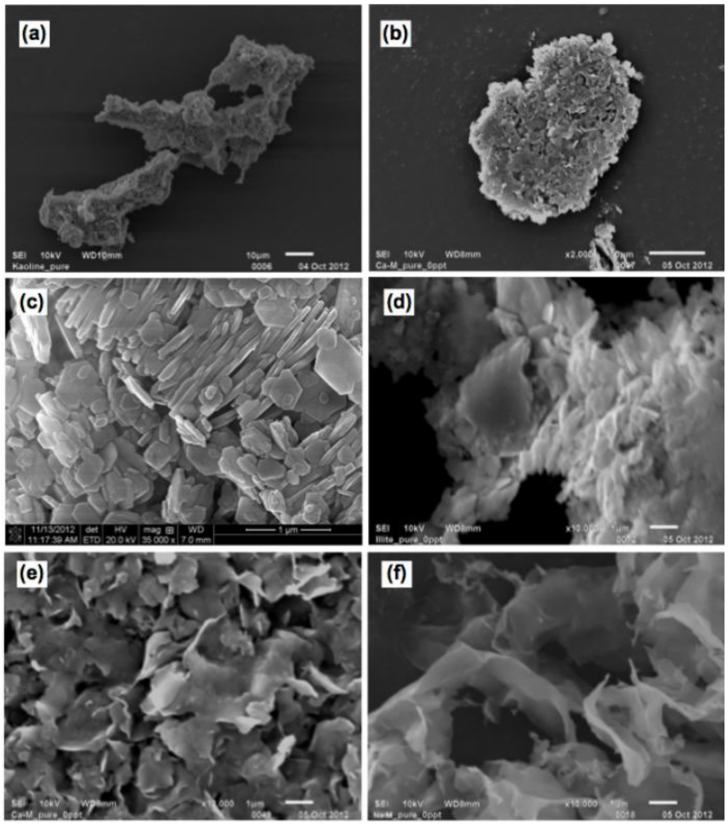

Figure 2.13 SEM images for freeze-dried samples of four pure clay samples: (a) kaolinite and (b) Ca^{2+}-Mt at a lower magnification, and (c) kaolinite, (d) Illite, (e) Ca^{2+}-Mt, and (f) Na^{+}-Mt at a higher magnification (Tan 2013).

For clay-guar gum flocs, the results of SEM characterization demonstrate the presence of complex network associated with the interconnection of guar fibrils to the clay flocs (Figure 2.14), which basically involves three kinds of clay-guar associations: (1)

individual clay particles and flocculi adhesively coated by the film-like EPS bundles (Figure 2.14a), (2) groups of clay particles, floccule, and microflocs interconnected by the bridging of fibrils and bundles of EPS (Figure 2.14b), and (3) gluing of EPS fibrils and bundles to the individual clay particles (Figure 2.14c-d).

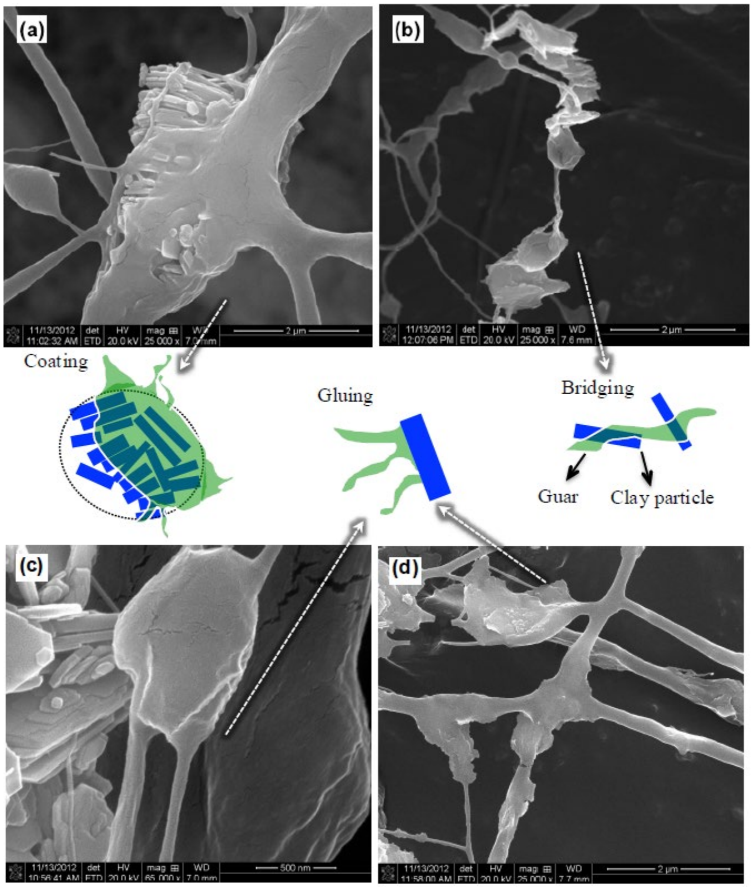

Figure 2.14 Example SEM images demonstrating the arrangement of clay and guar associations (Tan 2013)

Apart from the powerful microscopy techniques such as SEM, indirect methods for observing the microstructure of clay flocs, notably the measurements of free settling velocity, have also been widely used to provide referenced parameters closely associated with the microstructural characteristics, such as the density, fractal dimension, and porosity.

The routine procedure of this method is to plot the settling velocity W_s against floc size with double logarithmic axis, thus the fractal dimension, d, can be found from the slope (d-1) of the linear relationship between log (W_s) and log (D) (Droppo et al. 1997; Hill 1998; Huang 1993; Kobayashi 1999; Likos and Lu 2001; Miyahara et al. 2002; Tan et al. 2012; Ye et al. 2020). Figure 2.15 shows typical results of free settling velocity test for four pure clay flocs and clay-EPS flocs, which generates fractal dimensions ranging from 1.76 to 1.86, while the clay-EPS flocs 1.39 to 1.47, indicating that the presence of neutral EPS significantly decreases the density of flocs. Also, since the fractal dimension of each type of flocs is smaller than 3, suggesting that the clay flocs themselves are intrinsically not compacted but highly porous materials.

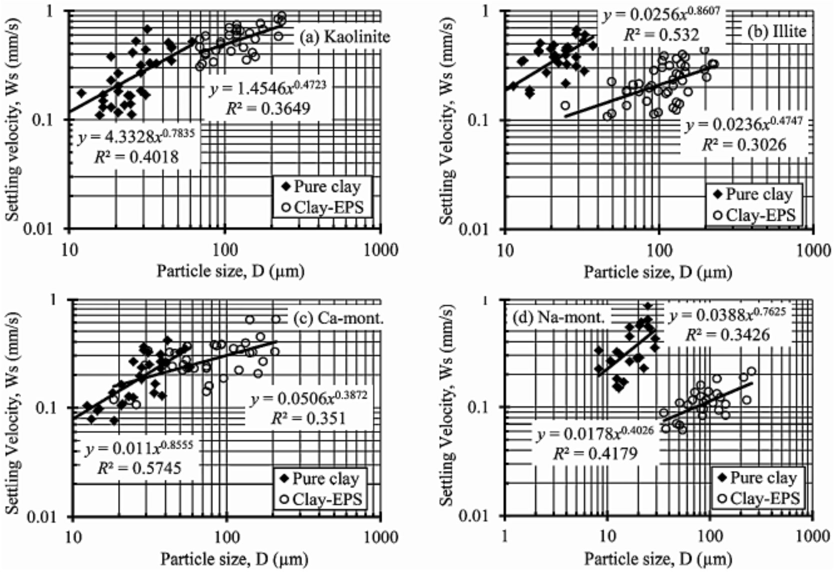

Figure 2.15 Settling velocity versus particle size of pure clay and clay-EPS flocs (Tan 2013)

In summary, with the advancement of powerful microscopy techniques and preparation methods, the microstructural characteristics of clay and clay-EPS flocs have been well investigated. Although flocs have multiscale internal pore distributions as similar as the clay aggregates (i.e., interlamellar pores, intraaggregate pores, interaggregate pores), they exhibit softer, more tenuous, and fractal structural characteristics compared with the aggregates, primarily due to the formation mechanisms of aggregation or flocculation occurring in the laboratory-prepared and natural aqueous environments where aqueous conditions are usually employed.

2.4 Mechanical Properties of Clay Aggregates and Granular Biofilms

2.4.1 Motivations and Methods for Measuring Strength of Clay Aggregates

As introduced in Chapter 1, compared with their sandy counterparts, mesoscale aggregate-based structure is essentially necessary for investigating the behavior of fine-grained soils (especially for clays) as a particulate system. Such structural unit can serve as the basic target for direct numerical modelling and experimental measurements in terms of mechanical characteristics, which allows for the development of multiscale methods for bridging between the micro- and macro-scale systems. In addition to the contributions to theoretical advancement, understanding on the mechanics of clay aggregates or flocs dominantly present in suspended cohesive sediments is of great importance in a variety of environmental and engineering implications, such as coastal and marine sustainability (e.g., transportation of sediments and contaminants, Carbon sequestration), geophysical remote sensing (e.g., marine acoustics, optical reflectance), wastewater treatment (Chen et al. 2005b; Hermawan et al. 2004; Maximova and Dahl 2006). The obtained size and mechanical properties can provide key parameters to these applications for modelling floc collision and floc bearing soils and their transport fate.

Many efforts have been devoted to the development of techniques for characterization of aggregate/floc strength. Generally, two fundamental measurement approaches have been utilized in prior studies in terms of *macroscopic* (on the measurement of the energy required in a system for floc breakage under hydrodynamic shear stress) and *microscopic* (on the measurement of the inter-particle forces within individual aggregates/flocs) aspects (Jarvis et al. 2005a). For most macroscopic measurements performed on the water-bone flocs, the research inspirations arise from the inherent relationship between the applied hydrodynamic shear rate and the resulting floc size (i.e., aggregation/flocculation of colloidal particles are facilitated under relatively low shear rate conditions), while break-up is very likely to occur under high shear rate. As such, the comparison of floc size before and after breakage can serve as an indicator for the floc strength indirectly. One example associated with this idea is the calculation of a floc strength factor, the ratio of floc size after and before breakage at a particular shear rate (François 1987; Govoreanu et al. 2003). Basically, the higher the value of the strength factor, the less susceptible the flocs are to shear breakage and thus stronger as shear rate increases. Another factor frequently used for the quantification of floc strength is based on the average velocity gradient G:

$$G = \sqrt{\frac{\varepsilon}{\upsilon}} \tag{3.1}$$

where ε is the rate of energy dissipation per unit mass of suspension, and υ is the kinematic viscosity:

$$\varepsilon = \frac{P_0 N^3 D^5}{V} \tag{3.2}$$

where P_0 is the impeller power number, N is the impeller speed, V is the stirred tank volume and D is the impeller diameter. Based on these equations, (Parker et al. 1972) proposed an empirical method to graphically relate the floc size with the average velocity gradient in the log-log plot, as shown in Figure 2.16.

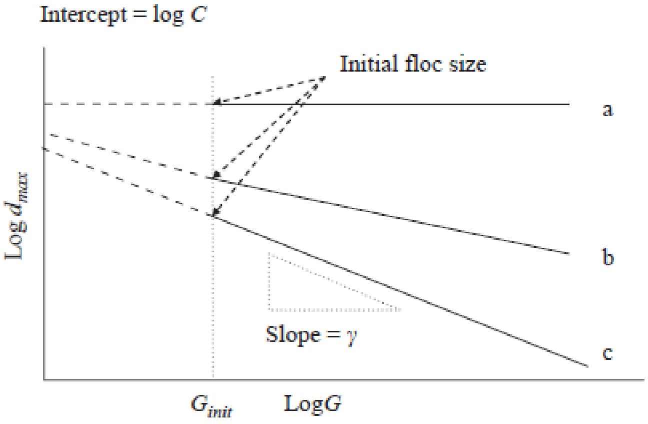

Figure 2.16 The relationship between the change in particle size and an increase in velocity gradient for three types of floc: (a) resistant to breakage; (b) breakage due to large-scale fragmentation; (c) breakage by surface erosion (Jarvis et al. 2005a)

In comparison with the macroscopic techniques, the microscopic counterparts are more direct for characterizing the strength of flocs, which basically study the micro/meso-scale mechanical behaviors of flocs influenced by small-scale forces acting on the single floc. For example, (Yeung and Pelton 1996) adopted two glass suction pipettes to measure the flocs tensile strength directly by rupturing and reflocculating strength (also known as micromanipulation cantilever approach), as shown in Figure 2.17. (Zhang et al. 1999) used another microscale manipulation technique called micromanipulation probing to characterize the breaking force of latex particle aggregates, which subjects the single aggregate to deformation by moving a force transducer (resolution: 1 μN) downward until the breakage of the tested floc (Figure 2.18). Yin (2013) conducted a systematically experimental studies in characterizing the mechanical properties (Young's modulus, yield shear stress) of pure kaolinite and Na-montmorillonite flocs prepared in saline waters and four types of clay-EPS flocs, with a pioneering, self-developed experimental device and analytical method (i.e., use of Hertz elastic contact theory to derive the reduced modulus and Weibull statistical analysis for the average value of mechanical properties) (Figure 2.19). The recent development of advanced theoretical studies as well as state-of-the-art experimental techniques (Israelachvili 2011; Wang et al. 2015a) have also enabled deep understanding on the interparticle forces between flocs or intermolecular/surface forces within flocs, such as the van der Waals force, electrical double layer force, hydration force, and chemical bonds between colloidal particles and flocculants.

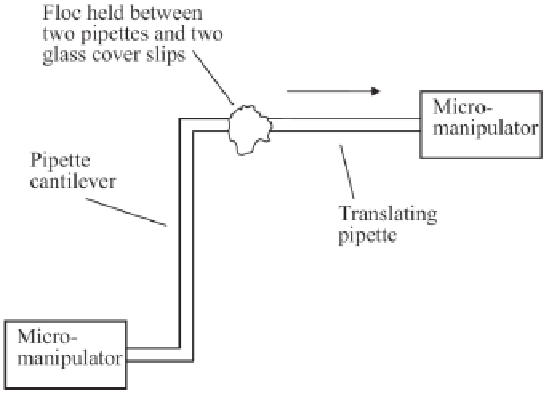

Figure 2.17.Micromechanical testing device (micro-manipulators) for measuring the strength of soft flocs (Jarvis et al. 2005a; Yeung and Pelton 1996)

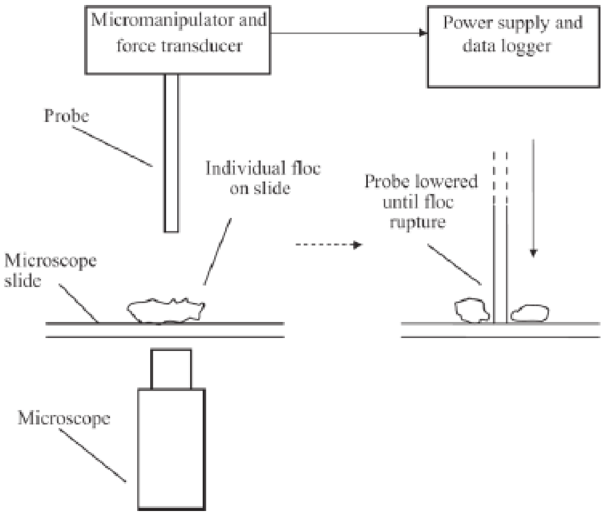

Figure 2.18 Schematic of microprobe technique for measuring the strength of soft flocs (Zhang et al. 1999)

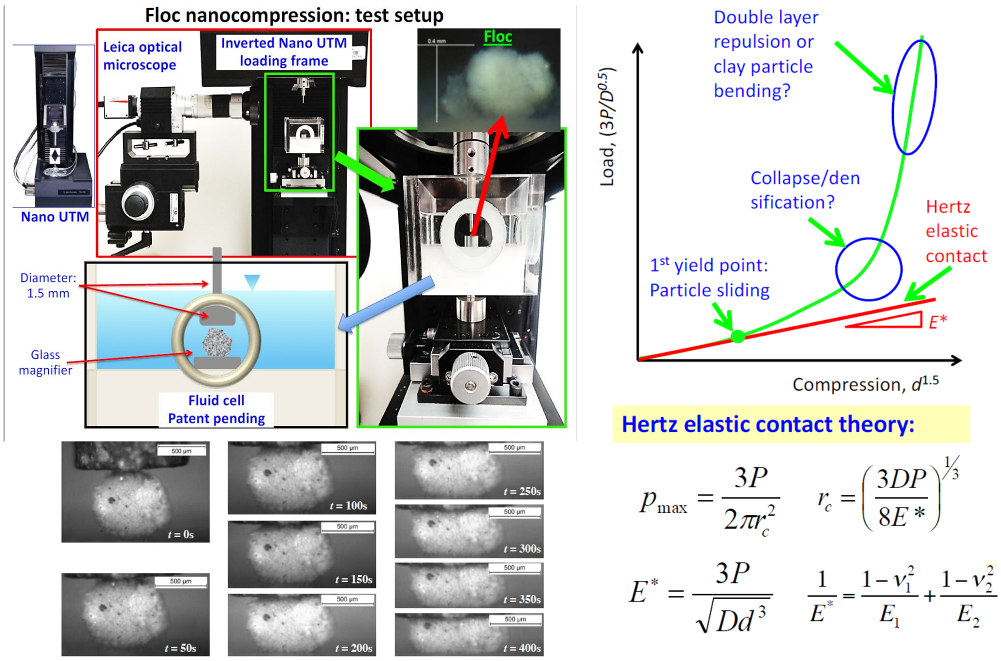

Figure 2.19 A patent experimental setup for the nano/micro compression testing of clay flocs and application of Hertz elastic contact theory for deriving the elastic properties of flocs (Yin 2013)

2.4.2 Backgrounds of Granular Biofilms

In addition to the abundant fine-grained cohesive sediments and EPS which constitute the major suspended particulate matters in natural aqueous systems, free-floating/suspended microorganisms (e.g., planktonic bacteria) also highly impact the underwater ecosystems by actively participating in various types of environmental process and microbiological synthesis such as the formation of biofilms. Figure 2.20 shows a typical stages of biofilm development in which the microcolonies composed of planktonic microorganisms and EPS gradually build up into a complex assemblage of bacteria closely intertwined with the three-dimensional EPS which primarily serves as the matrix maintaining biofilms structural integrity (Boudarel et al. 2018). Most wastewater treatment processes have used this process to form anaerobic and aerobic granular sludge (basically spherical, compact aggregates of biofilms) for water purifications (Gagliano et al. 2017; van Lier et al. 2015; Weber et al. 2008). Particularly, one bioengineering technique involving the formation of oxygenic photogranules (OPGs) in wastewater treatment has attracted growing research interest due to its promising potential in reducing the operating costs by eliminating the need for external aeration (Park and Dolan 2015). Also, significant environmental implications have been revealed in literatures that clay minerals also interact intensively with bacteria and EPS in the process of biofilms aggregation (Alimova et al. 2006, 2009). As such, studying the mechanical characteristics of biofilms with aggregated structure will not only deepen the understanding of the physical stability of biofilms and their life cycle, but also shed light upon the development of water-bone clay aggregates/flocs that is important to geotechnical and geoenvironmental communities.

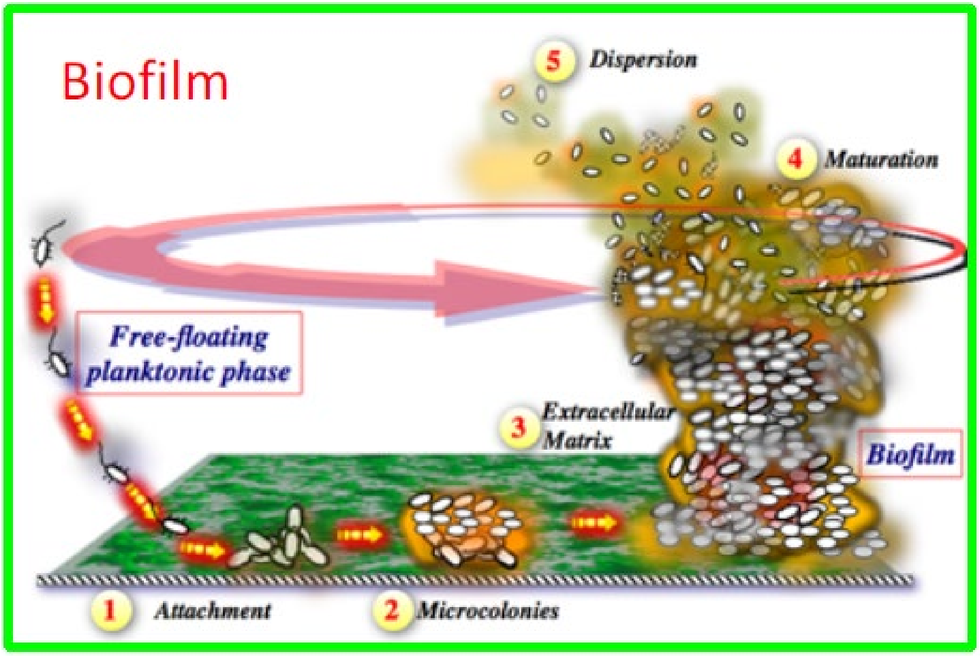

Figure 2.20 Stages of biofilm life cycle (Sehar and Naz 2016)

CHAPTER 3

A NEW BIN SIZE INDEX METHOD FOR BINNING MULTIMODAL DATASETS FROM MATERIALS CHARACTERIZATION[1]

This paper presents a new, normalized standard error-based statistical data binning method, termed “bin size index” (BSI), for optimizing an objective bin size used to construct a rational histogram to facilitate subsequent deconvolution of multimodal datasets obtained from materials characterization, leading to the determination of the underlying probability density function (PDF) distributions, including the number, mean, standard deviation (SD), and fraction of different modes. A total of 10 multimodal datasets, consisting of 4 normally-distributed synthetic ones, 3 normally-distributed ones on the elasticity of three rocks obtained by statistical nanoindentation, and 3 lognormally-distributed ones on the particle size distributions (PSD) of flocculated illite suspensions, were used to illustrate the BSI’s concepts and algorithms. While results from the synthetic datasets prove the method’s accuracy and effectiveness, analyses of other measurement datasets further demonstrate its rationale, performance, and applicability to real problems such as materials characterization. The BSI method also enables the determination of the number of modes via the comparative evaluation of the errors returned from different trial bin sizes. The accuracy and performance of the BSI method are further compared with other widely used binning methods, and the former yields the highest BSI and smallest normalized standard error. The advantages and disadvantages of the new method are also discussed.

---

[1] This chapter was submitted to Annals of Applied Statistics as a standalone paper: Jiang, T., Luo, S., Li, Y., He, L., Guo, D & Guoping Zhang (2022). A New Bin Size Index Method for Binning Multimodal Datasets from Material Characterization. *Annals of Applied Statistics*, under review

3.1 Introduction

Variates or random variables obeying multimodal distributions are ubiquitous and frequently encountered in all science and engineering disciplines. If the mathematical distribution function is known, the graphic presentation of such a distribution, such as the plot of probability density function (PDF), is typically characterized by multiple isolated or overlapping distinct peaks or modes. In most cases, however, the actual mathematical distribution function is not readily available for an unknown variate, and hence multiple, repeated sampling or measurements are necessary to obtain a series of data, which vary with the outcomes of random events or phenomena and hence constitute a multimodal random dataset. There are numerous examples of multimodal datasets encountered in daily practices and routine measurements. For instance, the particle size distribution (PSD) of a dry concrete mix that is usually composed of finer Portland cement, medium-sized sand, and coarser aggregate as well as additives such as plasticizers exhibits at least three modes. Moreover, upon hydration and setting, the hardened concrete made of inter-cemented particles may still possess a multimodal (e.g., 3 or more modes) PSD, due to the formation of nanocrystalline calcium-silicate-hydrates, non-hydrated cement particles, and non-reactive sands and aggregates. The second example is the characterization spectra, obtained by Fourier transform infrared (FTIR) and solid-state nuclear magnetic resonance (ssNMR) spectroscopy, of some silicates (e.g., silica aerogels) (Borba et al. 2017) and aluminosilicates (e.g., geopolymers) (Wan, Q., Rao, F., Song, S., García, R. E., Estrella, R. M., Patiño, C. L., & Zhang 2017) consisting of highly complex networks of molecular clusters including tetrahedral $[SiO_4]^{4-}$ and/or $[NaAlO_4]^{4-}$. Other examples include the PSD and pore size distributions of some natural soils and suspended sediments (Lee et al. 2012;

Zhang et al. 2013) consisting of different-sized particle groups (e.g., clay, silt, sand, and clay flocs), as well as the small (e.g., nano or micro) scale local mechanical properties of multiscale and multiphase composite materials consisting of mechanically distinct constituents (e.g., rocks, concretes), as further discussed later.

A thorough understanding of a multimodal dataset repeatedly sampled from a variate requires further data processing and treatment to uncover the basic statistics and underlying distributions. Such data analyses usually commence with assuming a certain type of statistical distributions (e.g., the Gaussian or normal distribution) for the variate of interest and terminate with statistical deconvolution, which is widely used to definitely determine the number, mean, standard deviation (SD), and fraction of different modes as well as the global distribution function. Depending upon the nature of the datasets (e.g., one, two, or multi-dimensional datasets), PDF, cumulative distribution function (CDF), and Gaussian mixture modeling (GMM)-based statistical deconvolutions are well-developed and readily available at present. For example, numerous work involving one or more of the aforementioned deconvolution methods has been reported for characterizing the mechanical properties of multiphase composites using nano/micro indentation (Hou et al. 2016, 2019; Lu et al. 2020; Luo et al. 2020; Wu et al. 2020; Zhang et al. 2017). In fact, most of the aforementioned materials characterization problems usually involve only univariate datasets, offering the PDF-based deconvolution certain advantages over the CDF and GMM. For example, PDF is more visually intuitive than the CDF in terms of the deconvoluted distinct modes, since the mean (i.e., center) and SD (i.e., width) can be directly identified from the plot, while the area under each deconvoluted peak represents its global makeup percentage relative to other modes. In fact, this is probably the same reason why the PDF is the most widely used or preferred mathematical function of a variate, and hence the PDF plays a vital role in data processing and analyses. The PDF is typically used to account for the likelihood or probability of the variate taking a specific value that is within a particular range, but not one particular value. Such a probability is defined by the area under the PDF confined between the data range.

The PDF-based deconvolution starts first with the construction of a histogram, or a discretized graphical presentation of the dataset of more or less continuous numbers, which is the most widely used and straightforward graphical description of a dataset. Histogram construction in turn requires data binning, a pre-processing technique for grouping the datasets into a smaller number of bins. In other words, a properly selected, rational bin size/width (b) is necessary to bin and group the individual measurement data into different intervals so that the number of data falling within each interval (i.e., bin) can be counted and hence the occurrence frequency within each bin determined. It is only after an appropriate and rational bin size or number of bins (N_b) is determined that a truly representative histogram can be obtained. In general, the bins must be adjacent with an equal size, but sometimes unequal bin sizes are necessary for processing the statistical data of a variate. Different bin sizes can reveal different features of the measurement data. Wider bins can accommodate more data, leading to a smaller number of bins or the underlying occurrence frequency bars, and hence reduce the noise due to the sampling randomness, a phenomenon also called “oversmoothing”. In contrast, narrow bins result in more underlying occurrence frequency bars, and hence the histogram is more sensitive to the sampling noise, or “undersmoothing”. Therefore, varying the bin size for a given dataset can result in different histograms and differently fitted, or sometimes misleading, PDFs with varying degrees of error.

However, to date, the method to determine the “best” number of bins or a rational, optimized bin size is not yet universally available or accepted. Many attempts have been made in the past by theoreticians or statisticians to propose different criteria to estimate the optimal bin sizes (Freedman and Diaconis 1981; Scott 1979; Shimazaki and Shinomoto 2007; Sturges 1926; Terrell and Scott 1985; Wand 1997) required for data binning and subsequent histogram construction or PDF deconvolution. Most of these binning methods suggest a bin size that is highly dependent upon the total number (*n*), and to a lesser extent the maximum and minimum, of the measurement data in the dataset. In particular, the Freedman-Diaconis rule (Freedman and Diaconis 1981) yields a relatively better estimate of the bin size due to the adoption of the interquartile range (*IQR*), which makes the estimated *b* less sensitive to the maximum and minimum but the standard deviation of the dataset. In some other cases, the selection of an appropriate bin size is simply based on personal experience and judgment, or even a rule of thumb. In summary, despite of these proposed rules, selection of a rational bin size is still largely empirical and mostly a matter of individual choice, but not objective or free of personal judgment.

In this paper, a new “data binning” approach, termed the “Bin Size Index (BSI)” method, is proposed to determine the optimal bin size required for the construction of histograms of multimodal datasets that are then used for PDF-based deconvolution. A wide variety of datasets were examined, including four normally-distributed synthetic datasets with varying the number, mean, SD, and fraction of different modes, three normally-distributed, real measurement datasets on the small-scale, local Young's moduli of three sedimentary rocks obtained by nanoindentation, and three log-normally distributed datasets on the PSD of flocculated illite suspensions. Validation of the fitting accuracy by the synthetic datasets with known distributions can expectedly manifest the effectiveness of the BSI method in selecting an optimal bin size for constructing the histogram to be used subsequently for the PDF-based statistical deconvolution, especially for multiphase materials characterization. This process also leads to the clearly and separately identified individual modes as well as the determination of the number, mean, SD, and fraction of each identified mode contained in the statistical dataset.

3.2 The New binning method

The generalized problem of data binning is first described here, followed by the detailed concepts and algorithms of the new BSI method. A multimodal variate *x* can be assumed to obey Gaussian or normal distributions, since it is the most popular and widely observed statistical function accounting for various natural and artificial phenomena (e.g., the height patterns of specific populations can be mostly modeled with a normal distribution, the size of living tissues basically follows a lognormal distribution but can be described by a normal distribution after the logarithmic transformation), and plays an essential role in approximating other fundamental statistical distributions (e.g., binomial distribution, Poisson distribution, chi-squared distribution, Student's t-distribution). Then a *K*-mode PDF of such a variate can be written as:

$$f(x) = \sum_{j=1}^{K} A_j f_j \left(x \mid \mu_j, \sigma_j \right) \tag{3.1}$$

where $f(x)$ and $f_j(x)$ (j = 1, 2, 3, …, K) are the global and individual mode's Gaussian PDFs respectively; A_j, μ_j, and σ_j the fraction, mean, and SD of the j-th mode, respectively. Overall, the coefficients A_j are constrained by:

$$\sum_{j=1}^{K} A_j = 1.0 \tag{3.2}$$

Appropriate sampling or measurement of the variate x repeated by n times results in a multimodal dataset $\boldsymbol{X}$, a one-dimensional matrix with n elements. To better understand the variate x, the dataset $\boldsymbol{X}$ needs to be analyzed statistically, particularly for the determination of the statistical properties of all modes, including K, A_j, μ_j, and σ_j, via statistical deconvolution. As stated earlier, PDF-based deconvolution is typically preferred over other counterparts, which starts with the selection of an appropriate bin size b to construct the histogram of the dataset $\boldsymbol{X}$, $H(\boldsymbol{X})$. The goal of deconvolution is to minimize the error $E(x)$ between the real but unknown analytical PDF $f(x)$ and the histogram $H(\boldsymbol{X})$:

$$E(x) = f(x) - H(\mathrm{X}) = E(b, K, A_j, \mu_j, \sigma_j) \tag{3.3}$$

That is, the error $E(x)$ is a function of five variables shown in the above equation, of which the b is the most important since it is necessary to initiate the deconvolution.

The newly proposed BSI method consists of a series of computational algorithms leading to the selection of the optimal bin size, b_{opt}. First, the Freedman-Diaconis rule (Freedman and Diaconis 1981) is adopted to generate an initial trial bin size b_0 for the dataset $\boldsymbol{X}$:

$$b_0 = \frac{2 \times IQR(\mathrm{X})}{n^{\frac{1}{3}}} \tag{3.4}$$

where *IQR* is the interquartile range of the considered dataset. Then six or more different trial bin sizes, b_m ($m = 1, 2, 3, \ldots, 6$) $< b_0$, are selected, preferably covering a wide range with a small but equal difference:

$$\Delta b = b_{m+1} - b_m \tag{3.5}$$

The reason for $b_m < b_0$ is that larger bin sizes always result in a relatively higher normalized standard error and smaller BSI (as defined later), according to preliminary work. Therefore, the b_0 determined by the Freedman-Diaconis rule can serve as a starting upper bound for other trial bin sizes b_m.

Each of the 7 different bin sizes is then used to construct its own histogram, followed by statistical deconvolution with widely and commercially available software, such as PeakFit (Li et al. 2021; Luo et al. 2020). In this study, however, fitting the histogram with PDF was performed with the Origin Peak Deconvolution Function (Originlab Technical Support, USA) under the assumption that the variate x obeys a multimodal Gaussian distribution described by Eq. (3.1). Particularly noteworthy is that the variable K, the total number of modes, is not independent, but varies with the bin size b. For a given histogram, the mode K should in theory be varied to find the best fit PDF by minimizing the $E(x)$, starting from $K = 1$ to a maximum $K_{\max}$. In many cases, however, the modes of a histogram constructed for a given b may be visually identified and discerned, or are clearly separated apart, and hence there is no need to vary K further in the deconvolution. The $K_{\max}$ is determined by two conditions (as discussed later): (1) it is constrained by the degree of freedom, and (2) for real measurement data, other accompanying results (e.g., the mineralogical composition of a rock determined by X-ray diffraction) may also be used to aid the selection of K_{max}.

This step of histogram fitting yields a certain number of modes K, as well as the mean, SD, and fraction of each mode. As such, the overall analytical (or deconvoluted) multimodal PDF (i.e., Eq. (3.1)) encompassing K modes can be determined. Usually this PDF does not match exactly with the histogram constructed by the particular bin size b. To quantify the goodness of fit or the error between the analytical PDF and experimental histogram, the least-squares criterion, a routine method used in most statistical analysis for minimizing the sum of squares due to error (*SSE*), is herein performed:

$$SSE = \sum_{i=1}^{N_b} w_i \left(\hat{y}_i - y_i\right)^2 \tag{3.6}$$

where N_b is the total number of bins, y_i and $\hat{y}_i$ are the i-th bin occurrence frequency and probability of the experimental histogram and analytical PDF respectively, and w_i is the weight applied to the i-th bin, which is usually equal to 1.0. The degree of freedom (*DOF*) is defined:

$$DOF = N_b - 3K - 1 \tag{3.7}$$

The standard error (S_E) for each trial bin size can then be calculated by:

$$S_E = \sqrt{\frac{SSE}{DOF}} \tag{3.8}$$

To obtain a rational S_E, the *DOF* must be an integer greater than or equal to 1. As such, the maximum K should be $K_{max} = (N_b - 2)/3$. The above process is repeated for all trial bin sizes, resulting in multiple S_E values with a mean μ_S and SD σ_S. In consideration of the potential variations in the S_E values obtained from all different trial bin sizes, which can differ by more than one order of magnitude and are much smaller than 1.0, a step of mean normalization of S_E is further proposed to obtain the mean-normalized residual standard error S_{EN} whose values are scaled up to ~1.0:

$$S_{EN} = \frac{|S_E - \mu_S|}{\sigma_S} \tag{3.9}$$

Finally, a new quantitative parameter, termed as "bin size index" (*BSI*), is defined for the first time in this paper to further evaluate the accuracy of the above deconvolution and curve fittings for each of the trial bin sizes:

$$BSI = \frac{|2 \times \ln(\mathrm{S}_{\mathrm{EN}})|}{K} \tag{3.10}$$

In general, $S_{EN} < 1$, and hence $\ln(S_{EN})$ is always negative. The smaller the S_{EN}, the greater the BSI. Clearly, the determined BSI values based on the above equations are primarily regulated by the S_E obtained at each bin size. Therefore, a finite number of modes $K \leq K_{max}$ can be tried at each trial bin size and the one yielding the highest BSI is selected as the correct number of modes deconvoluted at this particular trial bin size. Then plotting the BSI against b yields a unimodal peak or multiple peaks, and the peak with the highest BSI should be used to find the b_{opt}.

In summary, each S_{EN} is objectively determined by comparing individual S_E and the mean μ_S of all S_E values, followed by the normalization by the standard deviation σ_S. As discussed in the analysis of real measurement data, quite often, the lowest S_{EN} usually corresponds to the highest BSI, which corresponds to the b_{opt}. In other words, the *BSI* is intentionally penalized by the number of modes K so that the normalized standard error is shared by the number of modes K. All other statistical parameters, including K, A_j, μ_j, and σ_j in Eq. (3.1) can be determined by deconvoluting the histogram constructed by the b_{opt}. Although other trial bin sizes are used to construct different histograms that are also deconvoluted, their results are used to calculate the *BSI* and hence aid the selection of the maximum *BSI* and hence the b_{opt}.

In fact, the underlying concept of *BSI* is inspired by the maximum likelihood-based criteria such as Akaike information criterion (AIC; (Akaike 1974)) and Bayesian information criterion (BIC; (Bhat and Kumar 2010)). The AIC is defined by

$$AIC = 2\mathrm{k} - 2\ln(\hat{L}) \tag{3.11}$$

where $k = (3K - 1)$ is the total number of free parameters in the fitting model (Eq. (3.1)), and $\hat{L}$ is the maximum value of the likelihood function. Eq. (3.11) can then be expressed in terms of *SSE* when the residual errors are assumed to follow an independent identical normal distribution with a mean of zero:

$$AIC = 2\mathrm{k} + n\ln(SSE/n) \tag{3.12}$$

Similarly, the *BIC* is expressed as:

$$BIC = \mathrm{k}\ln(n) - 2\ln(\hat{L}) \tag{3.13}$$

or in terms of *SSE*:

$$BIC = \mathrm{n}\ln(SSE/n) + k\ln(n) \tag{3.14}$$

The BSI definition follows the same mathematical algorithms used for AIC and BIC: while the AIC and BIC first average the *SSE* by the number of data entries, n, of the datasets and then perform logarithmic transformation, the BSI first performs the logarithmic transformation of the S_{EN}, followed by the penalization or averaging of the $\ln(S_{EN})$ by the number of modes. Moreover, if $K = 1$, the algorithms of the AIC, BIC, and BSI are similar, except that the former two use the n for averaging, while the latter uses the DOF but not n for averaging and contains an extra step for normalizing the SSE or S_E to S_{EN} (Eq. (3.9)).

3.3 Data description and collection

3.3.1 Synthetic datasets

The general statistical accuracy and effectiveness of the proposed BSI method were first investigated and validated by synthetic datasets that were generated by a random number generator (i.e., the built-in "Random Number Generation" data analysis tool) in the Microsoft Excel program (Microsoft Corporation, USA). First, several individual unimodal subdatasets, each of which corresponded to one particular mode of a variate obeying a unimodal normal distribution, were generated under the preset statistical parameters, including the number of data entries, mean, and SD of the normal distribution. Then a selected number (i.e., the mode number $K = 3$ or 5) of different subdatasets were merged into one integrated master dataset, which became a multimodal distribution. In total, four different multimodal datasets (i.e., identified by I, II, III, or IV) with varying the number, mean, SD, and fraction of all modes were created for different purposes (Table 3.1). For example, while Datasets I and II consists of 3 modes, the rest two have 5 modes. On the other hand, all modes of Datasets I and III had equal fractions (i.e., each mode has 1,000 and 3,000 data entries for Datasets I and III respectively), the other two counterparts have unequal fractions of different subdatasets (Table 3.1).

Table 3.1 Summary and comparison of the pre-set versus deconvoluted statistical parameters for the four synthetic multimodal datasets following a normal distribution

Dataset ID (type)	Mode ID (# of data)	Mean (μ)		Standard deviation (σ)		Fraction (A) (vol.%)	
		Pre-set	Deconvoluted	Pre-set	Deconvoluted	Pre-set	Deconvoluted
I (equal fraction)	1 (1,000)	200.00	202.30	10.00	10.29	33.33	33.81
	2 (1,000)	220.00	233.18	10.00	9.79	33.33	38.10
	3 (1,000)	240.00	255.60	15.00	13.66	33.33	28.09
II (unequal fraction)	1 (3,000)	300.00	300.00	10.00	10.23	50.00	50.00
	2 (1,000)	320.00	320.00	15.00	12.81	16.67	16.70
	3 (2,000)	340.00	340.00	30.00	28.85	33.33	33.30
III (equal fraction)	1 (3,000)	200.00	203.83	10.00	10.32	20.00	20.05
	2 (3,000)	300.00	303.09	20.00	19.77	20.00	19.43
	3 (3,000)	360.00	364.21	18.00	19.65	20.00	21.17
	4 (3,000)	400.00	404.04	15.00	15.26	20.00	19.26
	5 (3,000)	450.00	451.15	21.00	21.49	20.00	20.08
IV (unequal fraction)	1 (3,000)	200.00	201.88	10.00	10.30	15.00	15.20
	2 (2,000)	250.00	251.02	20.00	18.52	10.00	9.48
	3 (4,000)	310.00	312.59	15.00	15.81	20.00	21.86
	4 (5,000)	360.00	363.40	25.00	22.95	25.00	22.93
	5 (6,000)	415.00	416.65	18.00	17.79	30.00	30.53

To guarantee sufficiently distinguished contrast between any two adjacent modes (i.e., by preventing excessive overlap of two neighboring unimodal distributions so that the two modes would not be treated as one single mode) (DeJong and Ulm 2007), a constraint was added to the data generation:

$$\mu_j + \sigma_j < \mu_{j+1} + \sigma_{j+1}, j = 1, 2, \ldots, K \tag{3.15}$$

The proposed BSI method were then applied to process and deconvolute the four multimodal datasets so that the statistical parameters, including the number of modes, mean, SD, and fraction of each mode, were determined. During the deconvolution, although the number of modes K was known, the range of tried K values was intentionally increased, i.e., $K = 1$ to 6 (= $K_{\max}$) for Datasets I and II and 1 to 7 (= $K_{\max}$) for Datasets III and IV, to examine the BSI method's effectiveness in determining the correct number of modes. In addition, many different initial values of the mean, SD, and fraction of all modes were needed to start with the fitting, and a proper histogram could aid the selection of these initial values.

3.3.2 Datasets on the elasticity of rocks

As the first example, the datasets on the elastic modulus of natural rocks were used to validate the viable applications of the BSI method. Heterogeneous composite materials usually consisting of multiple, compositionally distinct but structurally-integrated constituent phases across different scales (i.e., from nano- to macro-scales) are extensively manufactured and widely used for various functionalities in practice, such as metal foams (Zhao et al. 2004), ceramics (Men et al. 2013), polymers and biomaterials (Sumbekova et al. 2019), and Portland cement-based concretes. Besides the artificially engineered composites, naturally occurring counterparts are also abundant and frequently encountered in human activities, such as rocks and woods. One feature common to all these materials is that their mechanical properties (e.g., strength, stiffness) are affected by the properties of individual constituents and the fashion through which these constituents interact across different scales (i.e., from the nanoscale particles at the order of ~ tens of nanometers to a few micrometers, to mesoscale structural units, and to macroscale bulk material at the length scale of a few millimeters to meters). For example, as a representative kind of fine-grained sedimentary rocks, shales are formed by the deposition of primarily cohesive suspended sediments (e.g., clay minerals) together with minor coarse-grained sand and silt particles in natural water environments (e.g., rivers, oceans), followed by subsequent long-term (e.g., millions of years) geological processes (e.g., compaction, consolidation, diagenesis, tectonic stressing), during which a complex composite structure is developed involving multiple mineral constituents and associated interactions such as degree of packing, particle arrangements, interparticle contacts, and cementation (Bennett et al. 2015; Han et al. 2018; Li et al. 2017; Wu et al. 2020). As such, shales are typically made of a fine-grained, relatively homogeneous, clay mineral-based matrix and other hard minerals as solid inclusions randomly distributed within the matrix. Characterizing the in-situ mechanical properties of the matrix and the solid inclusions requires small-scale mechanical testing techniques such as nanoindentation.

Since its initial inception (DeJong and Ulm 2007), statistical grid nanoindentation has evolved as a convenient, fast experimental technique to probe the in-situ mechanical properties such as elasticity and hardness of individual constituent phases of multiphase composites such as rocks and concretes. More recently, big data-based nanoindentation has also been developed to characterize the cross-scale elasticity of shales and sandstones, i.e., the elastic moduli of individual constituents at the nano/micro scale and of bulk rock as a composite at the meso/macro scale (Luo et al. 2020). One key hypothesis for this technique is that each of the probed mechanical properties of individual phases is a multimodal variate obeying a normal distribution, and thus a massive number of measurements required to ensure statistical accuracy, particularly for the determination of the fraction of different constituent phases, constitute a multimodal dataset. For instance, the Young's modulus data obtained by nanoindentation randomly probing numerous locations on the sample surface constitute a multimodal dataset. The utmost important step for this grid nanoindentation approach is the statistical deconvolution of the dataset to determine the number, mean, SD, and fraction (i.e., in terms of area or volume) of all different modes or constituent phases of a composite. To date, various statistical analysis methods have been developed, including the K-means clustering, PDF, CDF and multivariate GMM, of which the PDF-based deconvolution is the most widely used, most likely due to its easy implementation, straightforward concepts, and intuitive graphic presentation. However, the PDF-based deconvolution is conducted on the experimental histograms whose construction requires the selection of an appropriate and rational bin size (or equivalently the number of bins).

To validate the effectiveness of the BSI methods in characterizing the mechanical properties of multiscale, multiphase sedimentary rocks, grid nanoindentation measurements on two sandstones (hereafter abbreviated as KS-45 and KS-52) and one shale (hereafter referred to as Longmaxi shale due its origin) were selected and analyzed. Experimental details on the samples, sample preparation methods, and measurement procedures can be found in prior publications: Li et al. (2021) for the two sandstones, and Lu et al. (2020) for the shale. In brief, nanoindentation testing was conducted on the highly polished disk specimens in a Keysight G200 nanoindenter (Keysight Technologies, Inc., Santa Rosa, Ca) equipped with a Berkovich diamond indenter with a tip radius of < 20 nm under the continuous stiffness measurement (CSM) mode. As such, the Young's modulus from each of the ~1029 indents was continuously obtained over the entire indentation depth of up to ~8 μm. As examples, the datasets for the Young's modulus extracted at indentation depth of 500, 150, and 350 nm for the KS-45, KS-52, and Longmaxi shale, respectively, were selected for statistical analysis. Further noteworthy is that the mineralogical compositions of these three rocks were also analyzed by qualitative and quantitative X-ray powder diffraction (XRD) (Ref. Li et al. 2021, Lu et al. 2020). Such results can be used to partially validate the accuracy of the proposed BSI method, since the statistical deconvolution can also yield the quantitative fractions of different mineral constituents in these rocks. With the XRD results, the $K_{\max}$ was pre-set as 9, 7, and 8 for the KS-45, KS-52, and shale, respectively.

3.3.3 Datasets on the PSD of flocculated clay suspensions

The second representative example used to illustrate the BSI method's applicability is the PSD of flocculated clay suspensions. Natural waters are usually loaded with suspended cohesive sediments, which are, unlike the sand/silt or other coarse-grained sediments, primarily composed of different types of platy-shaped clay minerals with nano and submicrometer sizes (e.g., < 2 μm), large specific surface areas, and chemically active surfaces (i.e., permanent negative charges on face surface and pH-dependent charges on edge surface) (Maggi 2005; Mikkelsen et al. 2006). These features lead to intensive interactions (e.g., flocculation and aggregation) among primary clay particles themselves and other suspended particulate matter (e.g., extracellular polymeric substances, EPS) that also has surface charges or chemically active functional groups, resulting in complex, multimodal PSD with different-sized particle groups. For instance, prior work showed that primary clay particles, flocculi, microflocs, and macroflocs could form as a result of counterbalanced effects of continuous flocculation versus breakage in the hydrodynamic water environments (Jarvis et al. 2005a; Lee et al. 2012; Zhang et al. 2013b). Knowledge of the complex PSD of suspended sediments is of essential importance for sediment and coastal shoreline management, and predictive modeling of sediment transport and fate, which play a vital role in the sustainable development and management of natural water environments (Hill 1998). Moreover, it is well known that the PSD of naturally occurring soils, deposits, and suspended sediments can be best described by a lognormal distribution. To further validate the applicability and performance of the BSI method for binning lognormally distributed, multimodal datasets, experiments were designed and conducted to obtain the PSD data of flocculated clay suspensions.

High-purity illite (IMt-1) acquired from the U.S. Clay Minerals Society Source Clay Repository (Purdue University, Indiana, USA) was used to prepare flocculated clay suspensions for PSD measurements, owing to its abundance in terrestrial and marine cohesive sediments. The as-received rock chips of illite were first wet-ground to a fine powder of < 20 μm in size. Following previously developed procedures (Tan et al. 2017), the ground illite of 0.12 g was first soaked in a centrifuge tube filled with 10 mL deionized

(DI) water for > 16 hrs, followed by mixing for 10 mins in a blender with additional 290 mL DI water, resulting in an illite suspension of 0.4 g/L in concentration. The purpose of these disintegration and dispersion steps was to obtain the truly primary clay particles for the formation of representative illite flocs, instead of the pre-existing aggregates in the samples.

To promote flocculation and simulate the hydrodynamic shearing in turbulent flows, the above clay suspensions with an original pH 8.61 were altered to have a 35 ppt NaCl salinity and three pH values, 8.61, 4.51, 2.25, the latter of which was adjusted through titration by 0.1 M HCl solution, since clay minerals such as illite tend to form repulsion in a clean or basic suspension. Flocculation of the suspended illite particles was then achieved by continuously vibrating at a speed of 150 oscillations/min for 24 hours the aforementioned clay suspension in a Burrell Model 95 wrist-action shaker (Burrell Scientific, LLC., USA). Such flocculated clay suspension was then transferred by a pipette to 10 to 15 clear and transparent Petri dishes to allow settling of particles for at least 24 hrs. Then each Petri dish was placed in a FemoTools FT-UMS 1002 universal measurement stand with a digital microscope (Nanoscience Instruments, Inc., Pheonix, AZ, USA) to capture >20 images on different locations at the Petri dish bottom surface for broader but no overlapping coverage, to ensure better accuracy and representativeness of the imaged particles.

Image analysis using Image J, an open-source, Java-based software developed and distributed by the U.S. National Institutes of Health (NIH), was conducted to measure the particle sizes, using the widely-accepted systematic procedures (Mazzoli and Moriconi 2014; Strom et al. 2010; Tajima and Kato 2011). It basically involved a few key steps: (1) converting the original color images to 8-bit grayscale counterparts; (2) subtracting the uneven background light; (3) contrasting and segmenting to differentiate the particle boundary; (4) thresholding for producing a binary image of black colored particles with a white background; (5) measuring particle sizes by the built-in "Analyze Particles" function. These steps were herein adopted as the reference procedures for analyzing the captured images of illite flocs settled to the bottom of each Petri dish. The equivalent circular area diameter, d_s, was selected to represent individual particle or floc sizes, which can be calculated by:

$$d_S = \sqrt{\frac{4S}{\pi}} \tag{3.16}$$

where S was the measured area of the particle via image analysis. For each of the pH values, particle size data collected from all >20 captured images were merged into a unified dataset, resulting in three separate datasets containing 10,411, 5,357, and 3,285 data entries for the pH 8.61, 4.51, and 2.25 suspensions, respectively, which were then analyzed by the BSI method. Finally, the $K_{\max}$ selected for these three datasets were 11, 9, and 9 for the pH 8.61, 4.51, and 2.25 illite suspensions, respectively.

3.4 Results and Discussion

3.4.1 Analyses of synthetic datasets

The BSI method-derived deconvolution results of the four synthetic datasets (i.e., I, II, III, and IV), consisting of the number, mean, SD, and fraction of all modes, are compared in Table 3.1 with the known counterparts used for generating the random numbers making up each respective dataset, while Figure 3.1 shows the histograms and deconvoluted PDF plots for the b_{opt} and the relationships of the BSI versus b and S_{EN} versus b for all four datasets. Also, for each trial bin size b, the pertinent deconvoluted number of modes K is also summarized in Figure 3.1. The initial bin size b_0 determined by Eq. (3.4) for the four synthetic datasets are 5.0, 3.0, 11.0, and 8.5 respectively, while the corresponding b_{opt} are 3.5, 2.0, 8.0, and 4.0, respectively.

According to Table 3.1 and Figure 3.1, the deconvoluted number of modes (i.e., $K = 3$ for Datasets I and II, and $K = 5$ for Datasets III and IV), and the mean, SD, and fraction of each mode agree remarkably well with the pre-set counterparts, validating the BSI method's accuracy and effectiveness. First, the fitting PDFs and histograms are consistent, and the number of modes deconvoluted at the b_{opt} is exactly the same as the pre-set initial K, especially for Datasets II and III that contain densely overlapped modes (Figures 1b and 1c). Second, based on the BSI versus b plots (Figure 3.1e to 1h), multiple local but smaller BSI peaks exist in all figures, which seems not to affect the selection of the b_{opt} corresponding to the global maximum.

Although prior work (Luo et al. 2020) claimed that the BSI versus b plots should exhibit a unimodal peak, it is not uncommon to observe multiple localized peaks in such plots. This discrepancy can be primarily attributed to the variations in the standard error, S_{E}, obtained from each deconvolution fitting, as shown in that compares the S_{E} and corresponding S_{EN} for different b values. Clearly, for all four synthetic datasets, the S_{E} generally decreases with increasing the b, because a larger bin size leads to underfitting (or oversmoothing) of the datasets and hence the reduction of some data features. There still exist different degrees of fluctuations of S_E as the b increases. Also, the penalization to the normalized standard error S_{EN} by the number of modes K affects the variations of resulting BSI. For example, in Figure 3.2, while all BSI show the opposite trend against the corresponding S_{EN} (i.e., the highest BSI basically corresponds to the smallest S_{EN}), Figure 1f shows that the highest BSI is reached at $b = 2.0$ instead of $b = 1.5$ that yields the smallest S_{EN}, which is due to the different number of modes at these two trial bin sizes (i.e., $K = 3$ at $b = 2$, while $K = 4$ at $b = 1.5$).

Finally, for all synthetic datasets, the b_{opt} selected by the BSI method is usually smaller than the b_0 estimated by the Freedman-Diaconis rule, but close to the median of the several trial bin sizes (Figure 3.1), which indirectly validates the core concept of the BSI method: the b_{opt} optimized for the construction of appropriate histograms should reflect a rational and successful trade-off between overfitting and underfitting. In fact, the fitting results for those bin sizes > b_{opt} tend to underfit the measurement data and hence less accurate due to the smaller number of identified modes, while those bin sizes < b_{opt} can also lead to higher fitting errors, as shown by both the S_E and S_{EN} (Figure 3.2), which is due to overfitting and the loss of generalization but too many uncaptured local features.

It is also noteworthy to discuss how the b affects the fitting errors for each mode, including its mean, SD, and fraction. In this regard, since the number of modes in each synthetic dataset was known, the fitting errors were determined based on a fixed mode number (i.e., 3 or 5 for the four datasets) but varying the bin size. That is, the effects of b on the accuracy of estimating the modes' statistical parameters (i.e., mean, SD, and fraction) under a constant K were examined. The root-mean-square (RMS) of errors

(RMSE) between the given and deconvoluted means, SDs, and fractions (Table 3.1) of all modes for each trial b was calculated, and results are compared in Figure 3.3. The RMSE in the mean values of each dataset increases nearly linearly or is generally dependent on the bin size. This phenomenon agrees well with the common understanding that larger bin sizes tend to underfit the data, but help reduce the noises resulting from the measurement randomness at the expense that the deconvolution accuracy for the parameters is lowered, while smaller bin sizes usually yield higher precision (or even overfitting). However, such a trend is not observed for the RMSE in the SDs and fractions for all four datasets. That is, the RMSE of the SDs or fractions is relatively independent on the bin size. Therefore, for a given dataset with the known mode number K, if PDF deconvolution is conducted, the deconvoluted SD and fraction of each mode are less affected by the bin size, but an appropriate bin size is required to estimate the more accurate mean of all modes.

In summary, the b_{opt} selected by the BSI method yields rational histograms that leads to reasonable and accurate deconvolution results, including the number of modes and three statistical parameters of each mode. The BSI at a given bin size is primarily dependent upon the corresponding S_{E}, further adjusted by the normalization effects of all S_{E} values (i.e., S_{EN}) and penalized by the number of modes K. Thus, when a constant K is used for all trial bin sizes, the penalization effects of K on the deconvolution results are theoretically negligible. In most data analyses and applications, however, the K is usually unknown. As such, a maximum K is required to make sure that the *DOF* is greater than or equal to 1. As discussed later, other accompanying measurements (such as XRD discussed in the next section) can help select a K_{max}. Therefore, the total number of fitting cases is limited for a given trial bin size, which simplifies the entire deconvolution process. As a result, a significant advantage of the BSI method is that it yields both the optimal bin size b_{opt} and number of modes K, as well as other routine parameters.

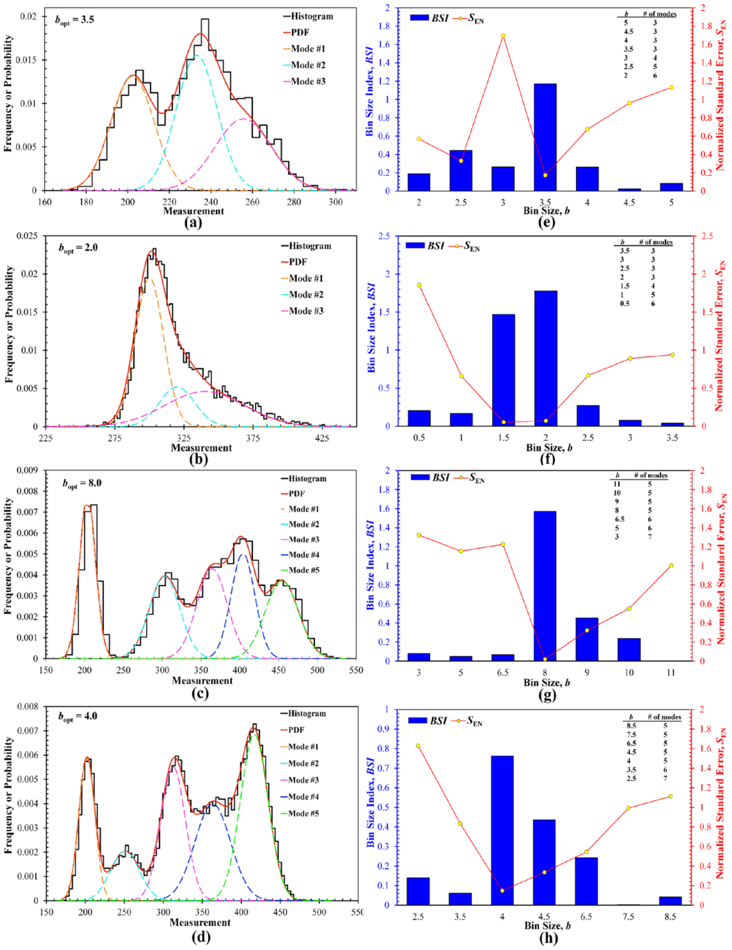

Figure 3.1 Deconvolution results for the four synthetic datasets: (a) to (d): Histogram constructed at the bopt and pertinent deconvoluted PDF distribution for Dataset I, II, III, and IV, respectively; (e) to (h): the relationships between the BSI and bin size and between the normalized standard error SEN and bin size for Dataset I, II, III, and IV, respectively; The global BSI maximum is used to select the bopt. Inset tables summarize the number of modes determined by deconvolution for each trial bin size

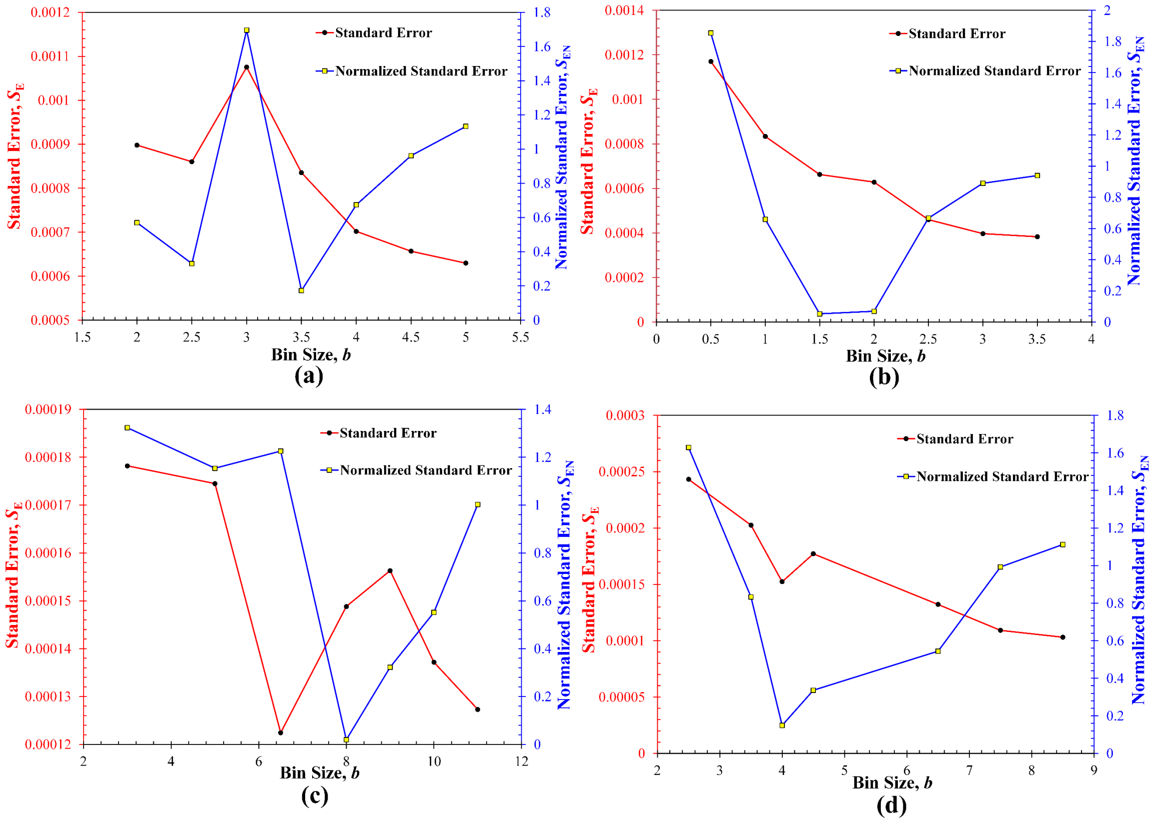

Figure 3.2 Comparison of the dependence of the standard error S_E and normalized standard error S_{EN} on the trial bin size for the four synthetic datasets (a): Dataset I; (b): Dataset II; (c): Dataset III; (d): Dataset IV.

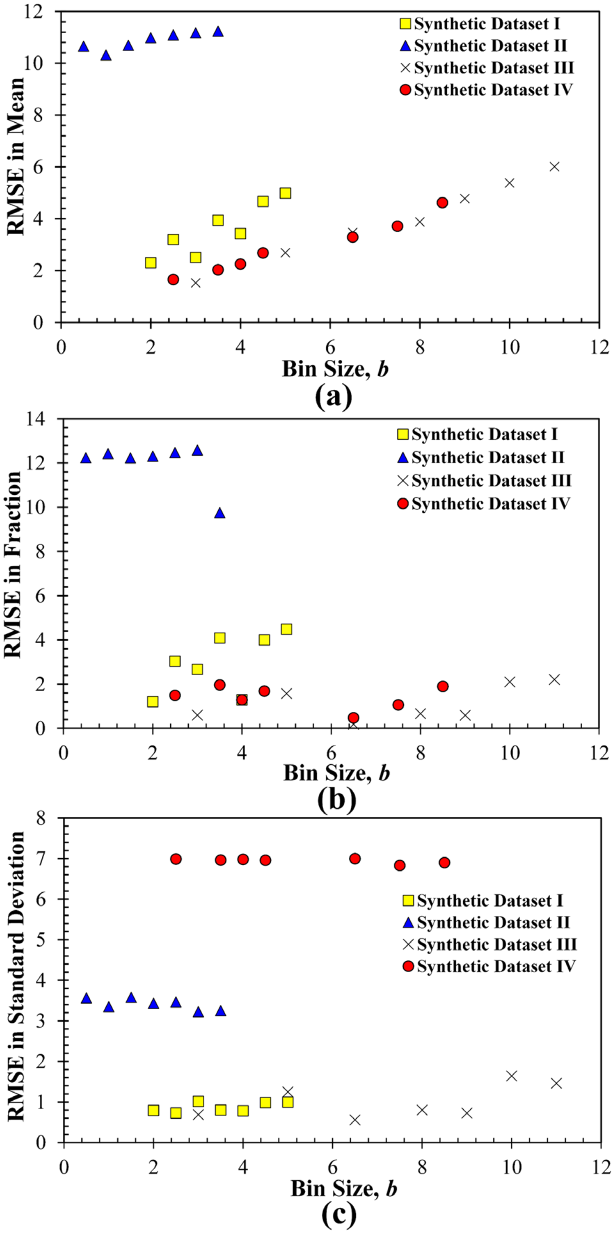

Figure 3.3 The dependence of fitting errors on the bin size if the number of modes is known and fixed for the four synthetic datasets: (a) RMSE in mean; (b) RMSE in fraction; (c) RMSE in standard deviation; RMSE is the RMS of errors between the deconvoluted PDF and measurement histogram.

3.4.2 Analyses of datasets on rock's elasticity

Figure 3.4 presents the obtained XRD patterns of the two sandstones and one shale with all reflections labeled for the identified mineral phases, and quantitative weight-based fractions (wt.%) are accordingly summarized in Table 3.2. With the known specific gravity G_s of different minerals reported in the literature (Dean 1990; Huang et al. 2015), the volume-based fractions (vol.%) can then be determined. These results, including the number of modes (i.e., phases) K and fractions A_j can be in turn used as the initial trial inputs for the PDF-based deconvolution of the elasticity datasets of these rocks obtained by nanoindentation.

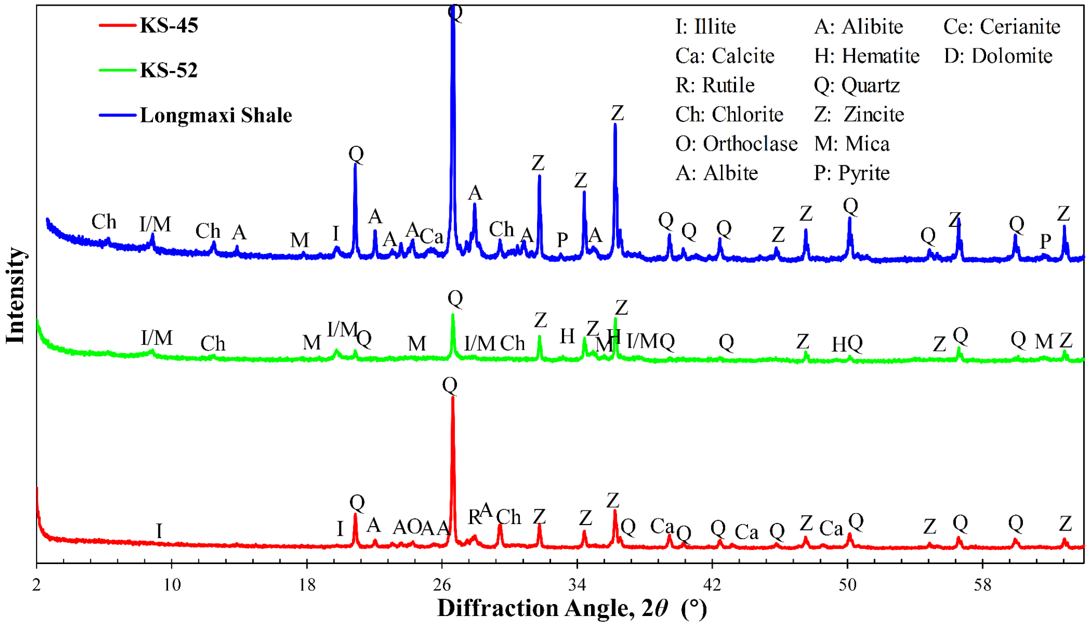

Figure 3.4. XRD patterns of the three studied rock samples.

Table 3.2 Results of qualitative and quantitative mineralogical analyses by XRD for the KS-45, KS-52, and Longmaxi shale.

Mineral	Ideal chemical formula	Specific gravity	Weight fraction (wt.%)			Volume fraction (vol.%)		
			KS-45	KS-52	Shale	KS-45	KS-52	Shale
Quartz	SiO_2	2.65	53.23	17.99	43.40	53.50	19.57	43.80
Orthoclase	$KAlSi_3O_8$	2.61	6.06	/	/	6.18	/	/
Albite	$NaAlSi_3O_8$	2.61	18.17	2.31	23.40	18.54	2.55	23.60
Biotite	$K(Mg, Fe)_3(AlSi_3O_{10})(F,OH)$	3.05	/	5.18	/	/	4.90	/
Muscovite	$KAl_2(AlSi_3O_{10})(F,OH)_2$	2.88	/	25.56	12.00	/	25.58	10.90
Calcite	$CaCO_3$	2.71	13.09	1.67	2.30	12.86	1.78	2.20
Illite	$KAl_2(AlSi_3)O_{10}(OH)_2$	2.69	8.10	24.66	10.00	8.01	26.42	8.90
Chlorite	$Mg_5Al(AlSi_3)O_{10}(OH)_8$	3.20	/	19.30	5.20	/	17.38	5.30
Hematite	Fe_2O_3	5.26	/	3.33	/	/	1.82	/
Rutile	TiO_2	4.01	1.35	/	/	0.90	/	/
Pyrite	FeS_2	5.10	/	/	2.00	/	/	1.30
Organic matter	/	1.06			1.70		/	4.00

Prior to the histogram construction, extra effort is still needed to categorize and combine certain different mineral phases, because of two reasons: (1) nanoindentation with finite but not infinitesimal depths has a constrained resolution of detection limits, and hence very small-sized constituents such as clay minerals (e.g., < 2 and ~0.2 μm in planar dimension and thickness respectively), organic matter, and the finer interparticle cementation (e.g., carbonates) or pores, cannot be detected or discerned by nanoindentation (Wu et al. 2020); (2) some constituents may exhibit similar mechanical properties (e.g., Young's modulus), although their crystal structures are totally different and clearly distinguished by XRD as two different phases. As such, a homogenized composite phase, consisting primarily of typical clay minerals (e.g., illite, chlorite) and the similarly-sized pores, pore-filling organic matter, and interparticle cementation, is assigned as a "clay matrix" phase. In addition, some other trace minerals, such as rutile, hematite, pyrite, and calcites, which are present at very small fractions (i.e., KS-52 and the shale have only 1.78 and 2.3 vol.% calcites, respectively), can also be grouped into the clay matrix. On the other hand, some hard minerals (e.g., quartz, feldspar) may have very similar Young's modulus, and hence can be categorized as one unified phase (e.g., a composite phase "QF" stands for the combined quartz and feldspar). This extra data processing usually leads to the number of phases that is less than the counterpart identified by XRD. Finally, due to the finite indentation depths, a virtual phase, termed as "interface", which accounts for the measurements from indents located at the boundary between two mechanically dissimilar phases (e.g., a hard phase versus the clay matrix), should also be considered in the deconvolution (Luo et al. 2020). Noteworthy is that the volumetric fraction of the virtual interface phase should not be counted toward the total composition, but discarded when calculating the actual volumetric fractions of the real but not virtual phases.

The above pre-processing of XRD data yields the maximum for the number of modes, $K_{\max}$, used to simplify the PDF deconvolution, which is 9, 7, and 8 for the KS-45, KS-52, and shale, respectively. Noteworthy is that these $K_{\max}$ values are intentionally increased to avoid the missing of some potential modes (i.e., a smaller $K_{\max}$ might not be able to account for all potential modes). Therefore, for a selected trial bin size, the corresponding histogram can be constructed, and then the number of modes K can be determined and optimized by two different approaches: if different individual modes can be clearly discerned and identified from the histogram, then the K can be manually determined; In contrast, if the modes are not so clearly separated apart but considerably overlapped, then different K values ranging from 1 to $K_{\max}$ are tried in the deconvolution. Finally, for each combination of K and b, many sets of initial input parameters, including the mean, SD, and fraction of each mode, are randomly selected and used for each deconvolution fitting, and the final solution is determined by maximizing the BSI.

Figure 3.5 shows the selected deconvolution results plotted at the b_{opt} for each rock sample, together with the BSI versus b plot for the selection of b_{opt}, while Figure 3.6 compares the two fitting errors, S_{E} and S_{EN}, obtained at all trial bin sizes. Again, the BSI of each rock exhibits multiple local peaks, as reflected by the varying S_{E} and S_{EN} in Figure 3.6. Nevertheless, while the S_{E} of KS-52 increases with decreasing the bin size (Figure 3.6b), the other two rocks, the KS-45 and shale, show certain fluctuations in the S_{E}, although all fittings were performed using the same criterion of maximizing the BSI. This phenomenon may be attributed to the repeated selection of the same number of modes at certain trial bin sizes, particularly the small ones that lead to overfitting and a higher number of modes. Moreover, due to the constraint imposed to each deconvolution fitting to avoid the excessive overlap of any two neighboring modes (Eq. (3.15)), some individual modes that help optimize the global fittings are likely to be omitted, leading to the fluctuations in the resulting S_{E}. Particularly, for all rock samples, the number of phases or modes determined at their respective b_{opt} is consistent with the counterparts determined by the XRD analysis, which thus indirectly verifies the accuracy and effectiveness of the BSI method.

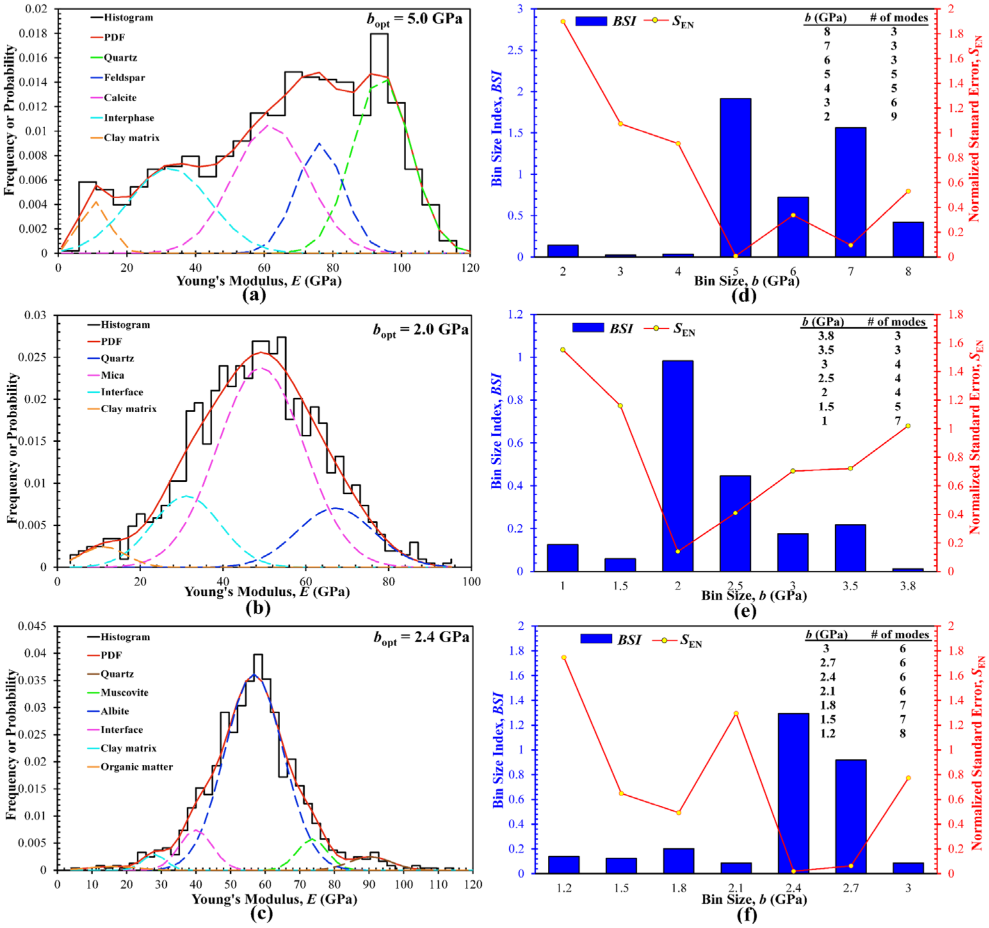

Figure 3.5 Deconvolution results for the Young’s modulus of three rock samples obtained by statistical nanoindentation: (a) to (c): Histogram constructed at the b_{opt} and pertinent deconvoluted PDF distribution for KS-45, KS-52, and shale, respectively; (d) to (f): the relationships between the BSI and bin size and between the normalized standard error S_{EN} and bin size for KS-45, KS-52, and shale, respectively; The global BSI maximum is used to select the b_{opt}. Inset tables summarize the number of modes determined by deconvolution for each trial bin size.

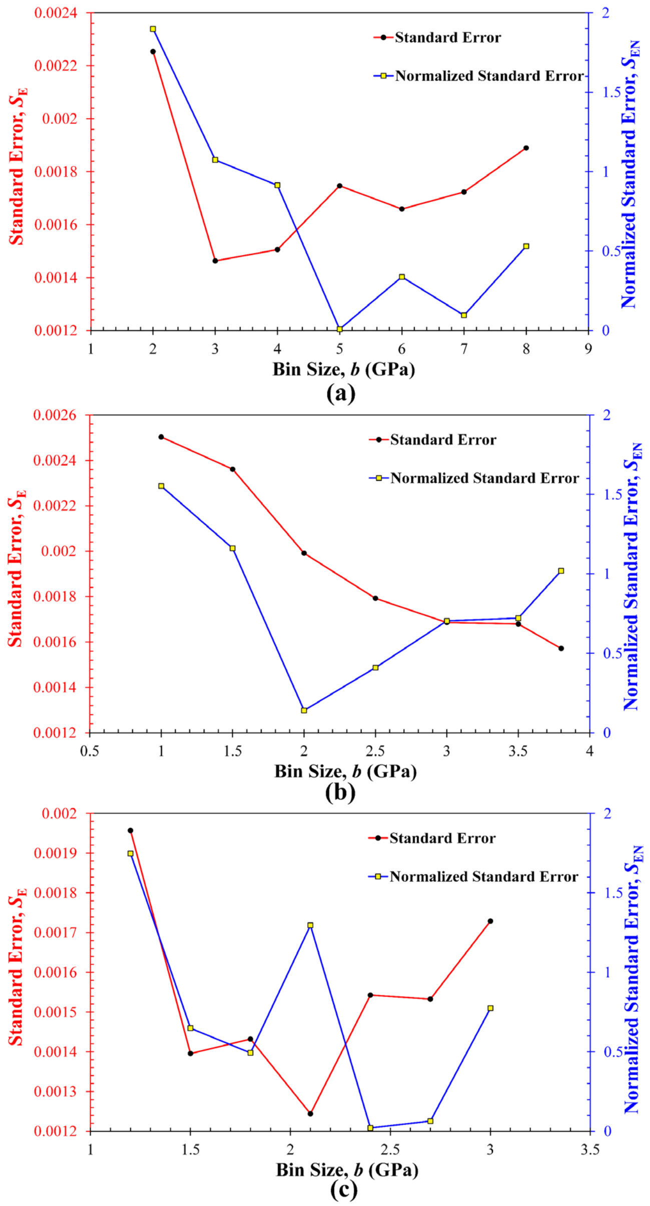

Figure 3.6 Comparison of the dependence of the standard error S_E and normalized standard error S_{EN} on the trial bin size for the elasticity of three rock samples: (a): KS-45; (b): KS-53; (c): Shale.

The above deconvolution leads to the identification of distinct modes from the histograms and the mean, SD, and fraction of each mode. By comparing the published elastic modulus of different minerals with the deconvoluted means, each mode can then be assigned to a particular, mechanically distinct phase in the rocks, and hence the in-situ elasticity of different mineral phases is obtained. Table 3.3 compares the Young's moduli of all the deconvoluted phases with those reported in the literature (Brown et al. 2006; Eliyahu et al. 2015; Heyliger et al. 2003a; Li et al. 2021; Liu et al. 2020b; Lu et al. 2020; Luo et al. 2020; Merkel et al. 2009). Clearly, the Young's moduli derived from the deconvolution are in excellent accordance with those reported in the literature. Some small discrepancies may be explained by a few factual mechanisms. The property obtained by nanoindentation manifests the in-situ response of the considered mineral phases, which is affected by the residual stress, packing density, and to some lesser extent surrounding phases (i.e., the so-called "indentation surround effect") (Lu et al. 2020; Luo et al. 2020; Wu et al. 2020). For instance, the relatively smaller Young's modulus of quartz in the KS-52 is likely due to the small fraction (e.g., 19.57 vol.% quartz) as well as smaller sizes of quartz particles, and hence the mechanical response of the quartz to indentation loading is considerably affected by the larger fractions of surrounding finer particles (i.e., the homogenized clay matrix). Such a "surround effect" accounts for the influence of softer phases such as clay matrix on the mechanical response of the hard inclusions surrounded by the former, or vice versa. That is, the in-situ Young's moduli of the hard inclusions obtained by nanoindentation are reduced by the nearby softer clay matrix that can be included in the expanded elastic zone due to the tiny size of the hard inclusions, even at small indentation depths (e.g., 100 – 200 nm) (Li et al. 2021).

Table 3.3 Summary of the Young's moduli (unit: GPa) of individual minerals or phases for the three rock samples determined by statistical deconvolution of nanoindentation data.

Mineral or phase	This study			Reported value (Reference)
	KS-45	KS-52	Shale	
Quartz	94.24	67.12	90.39	65.01 – 105.80 (Heyliger et al. 2003b; Li et al. 2021)
Feldspar	76.25	/	/	51.10 – 85.0 (Liu et al. 2020b; Wu et al. 2020)
Muscovite	/	/	73.59	69.05 – 77.5 (Lu et al. 2020; Ma et al. 2019)
Calcite	61.79	/	/	64.0 ± 8.00 (Merkel et al. 2009)
Albite	/	/	56.79	59.0 ± 3.00 (Brown et al. 2006)
Mica	/	49.12	/	51.0 ± 4.00 (Li et al. 2021)
Clay matrix	10.62	11.12	27.99	12.0 – 33.10 (Luo et al. 2020, 2021)
Organic matter	/	/	15.99	0 – 25.00 (Eliyahu et al. 2015)

Another important parameter determined by deconvolution is the volumetric fraction of each mode or phase. Figure 3.7 compares the volumetric fractions of different modes (or mineral phases) determined by the deconvolution and by the quantitative XRD for all three rocks. In general, the deconvolution results are approximately the same as those from the XRD. The errors and discrepancies may be caused by some tenable reasons. First, XRD is still a semi-quantitative technique. Although it can work well for those inorganic crystalline solid minerals, its quantification of amorphous and/or organic phases (e.g., organic matter or kerogen in oil/gas shales) is usually semi-quantitative and difficult. Second, nanoindentation measurements are size or length-scale dependent, and are incapable of probing the very small-sized crystals and particles such as clay minerals, clay-sized framework silicates (e.g., quartz, feldspar), and oxides (e.g., hematite, goethite). For instance, the fraction of quartz with particle sizes of < 1-2 μm may not be discernable by nanoindentation and hence may be grouped into the clay matrix phase. In contrast, the larger clay particles (e.g., illite and chlorite) with sizes of > 5-10 μm may be detectable by nanoindentation as an independent phase out of the clay matrix. Finally, as pointed earlier, two minerals with distinct crystal structures but similar elastic moduli can be discerned by XRD but not by nanoindentation. Also, due to the indentation size or surround effect, there is a discrepancy between the results from different indentation depths. In fact, the results from two different indentation depths (Figure 3.7) are expected to be different. Nevertheless, these two sets of results on the volumetric fractions of various mineral phases are relatively consistent.

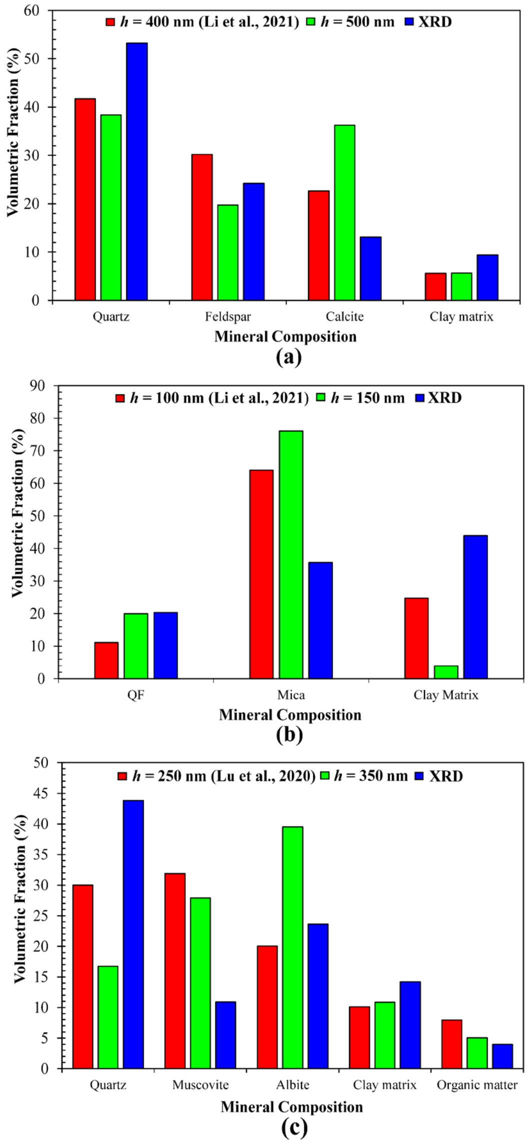

Figure 3.7 Comparison of the volumetric fractions of different minerals in the three rocks determined by quantitative XRD and PDF-based deconvolution of nanoindentation data at a particular deptn *h*. (a): KS-45; (b): KS-52; (c): Shale. Reference data at indeptation depth *h* = 400 and 100 nm for the KS-45 and KS-52, respectively, were extracted from (Li et al. 2021), and *h* = 250 nm were from (Lu et al. 2020)

3.4.3 Analyses of datasets on the PSD of flocculated clay suspensions

As stated earlier, PSDs of cohesive suspended matter and natural deposits can generally be described by a lognormal distribution, most often with multiple modes, each of which represents a subordinate lognormal distribution of the sizes of a distinct particle group. To enable the use of the BSI method, routine pre-processing was performed to transform the original lognormal distribution into a conventional normal distribution. That is, if the dataset measured for the variate of particle size y follows a lognormal distribution $\ln[f(y|\mu, \sigma)]$, then the transformed variate $z = ln(y)$ becomes a normal distribution $f(\ln y|\mu, \sigma)$ (Johnson et al. 2005). Therefore, logarithmic transformation was first performed on the three PSD datasets collected at different pH, followed by the PDF-based deconvolution with the BSI method. An additional benefit of this logarithmic transformation is to detect the possibly hidden particle size groups due to the high skewness of the lognormal distribution that usually leads to the concentration of data with smaller values.

Figure 3.8 presents the deconvolution results, including the PSD histograms plotted at the respective b_{opt} selected by the BSI method and the comparison between the *BSI* and S_{EN}. It should be noted here that, unlike the three rock samples that rely on the quantitative XRD analysis to pre-select the $K_{\max}$, the number of distinct particle size groups (or modes K) used in the PDF-based deconvolution of the PSD histograms cannot be determined in advance, but via multiple trials to determine the correct number of modes that guarantees the minimal fitting errors. Interestingly, the total number of deconvoluted distinct-sized particle groups is higher than that reported in some prior studies considering similar materials and environmental conditions (e.g., pure clay minerals and clay-EPS mixture suspensions in saline or fresh water affected by hydrodynamic shearing) as the substitutes for natural cohesive sediments (Mietta et al. 2009; Tan et al. 2014b, 2017, 2012; Vaezi G. et al. 2011b; Zhang et al. 2013b, 2019a). Such a discrepancy can, to some extent, be due to the logarithm transformation that uncovers the hidden peaks in the originally lognormally-distributed PSDs. Also, the sizes of irregular particles or flocs are defined in this study as the equivalent circular diameter of the particle area measured by optical imaging (Eq. (3.16)). In prior studies, however, different definitions were adopted to represent the measured particle or floc size. For example, Zhang et al. (2013) calculated the particle or floc size based on the volume moment mean value or De Brouckere mean diameter, as expressed with the following equation:

$$d_V = \frac{\sum pVl}{\sum pV} = \frac{\sum pl^4}{\sum pl^3} \tag{3.17}$$

where V and l are respectively the volume and equivalent sphere diameter of a particle or floc, p is the total number of particles or flocs at a fixed size range (i.e., equivalent to the bin size), and d_V is the mean diameter of all particles or flocs within that given size range. The use of such a mean diameter d_V generalizes the size range for particles that may fall into different particle size groups (i.e., deconvoluted modes), and hence the resulting histograms become smoother with less localized peaks to be deconvoluted and identified.

The means of different-sized particle groups or modes are then collected from the transformed multimodal PDFs shown in Figure 3.8, and then further used to calculate the corresponding particle sizes, which manifests a wide, discrete range of particle sizes. Prior studies attempted to conceptually define the particle size groups of suspended cohesive sediments affected by flocculation and hydrodynamic shearing (Andrews et al. 2010; Eisma 1986; Lee et al. 2012; Mikkelsen et al. 2006; Zhang et al. 2013b). Since a standard classification of different particle/floc size groups is yet to be developed, the four-level hierarchical particle size system proposed by Zhang et al. (2013) is followed in this study, and the above deconvoluted modes are assigned to different classified size groups (Table 3.4). Clearly, the pH of a clay suspension can significantly affect the size kinetics of saline illite suspensions: with decreasing the pH, larger-sized particles or flocs (e.g., macroflocs and microflocs) tend to form, while the population of the finer-sized particles (e.g., primary particles and flocculi) decreases. At pH 2.25, the flocculi group with a size range of ~10 to 30 μm even disappears (Figure 3.9). In addition, based on the fraction of each size group, the flocculi and primary particles groups can be regarded as the basic constituents of illite suspensions, which make up the entire, original basic illite suspension (i.e., without acid titration to decrease the pH) and interact with each other or even smaller primary particles to form larger microflocs and macroflocs. Similar findings were also reported in the literature, which reveals the mechanisms of flocculation or stability of aqueous colloidal systems affected by the surface properties and water chemistry (e.g., ionic strength, pH, polymeric electrolyte concentrations) (Gupta et al. 2011; Kang et al. 2019; Konduri and Fatehi 2017; Liu 2001; Liu et al. 2018; Long et al. 2006; Mietta et al. 2009; Wilkinson et al. 2018).

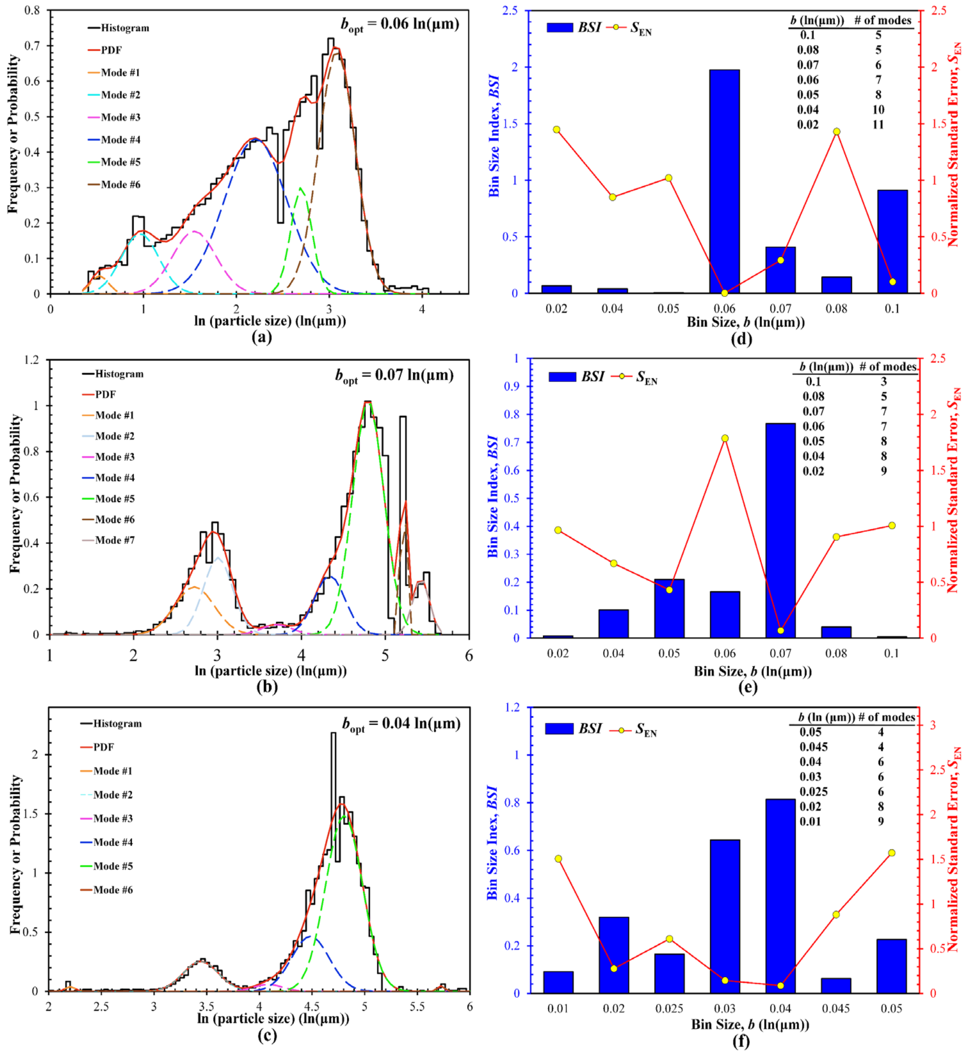

b (ln(μm))	# of modes
0.1	5
0.08	5
0.07	6
0.06	7
0.05	8
0.04	10
0.02	11

b (ln(μm))	# of modes
0.1	3
0.08	5
0.07	7
0.06	7
0.05	8
0.04	8
0.02	9

b (ln (μm))	# of modes
0.05	4
0.045	4
0.04	6
0.03	6
0.025	6
0.02	8
0.01	9

Figure 3.8 Deconvolution results for the PSDs of three focculated illite suspensions: (a) to (c): Histogram constructed at the b_{opt} and pertinent deconvoluted PDF distribution for pH = 8.61, 5.51, and 2.25 illite suspensions, respectively; (d) to (f): the relationships between the BSI and bin size and between the normalized standard error S_{EN} and bin size for pH = 8.61, 5.51, and 2.25 illite suspensions, respectively; The global BSI maximum is used to select the b_{opt}. Inset tables summarize the number of modes determined by deconvolution for each trial bin size.

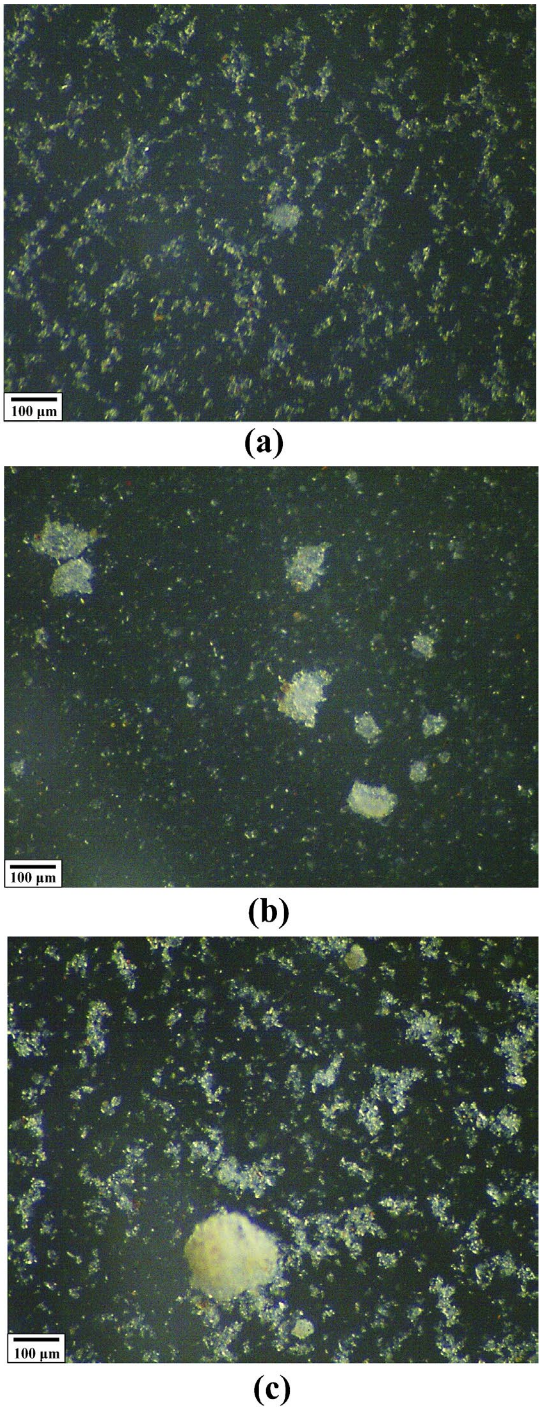

Figure 3.9 Example optical images of the flocculated illite suspensions prepared at a 35 ppt NaCl salinity:(a): pH 8.61; (b): pH 4.51; (c): pH 2.25.

Table 3.4 Summary of the fractions of different particle size groups in flocculated illite suspensions determined by the statistical deconvolution (note that the sum of fractions for ass particle size groups is 1.00)

Particle group	Size range (μm)	Population fraction, *A* (%)		
		pH = 8.61	pH = 4.51	pH = 2.25
Primary particles	< 10	57.37	/	0.45
Flocculi	10 – 30	42.63	26.62	/
Microflocs	30 – 200	/	13.56	33.66
Macroflocs	> 200	/	59.82	65.89

As a typical weathering product of K- and Al-rich sedimentary rocks (e.g., shales), illites are formed by the alteration of muscovite and feldspar under high pH conditions during which highly complex nanoscale irregularities, high crystal defect, and broken bond can develop on the face and edge surfaces of illites (Pevear 1999). These structural features render illite a very high net negative layer charge (e.g., typically -1.68 per $O_{20}(OH)_4$) and alkaline properties when dispersed in water, resulting in strong electrostatic repulsion between the face surfaces of individual particles caused by the repulsive double layer, which is further increased due to the pH-dependent negative charge that can also form electrical double layers on the edge surface (Tombácz and Szekeres 2004), and hence stabilization of the clay suspension is achieved by preventing particles from flocculation or aggregation. Increasing the ionic strength by adding different electrolytes (e.g., 35 ppt NaCl salinity selected in this study) and decreasing the pH by adding HCl can both promote flocculation among illite particles and flocs, leading to the formation of larger-sized microflocs and macroflocs, via reducing the repulsive double layer thickness and reversing the negative edge charges into positive ones when the adjusted pH is smaller than the point of zero charge of the illite, respectively, which can both increase the prevailing attractive forces (e.g., Coulomb attraction) over the double layer repulsions (which is also known as DLVO theory) (Derjaguin and Landau 1993; Verwey and J. T. G. Overbeek 1955).

3.5 Discussion

The above analyses of the synthetic datasets as well as real materials characterization datasets on the elasticity of three rocks and PSDs of flocculated clay suspensions validate the accuracy and effectiveness of the newly developed BSI method and its applicability to common data processing practices, especially for those involving multimodal datasets. Prior to further discussion, it is worth summarizing the basic concepts and underlying algorithms of this new statistical data binning criterion. A prior common binning criterion, the Freedman-Diaconis rule (Freedman and Diaconis 1981), in general sets the upper bound b_0 for the optimal bin size, but fails to provide a comparative feedback to assess the errors of the deconvolution or fitting of the histogram constructed by this b_0. In contrast, the BSI method employs a simple comparative, feedback algorithm to select the b_{opt} that basically results in the smallest S_{EN}, which is further penalized by the number of modes K (i.e., the errors are also dependent upon both the b and K), finally leading to the determination of the maximum BSI. In particular, the standard error S_{E} obtained at each tribal bin size b is not treated independently, but weighted and normalized by the mean μ_{S} and SD σ_{S} of all S_{E} values from all trial bin sizes via the S_{EN}. Different from previous methods and theories that select a bin size by mainly considering the fitting error resulting from only one selected bin size, the BSI method offers a quantitative estimate that delineates the boundary (i.e., the b_{opt}) between the overfitting with a too small bin size and the underfitting with a too big bin size (i.e., lower precision to the estimation of true statistical distributions).

Such an algorithm is generally similar to the *AIC* (Eq. (3.12)) and *BIC* (Eq. (3.13)) criteria in which the number of unknow parameters, $k = 3K - 1$, is used to balance or penalize the maximum likelihood value $\hat{L}$. Given this theoretical basis, the number of modes or phases used in the PDF-based deconvolution generally varies with the bin size: while a smaller number of modes is usually needed for a larger bin size, more modes are necessary for a smaller bin size to capture more details of the true distribution, and the random (or same) number of modes tend to be selected depending upon the generated S_E at a given trial bin size. As such, concerns with the correct number of modes selected to determine the smallest S_E may arise, since an infinite number of modes can be found at any bin size in the deconvolution constrained by only one limited compatibility condition (i.e., Eq. (3.2), the sum of the fractions of all individual modes should equal to 1.0) (Wu et al. 2020; Zhang et al. 2013b). This issue, admittedly, reflects the disadvantages of other conventional deconvolution methods (including both PDF and CDF-based methods), which not only require the number of modes as the input parameter for the fitting, but also an accurate estimation of initial values of the three statistical parameters (i.e., mean, SD, and fraction) of all different possible modes. This is particularly important for the gradient descent method that is commonly used for deconvolution to optimize the objective function. Despite the limitation, the validation based on the analyses of synthetic datasets with a constant number of modes still yields an interesting finding. When the number of modes is known and fixed during the deconvolution, the errors in the deconvoluted mean shows a stronger dependence on the bin size than the counterparts of the other two parameters, SD and fraction. This phenomenon can at least serve as a feasible rule for the prediction of errors in the mean of each deconvoluted mode when the same number of mode *K* is sometimes selected for different trial bin sizes (e.g., prediction of Young's modulus in the statistical nanoindentation). That is, for a given multimodal dataset, if the mode *K* is fixed, the error in the means of all *K* modes increase with the bin size.

Furthermore, it is interesting to compare and benchmark the accuracy and rationale of the BSI method with a widely used counterpart, the square root method, a built-in function of Microsoft Excel (Microsoft Office, USA) for bin size estimation (b_{Excel}) in most routine work:

$$b_{Excel} = \frac{Max(data) - Min(data)}{\sqrt{n}} \tag{3.18}$$

This method is used to repeat the deconvolution of some selected datasets discussed above, and results are summarized in Figure 3.10. It should be noted that, since the $\mathrm{b_{Excel}}$ values for the shale and flocculated illite suspension at pH 2.25 are greater than those estimated by the Freedman-Diaconis rule (Freedman & Diaconis, 1981), which serve as the upper bound, deconvoluted results are not compared for these two datasets. For the two synthetic datasets I and IV (Figures 10a and 10b), the two $\mathrm{b_{Excel}}$ values are both much smaller than the b_{opt} (i.e., for Dataset I, $b_{\mathrm{opt}} = 3.5$, $b_{\mathrm{Excel}} = 2.092$; for Dataset IV, $b_{\mathrm{opt}} = 4 - 4.5$, $b_{\mathrm{Excel}} = 2.470$), most likely due to the too large *n* values (Table 3.1). Furthermore, the two $\mathrm{b_{Excel}}$ values result in the wrong number of modes, i.e., $K = 6$ (versus the correct 3) and 7 (versus the correct 5) for Datasets I and IV, respectively, showing that the b_{Excel} cannot find the correct number of modes and hence other three parameters. For the four real measurement datasets (Figures 3.10c to 10f), the b_{Excel} is sometimes smaller than b_{opt}, but could also be greater than b_{opt}. Nevertheless, the corresponding BSI determined by each respective b_{Excel} is not the highest or global maximum, validating that the b_{Excel} cannot yield the smallest SEN or the highest BSI. Interestingly, in Figure 3.10f, a small variation in the b (i.e., $b_{\mathrm{opt}} = 0.07$ versus $b_{\mathrm{Excel}} = 0.07123$) can result in remarkable difference in the BSI, which further indicates that deconvolution should be performed via a trial-and-error algorithm to find the best b_{opt}, or the selection of b_{opt} should not rely on an unidirectional estimation, but more on the feedback of overall normalized errors. In summary, the results from all these b_{Excel} values further validate the accuracy and effectiveness of the BSI method in selecting the b_{opt} corresponding to the highest BSI for PDF-based statistical deconvolution of multimodal datasets. In addition, as pointed out earlier, the b_0 determined by the Freedman-Diaconis rule is usually greater than the b_{opt} determined by the BSI method.

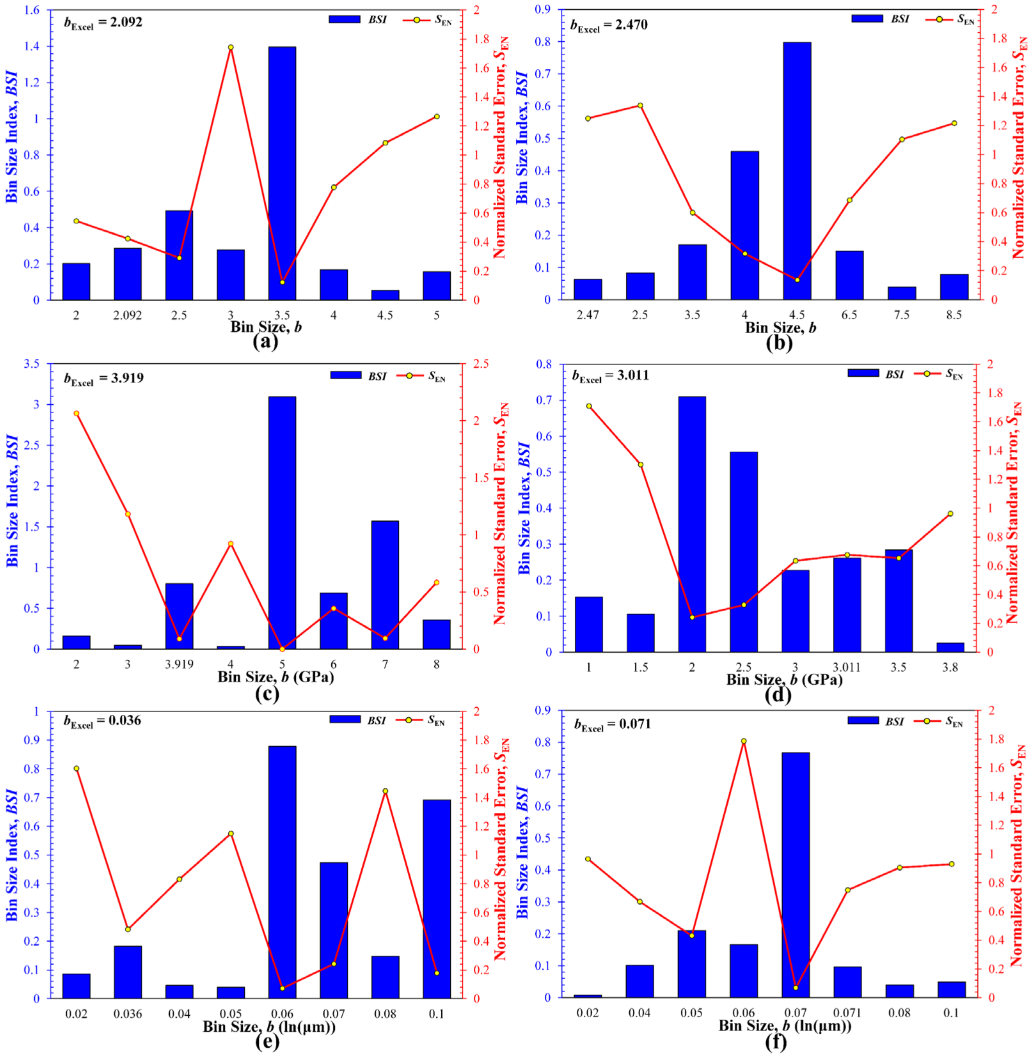

Figure 3.10 Comparison of the BSI and S_{EN} for different bin sizes, including the one determined by the Microsfot Excel program: (a): Synthetic Dataset I; (b): Synthetic Dataset IV; (c): KS-45; (d): KS-52; (e) illite suspension at pH 8.61; (f) illite suspension at pH 4.51.

Finally, as binning is widely used to smooth data or to handle noisy data, or even more generally in data mining (i.e., used as a data pre-processing method to minimize the effects of minor observation errors), the newly proposed BSI method may not only find ample applications to statistical deconvolution of multimodal datasets, but also be expected to play an important role in more generalized data mining and processing practices. For multimodal variates or datasets, an improperly selected bin size usually leads to a wrong number of modes, and hence the deconvoluted results may be misleading. The extension of the BSI method to two or three-dimensional multivariate datasets warrants further effort.

3.6 Conclusions

This paper presents a new bin size index (BSI) method, developed based on the residual normalized standard error penalized by the number of modes, for binning multimodal datasets from materials characterization. A total of 10 datasets, consisting of 4 normally-distributed synthetic ones, 3 normally-distributed ones on the elasticity of three rocks obtained by statistical nanoindentation, and 3 lognormally-distributed ones on the particle size distributions (PSD) of flocculated illite suspensions, were used to illustrate the BSI method's concepts and algorithms and demonstrate its accuracy and effectiveness. Based on the above analyses and discussion, the main conclusions can be drawn as follows:

- The accuracy and effectiveness of the BSI method were validated by the synthetic datasets with the pre-assigned number, mean, SD, and fraction of all modes, while the applicability to practical materials characterization demonstrated by the real measurement datasets on the elasticity of multiphase sedimentary rocks and PSDs of flocculated illite suspensions.
- In the plot of the BSI against trial bin size, the global maximum BSI corresponds to the optimal bin size, which can then be used to construct the

appropriate experimental histogram required for the PDF-based statistical deconvolution of multimodal datasets;

- The BSI method is demonstrated to be powerful and effective in binning the datasets obeying both normal and lognormal distributions, and is expected to be applicable to other types of statistical distributions;
- For all studied example datasets, the maximum BSI basically corresponds to the smallest normalized residual standard error, but with additional penalization by the number of deconvoluted modes;
- When the number of modes is fixed, the deconvoluted means, but not the SDs and fractions, show a more pronounced dependence on the bin size;
- The optimal bin size determined by the BSI method is not significantly affected by the total number of data entries in the dataset, nor by the maximum, minimum, or range of the data values. Instead, a feedback algorithm is used to compare all fitting errors from multiple trial bin sizes, while other conventional binning methods rely heavily on the number of data entries or range of data values and fail to feedback and assess the fitting errors.
- The bin size plays a more dictated role than the number of modes, since the latter is weakly correlated to, but not totally independent on, the former. Other parameters such as the mean, SD, and fraction of each mode can be determined by the trials of different initial values.

Acknowledgments

This work was partially supported by the US National Science Foundation (NSF) through Award CMMI-1702881. The first author, Tao Jiang, also received the Charles F. Perrell Fellowship from the Department of Civil and Environmental Engineering at the University of Massachusetts Amherst. The first author also acknowledges the valuable discussion and help from Dr. Yongkang Wu. Any opinions, findings, and conclusions expressed in this paper are those of the authors and do not necessarily reflect the views of the NSF.

CHAPTER 4

KINETICS OF FLOCCULATED ILLITE SUSPENSIONS AFFECTED BY IONIC STRENGTH, PH, AND HYDRODYNAMIC SHEARING[2]

An experimental investigation is presented of the kinetics of particle size distributions (PSDs) of flocculated illite suspensions subject to varying ionic strength, pH, and hydrodynamic shearing. A total of 21 PSD measurements were conducted by analyzing the high-resolution optical images of particle flocs extracted from illite suspensions with a concentration of 0.4 g/L prepared at four ionic strengths (i.e., 0, 0.09, 0.17, 0.60 M NaCl solution), three pHs (i.e., 8.61, 4.51, 2.25), and three vibrational shaking speeds (i.e., 150, 225, 300 oscillation/min) at four shaking durations (i.e., 10, 30, 60, 1440 min). Experimental PSD histograms were constructed using a new bin size index (BSI) data binning method involving the conversion of original multimodal lognormal distributions into regular Gaussian distributions, followed by the probability density function (PDF)-based deconvolution to extract the number, mean, standard deviation, and fraction of different characteristic particle size groups: primary particles, flocculi, microflocs, and macroflocs. Results show that flocculation is enhanced by the high ionic strength and low pH, and more microflocs and macroflocs form at higher ionic strengths (i.e., 0.60 M) and more acidic pHs (i.e., 2.25, 4.51). Moreover, higher hydrodynamic shearing causes more breakdown of weaker flocs, but promotes stronger and smaller ones. The new BSI data binning method can better reveal the smaller-sized particle groups due to the logarithmic conversion. The PSD kinetics of illite suspensions is chiefly controlled by the face-to-face

---

[2] This chapter has been published as a standalone paper: Jiang, T., Wu, Y., Liu, C., Whittle, A., Guo, D., Zhang., G. (2022). Kinetics of flocculated illite suspensions affected by ionic strength, pH, and hydrodynamic shearing. *Applied Clay Science, 221*(7), 106462

and edge-to-face interparticle interactions, caused by the suppression of the electrical double layer and generation of positive edge charges, respectively. Finally, the implications and significance of PSD kinetics of clay suspensions for engineering practices and environmental processes are discussed.

4.1 Introduction

As a naturally occurring, ubiquitous geomaterial, clay minerals are characterized by their peculiar structural and physiochemical properties resulting from geochemical processes such as weathering, transformation, and crystallization. For instance, clay minerals usually have very small particle sizes (e.g., < 2 μm), high specific surface areas (SSA), nano-layered structures (e.g., 0.7 and 1.0 nm thick 1:1 and 2:1 layers, respectively), and negative layer charges induced by isomorphous substitutions (e.g., Al3+ for Si4+ and Mg2+ for Al3+ in the tetrahedra and octahedral sheets, respectively). These features then promote clay minerals' active participation in many environmental processes, such as extensive interactions with other suspended matter (e.g., exopolymers, microorganisms) found in various natural waters (e.g., rivers, estuaries, and oceans) via intermolecular and surface forces (e.g., van der Waals attractions, Coulomb forces, hydrogen bond, ion-dipole forces), leading to the formation of larger, porous cohesive particulate aggregates or flocs of ~ 10 to 500 μm in size (Furukawa et al. 2009, 2014; Harris and Mitchell 1973; Maggi 2005). In prior research focusing on flocculation of clay minerals, much attention was paid to the particle size distributions (PSDs) of clay suspensions, and those works played a fundamental and indispensable role in providing reference data for many scenarios involving the flocculation of clay minerals (Bergaya and Lagaly 2006; Harvey and Murray 1997; Murray 2000; Walling and Moorehead 1989; Wu 2001). Essentially, flocculation of clay minerals can be considered as a highly dynamic process where the PSDs of suspended solids vary significantly due to the formation of diverse-sized flocs, and hence have important influences on the natural aquatic environments (e.g., sediment settling and transport, turbidity).

The PSDs of clay mineral suspensions during sediment transport, in general, vary with time, as a result of response to various environmental stimuli, such as ionic strength, pH, and hydrodynamic shearing. The first factor accounting for the chemical effects is the ionic strength or salinity of the aquatic environments, typically including dissolved inorganic salts, polyelectrolytes with ionizable groups, and bio-flocculants (Shaikh et al. 2017; Tiraferri and Borkovec 2015). Similar to other colloidal particles dispersed in liquids (i.e., sol-like materials), particle-to-particle interactions are responsible for the stability and evolution of clay mineral dispersions or suspensions. Generally, the formation of clay flocs, or destabilization of a clay dispersion, results from the prevailing attractive forces between particles over the repulsive counterparts (Richtering 2019). In fact, most clay minerals possess permanently net negative layer charges, resulting in the formation of electrical double layer (EDL) on their surfaces that generates a long-range repulsion impeding the flocculation of clay particles (Mitchell and Soga 2005). Such repulsive forces can be mitigated or even eliminated by adding various coagulants or flocculants to the suspension, which facilitate the attraction between clay particles and hence the formation of larger-sized clay flocs, by either suppressing the EDL with multivalent ions (e.g., Al3+, Fe3+) and increased salinity, or intermolecular interactions (e.g., adsorption, crosslinking) with added exopolymers (e.g., xanthan) or polyelectrolytes with ionic functional groups actively interacting with the clay surfaces via H-bonding and Coulomb forces (Brigatti et al. 2006, 2013; Sincero and Sincero 2002; Young et al. 1994).

The second environmental stimulus that affects clay particle interactions and hence flocculation and PSDs is the pH or acidity. The edge surface of clay minerals is composed of broken bonds that hydrolyze to form Si-OH or Al-OH (Yariv and Cross, 1979), resulting in variable, pH-dependent charges, which exhibit amphoteric properties by protonation (i.e., adsorption of H+) or deprotonation (i.e., loss of H+) reactions depending upon the pH of aquatic environments (Delhorme et al. 2010). As such, decreasing the pH can result in a positively-charged edge surface and hence flocculation of clay minerals because of the attraction between the dissimilarly-charged edge and face surfaces (Gu and Evans 2008; Konduri and Fatehi 2017; Mietta et al. 2009). Quantitatively, such effects of pH on clay flocculation are related to the concept of point of zero charge (PZC), defined as the pH at which the total net surface charge is zero or the permanent negative charges on the face surface are exactly counterbalanced by the positive ones on edge surface. However, more recently, the concept of PZC of local edge surface (i.e., PZCedge) only was also defined to describe the pH at which the edge surface reverses the pH-dependent charges (i.e., from positive to negative or vice versa) (Sposito et al. 1999; Tombácz and Szekeres 2004). Globally, two clay particles with the same net charge polarity may not approach each other to flocculate due to the EDL repulsion. On the other hand, locally, these two particles may still flocculate, under certain conditions such as flow-induced shearing (as discussed later), via the attraction between the positively charged edge and negatively charged face, even if their overall net charges are all negative. Nevertheless, both concepts, PZC and PZCedge, of clay minerals may be used in assessing suspension stability and flocculation of clay minerals with amphoteric surface sites (e.g., the edge of clay minerals, alumina, and silica surfaces). Moreover, due to the dissimilar acid-base properties and different fractions of the Si-OH and Al-OH sites exposed on clay mineral's edge surfaces (Tombácz and Szekeres 2004), the PZCedge of most clay minerals is not pH 7. For instance, the surfaces of alumina and silica are all amphoteric and have a PZC of pH

~8.1 and 4.8, respectively, while the Na-montmorillonite (SWy-1) has a PZCedge of pH ~6.5, at which only the amphoteric Al-OH sites develop a positive charge, and such behavior is affected by the ionic strength of the aqueous solution (Janek and Lagaly 2001). As such, the effect of pH on flocculation of clay particles is quite complex: the types and locations of edge charges and background ionic strength both affect the PZCedge of clay minerals.

Furthermore, in the natural aquatic environments where hydrodynamic flow conditions are drastically dynamic, the evolution of PSDs of clay mineral suspensions is also significantly influenced by water flow and associated hydrodynamic shearing that directly drives clay particles to interact with each other as well as other solids (e.g., organic matter) (Mietta et al. 2009) and may also breakdown relatively weaker flocs. Some quantitative indices are used in the literature to account for the hydrodynamic flow conditions, such as the Reynolds number (Re) and shear rate (G). In fact, three types of flow can be categorized, including laminar flow if Re < 2000 or G ~ 10 s-1, transitional flow if 2000 < Re < 4000 or G ~ 350 s-1, and turbulent flow if Re > 4000 or G ~ 900 s-1. These flow conditions correspond to maximum shear stress (τ) ranging from 0.02 to 1.10 Pa (Matsuo and Unno 1981). Generally, during the resuspension, transport, and settling process, the formation of flocs is primarily governed by two competitive processes: floc growth and formation versus breakdown. If the shear strength of a newly formed floc is greater than the hydrodynamic shear stress, then larger-sized flocs are expected to form in subsequent particle collision and flocculation. On the contrary, floc breakage occurs if the hydrodynamic shear stress exceeds the strength of the floc, thus causing a reduction in floc size (Jarvis et al. 2005a). Following this principle, many studies were conducted to investigate the flocculation of clay minerals under varying flow conditions, such as the types of flow or different shear rates, shearing durations, number of shearing cycles, inherited floc sizes (i.e., the size of flocs that formed under a certain shear rate), and floc aging time (i.e., the length of time for flocs remaining on the bottom bed after settling) (He et al. 2012; Keyvani and Strom 2014; Kuprenas et al. 2018; Owen et al. 2008; Spicer and Pratsinis 1996; Tran and Strom 2019; Yu et al. 2011).

In summary, flocculation of suspended clay minerals and other cohesive sediments is inherently complex, owing to the intensive particle-to-particle interactions induced by their physicochemically active surfaces, which can be further complicated by the variable environmental factors such as pH, ionic strength, and hydrodynamic shearing. Prior studies considering the effects of these specific factors on clay flocculation were conducted on some clay minerals that are both abundant in natural environments and representative of major clay species, such as kaolinite, Na-montmorillonite, and Ca-montmorillonite (Tan et al. 2014b). While kaolinite is a 1:1 type clay mineral without expandable or swelling layers, Na- and Ca-montmorillonites are 2:1 type swelling clays with Na+ and Ca2+ as the major interlayer exchangeable cations. However, specific work on the flocculation of illite is seldomly reported in the literature. This paper focuses on the flocculation and PSD kinetics of illite, using a source clay mineral, IMt-1, as the model material. Illite is a 2:1 type non-swelling clay mineral whose physicochemical properties are reportedly intermediate between kaolinite and smectite. For example, the particle size and specific surface area of illite are usually less than those of swelling smectite, but greater than the counterparts of kaolinite. The primary objective of this study was to investigate the PSD variations of flocculated illite suspensions prepared under three environmental conditions: (1) different ionic strengths adjusted by an indifferent monovalent salt, sodium chloride (NaCl), (2) different pH adjusted by the titration of hydrochloric acid (HCl) solution, and (3) variable hydrodynamic shearing forces achieved by different vibrational shaking speeds and durations. The results and findings are expectedly of significant importance to the industrial applications and environmental processes involving suspended cohesive sediments and intensive clay-water-salt interactions.

4.2 Materials and methods

4.2.1 Clay minerals

The highly pure illite (IMt-1) from the U.S. Clay Minerals Society (CMS) Source Clay Repository, was studied as the model clay. It was widely used as a reference clay mineral by many prior studies. Apart from some representative properties of most phyllosilicates, such as layer charges, illite is also featured with the nonhydrated K^+ as interlayer cations, similar to the mica group minerals (e.g., muscovite, glauconite, and biotite), and its layers are non-expandable upon wetting. The basic structural and chemical properties of IMt-1 together with two other reference clay minerals, Na-smectite (SWy-2) and kaolinite (KGa-1b), are summarized in Table 4.1. While the Na-smectite is a swelling mineral that can exfoliate into very thin individual 2:1 layers upon free swelling, the kaolinite is a 1:1 type mineral with a relatively bulky geometry. The as-received IMt-1 sample consisted of small rock chips, which were first manually ground with a mortar and pestle and then wet ground with ethanol in a McCrone micronizing mill (McCrone Accessories & Components, Wetmont, IL, USA) for 3 mins, followed by overnight oven-drying at 110°C. Finally, a fine illite powder was obtained by sieving the oven-dried powder through a No. 635 mesh with an opening size of 20 μm in a mechanical shaker designed for sieving analysis. The SWy-2 and KGa-1b were supplied as dry powders and hence were directly used without further processing.

Table 4.1 Basic structural and physicochemical properties of the three studied minerals (excepted noted, all data are taken from the U.S. Clay Minerals Society Source Clay Data Sheets.

Name	CEC[a]	SSA[b]	pH[c]	Layer charge[d]	Chemical formula
Illite (IMt-1)	15.00[e]	30.00[f] or 24.90[g]	8.61	-1.68	$(Mg_{0.09}Ca_{0.06}K_{1.37})$ $[Al_{2.69}Fe^{3+}_{0.76}Fe^{2+}_{0.06}Mn_{tr}Mg_{0.4}Ti_{0.06}]$ $[Si_{6.77}Al_{1.23}]O_{20}(OH)_4$
Kaolinite (KGa-1b)	2.00	10.05	5.97	-0.06	$(Mg_{0.02}Ca_{0.01}Na_{0.01}K_{0.01})$ $[Al_{3.86}Fe^{3+}_{0.02}Mn_{tr}Ti_{0.11}]$ $[Si_{3.83}Al_{0.17}]O_{10}(OH)_8$
Na-smectite (SWy-2)	76.40	31.82	6.44	-0.55	$(Ca_{0.12}Na_{0.32}K_{0.05})$ $[Al_{3.01}Fe^{3+}_{0.41}Mn_{0.01}Mg_{0.54}Ti_{0.02}]$ $[Si_{7.98}Al_{0.02}]O_{20}(OH)_4$

[a] CEC: cation exchange capacity.

[b] SSA: specific surface area.

[c] pH of the clay suspension at a concentration of 0.4 g/L in de-ionized water at room temperature (23°C).

[d] Layer charge of each mineral is calculated based on per $O_5(OH)_4$ for KGa-1b or per $O_{10}(OH)_2$ for IMt-1 and SWy-2.

[e] Data from Kinter and Diamond (1956) and Hower and Mowatt (1966).

[f] Data from Celis and Koskinen (1999).

[g] Data from Goldberg et al (1996).

4.2.2 Preparation of illite suspensions

The concept of intrinsic PSD (Zhang et al. 2004b) mainly emphasizes the importance of complete dispersion of a clay sample to obtain the sizes of truly primary particles. For the studied illite, the presence of pre-existing clay aggregates or pulverized rock chips would affect the true PSD of illite particles and flocs, the latter of which formed via the interactions between the truly primary particles, affected by different environmental factors. Therefore, it was necessary to disaggregate and disperse those illite chips and aggregates prior to the true flocculation process. Tan *et al.* (2017) evaluated the effectiveness of chemical dispersants and mechanical energy to further disperse four US CMS source clay minerals, including IMt-1, and recommended that overnight soaking or using sodium hexametaphosphate ($(NaPO_3)_6$) as a dispersant be the optimal dispersion methods to obtain the intrinsic PSD of illite. However, given the possible hindering effects of the clay edge-adsorbed PO_3^- on flocculation (i.e., the fully solvated PO_3^- can increase the interparticle distance due to the relatively larger volume occupied by the hydrated PO_3^- anions), overnight soaking was selected as the dispersion method to obtain the fully dispersed illite suspensions consisting of primarily primary particles. Dry illite powder of 0.12 g was soaked in 10 mL deionized (DI) water in a centrifuge tube for >16 hours, followed by transferring the hydrated illite to a blender for further disaggregation and dispersion with 290 mL DI water for 5 mins at a high speed, which was traditionally used for hydrometer analysis. This resulted in an illite suspension with a concentration of 0.4 g/L for subsequent flocculation and PSD analyses.

4.2.3 Flocculation experiments

Besides the DI water, HCl solution with a concentration of 36.5 wt.% and NaCl solution at three salinities (i.e., 5, 10, and 35 ppt, equivalent to 0.09, 0.17, and 0.60 M ionic strengths, respectively) were used to adjust the pH and ionic strength of the clay suspensions at a constant illite concentration of 0.4 g/L. While the total volume of all clay suspensions remained the same at 300 mL, four different ionic strengths (i.e., 0, 0.09, 0.17, and 0.60 M NaCl) and three different pHs (i.e., 8.61 (the pH of pure clay suspension), 4.51, and 2.25) were prepared via adding the appropriate amount of NaCl or HCl solution to the suspension.

Flocculation was then conducted by subjecting the illite suspension stored in a round-bottom flask to a swing-mode vibration using a Burrell Model 95 wrist-action shaker (Burrell Scientific, Pittsburgh, PA, USA) with adjustable shaking speeds (i.e., in the range of 150 to 450 oscillation/min), shaking duration (i.e., timed to continuous shaking), and shaking angle (i.e., 0 to 15° arc angle of the flask-holding arm referenced to the horizontal direction). In general, flocculation of suspended particles commences once the vibrational shaking starts, and floc generation may experience an initial transient process and then reach a steady state at which the PSD is stable. During the prolonged continuous vibrational shaking, flocs formation and breakdown reached a balanced steady-state.

Based on extensive preliminary trials, a shaking speed of 150 oscillation/min, 24 h shaking duration, and 15° shaking angle were selected as the initial reference condition used for particle flocculation. Such a condition was likely to generate a hydrodynamic shearing stress comparable to that of laminar flows. In addition, two other shaking speeds, 250 and 300 oscillation/min, were also used to examine the effects of different hydrodynamic shearing stresses on particle flocculation, and three shorter shaking durations, 10, 30, and 60 mins, to investigate the transient flocculation and PSD kinetics. In summary, nine suspensions, all with 0.60 M ionic strength and 8.61 pH, were studied to examine the different hydrodynamic shearing (i.e., 3 shaking speeds and 3 shaking durations); four suspensions to investigate the different ionic strengths (i.e., 0, 0.09, 0.16, and 0.60 M NaCl solution); eight suspensions to study the combined effects of both ionic strength (i.e., 0, 0.09, 0.17, and 0.60 M NaCl solution) and pH (i.e., 4.51 and 2.25) (Table 4.2). Overall, a total of 21 suspensions were prepared for PSD measurements and analyses.

Table 4.2 Summary of environmental variables examined in this study.

Environmental factor	Ionic strength (M)	pH	Shaking speed (oscillation/min)	Shaking duration (min)
Salinity	0, 0.09, 0.17, 0.60	8.61	150	1440
Salinity & acidity	0, 0.09, 0.17, 0.60	4.51, 2.25	150	1440
Hydrodynamic shearing	0.60	8.61	150, 225, 300	10, 30, 60

Upon the completion of each flocculation experiment, a pipette was immediately used to extract a large volume of suspension that was manually shaken to prevent particle settling. The aliquot of suspension was then dispensed onto ten sterile Petri dishes for imaging. For each Petridish, upon the completion of settling of particles to the bottom (e.g., usually overnight to 24 h), multiple images were captured using an optical microscope that was built in the FemtoTools FT-UMS1002 universal measurement system (Nanoscience Instruments, Inc., Phoenix, AZ, USA) to ensure the statistical accuracy of the measurements. For each PSD measurement, a total of 15 to 20 optical images were acquired for subsequent image analysis, resulting in a large number (e.g., >5,000) of analyzed particles.

4.2.4 Image analyses

ImageJ, a free, open-source, Java-based image analysis program developed by U.S. National Institutes of Health, was employed to measure the particle sizes of illite flocs by following the protocols established by prior studies (Keyvani and Strom 2013; Mazzoli and Moriconi 2014; Tajima and Kato 2011). Basically, five key steps were involved: (1) conversion of original color images to the 8-bit grayscale ones; (2) subtraction of uneven background light; (3) contrasting and segmentation to differentiate particles' border; (4) thresholding to produce a binary image with black colored particles and white-colored background; (5) measurement of particle sizes by running the built-in "Analyze Particles" function. Appendix presents the details of these steps using an example image.

An equivalent circular diameter, d_s, was selected to represent the sizes of the irregularly-shaped individual particles and flocs, which can be calculated by the following equation:

$$d_s = \sqrt{\frac{4A}{\pi}} \tag{4.1}$$

where A is the projected area of the particle, which was measured using ImageJ. A stage micrometer with a resolution of 0.001 mm was used to calibrate the size of each pixel of the acquired optical images. The experimental particle size d_s data measured by ImageJ was then exported for statistical deconvolution analysis.

4.2.5 Statistical deconvolution

Prior studies (Lee et al. 2012; Lee and Kim 2018; Mikkelsen et al. 2006; Zhang et al. 2013b) demonstrated that suspended cohesive sediments with clay minerals as the main solid constituents exhibit a multimodal lognormal distribution of PSDs where each subordinate unimodal lognormal PSD represents a particular size-discrete particle group. To quantitatively analyze each particle group, statistical deconvolution was performed on the experimental PSD data. Because of the essentially high skewness of lognormal distribution that can lead to the concentration of data points and thus possible overcrowded or hidden particle groups, especially at smaller size ranges, the experimental size data were transformed to their logarithmic values, generating new normally-distributed PSDs. That is, if a discrete random dataset X obeys a lognormal distribution with μ and σ as mean and standard deviation, then the transformed counterpart $ln(X)$ should be a normally distributed random dataset (Johnson et al. 2005).

Statistical deconvolution of the lognormally transformed experimental PSD data was then performed by fitting the experimental histogram with a certain number K of unimodal normal distributions f_j expressed by the following equation:

$$f_j(x;\mu_j;\sigma_j) = \frac{1}{\sigma_j\sqrt{2\pi}} e^{-\frac{(x-\mu_j)^2}{2\sigma_j^2}} \tag{4.2}$$

where μ_j and σ_j are the mean and standard deviation of the j-th particle group and $j = 1, 2, 3, \ldots, K$. Each size-discrete particle group had a population-based fraction, A_j, which is subjected to a compatibility condition:

$$\sum_{i=1}^{K} A_i = 1 \tag{4.3}$$

where K is the total number of particle groups in a suspension.

Particularly, in the construction of experimental histogram, the selection of a proper and rational bin size (or bin width) plays a vital role in determining the deconvolution results: larger bin sizes help generalize the distribution due to the less induced measurement randomness, while a higher precision of fitting the experimental histogram can be obtained with the smaller bin sizes. In this study, a recently developed data binning criterion, termed as Bin Size Index (BSI) method, was employed to determine the optimal bin size for the construction of experimental PSD histograms. Example results of the probability density function (PDF)-based deconvolution by employing the BSI method can be found in Chapter 3.

4.3 Results and discussion

4.3.1 Optical imaging

Figure 4.1 shows example optical images of illite flocs randomly taken from different flocculation conditions. A general pattern of PSD of flocs can be visually recognized: flocs have non-uniform sizes of ~1 and ~700 μm, depending upon the ionic strength and pH of the clay suspensions. At the same pH, the size of relatively larger ones increases with the ionic strength, at least for the studied NaCl salinities of 0 to 0.60 M. On the other hand, at the same ionic strength, flocs of > ~100 μm in size present at pH 4.51 and 2.25, while only smaller flocs of ~10 μm exist at pH 8.61, the initial pH of the illite suspension prepared with DI water. Also, flocs with dense stacking, manifested by the relatively dark color, tend to form at higher ionic strengths (i.e., 0.17 and 0.60 M NaCl concentration), whereas irregularly-shaped thin flakes are widely present in the suspensions of 0 and 0.09 M ionic strengths. Apparently, the ionic strength and pH are two key environmental factors responsible for the variation of floc size and morphology. A general explanation is that an increase in ionic strength results in the formation of denser flocs with face-to-face associated flocs due to the suppressed electrical double layer (EDL), which is to be discussed further later, while an acid pH can reverse the edge charge to be positive and hence facilitate edge-to-face flocculation or the formation of larger-sized (>100 μm) flocs.

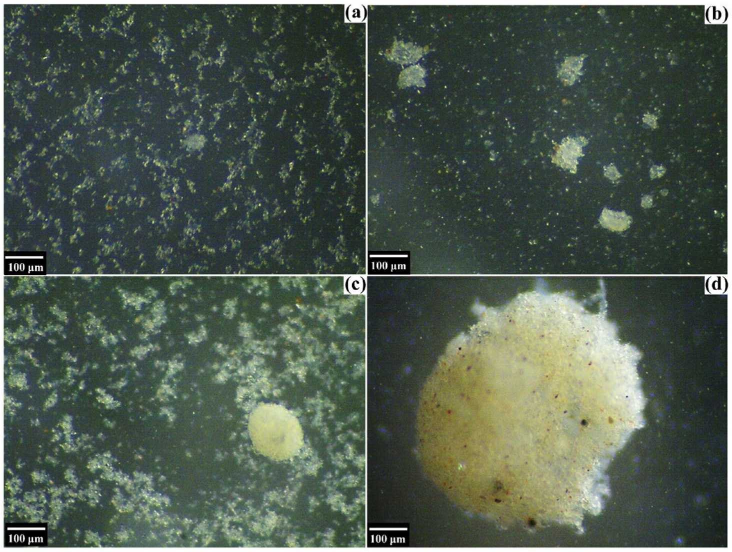

Figure 4.1 Selected images of illite particles and flocs prepared under different environmental conditions: (a) ionic strength: 0 M, pH: 8.61; (b) ionic strength: 0.17 M, pH: 4.51; (c) ionic strength: 0.60 M, pH: 4.51; (d) ionic strength: 0.60 M, pH: 2.25

To further validate the above observation and interpretation, the same flocculation experiments were also performed on the KGa-1b and SWy-2 samples (Table 4.1) at 0 and 0.60 M NaCl ionic strengths and no pH adjustment (i.e., the suspension's original pH). As shown in Figure 4.2, for both ionic strengths, flocs of >100 μm in size can form in kaolinite suspensions and their population increases with ionic strength. However, for SWy-1, only smaller flocs exist at 0 ionic strength, while flocs of >100 μm form at 0.60 M ionic strength. The difference in the flocculation behavior of the three clay minerals can be generally explained by their dissimilar electrochemical properties. The KGa-1b has the lowest layer charge and pH (5.97), followed by the SWy-2 with a layer charge of -0.55 and pH 6.44, while the IMt-1 has the highest layer charge (-1.68) and pH (8.61). The formation of large flocs in the 0 M kaolinite suspension indicates the positive effects of acidic pH and low layer charge on flocculation. Moreover, the PSD of the illite suspension prepared at pH 8.61, 0 M NaCl ionic strength, and 150 oscillation/min is compared with the counterpart reported by Tan et al. (2017) obtained by a laser diffraction-based particle size analyzer at the same conditions except a different device used to apply hydrodynamic shearing, and a consistent median particle size d_{50} (i.e., 7.39 vs. 6.37 μm) is obtained. This further validates the applicability of the imaging-based PSD measurement technique adopted in this study.

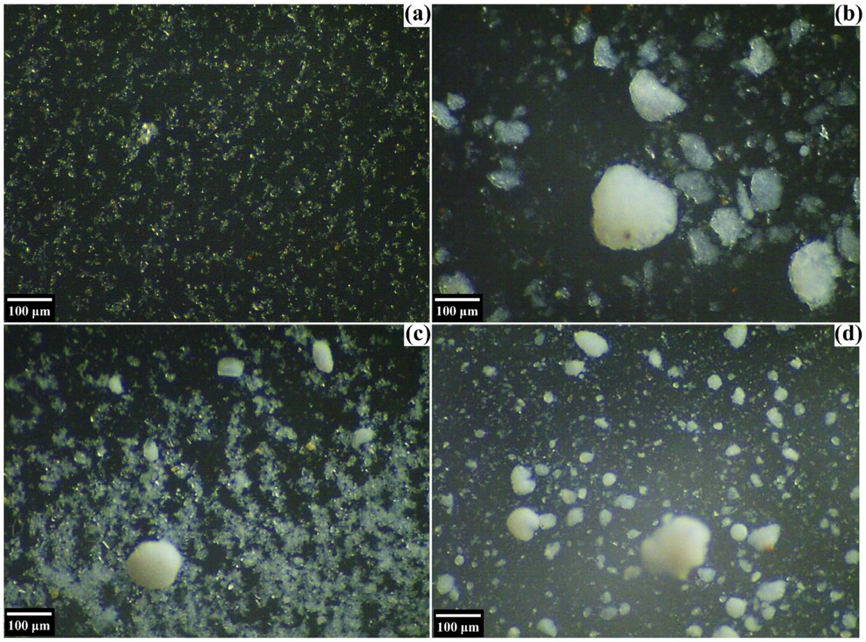

Figure 4.2 Selected images of Na-smectite and kaolinite particles and flocs prepared under different environmental conditions: (a) smectite, ionic strength: 0 M; (b) smectite, ionic strength: 0.60 M; (c) kaolinite, ionic strength: 0 M; (d) kaolinite, ionic strength: 0.60 M.

4.3.2 Effects of ionic strength

The influence of different ionic strengths via the four NaCl solutions on the flocculation and PSDs of illite suspensions is shown in Figure 4.3, which can also serve as the baseline data for the effects of pH to be discussed later. In general, the PSDs of all four suspensions show multimodal lognormal distributions with a size range of 1.42 to 58.6 μm. As the ionic strength increases, the PSD curves shift to the right, indicating the formation of a greater number of larger flocs. Although the peak of the largest flocs formed in 0.60 M NaCl moves toward left slightly, it is still the highest peak of all PSD curves. As stated earlier, the overall PSD curves for all ionic strengths were obtained by fitting the experimental histograms with multimodal lognormal Gaussian distributions, where each particle size group was represented by a unimodal lognormal PDF. Thus, the statistical parameters such as the mean and standard deviation of each particle group and its number-based fraction can be determined, leading to the analysis of PSD kinetics of illite suspensions at the four ionic strengths.

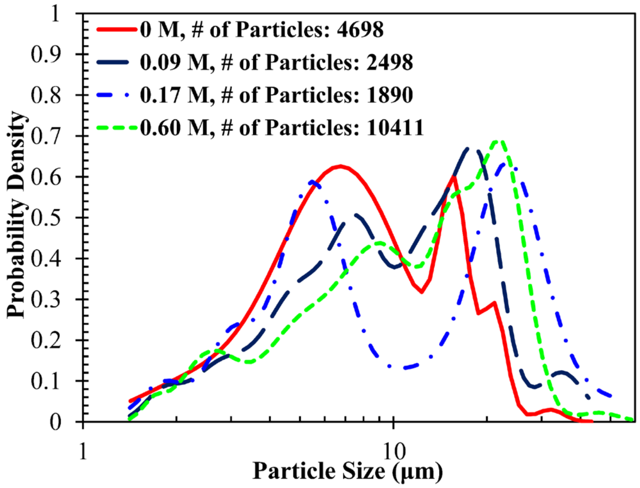

Figure 4.3 PSD curves of illite suspensions at four ionic strengths: 0, 0.09, 0.17, and 0.60 M NaCl.

Depending upon the different size ranges of all particles constituting a peak or a mode in the multimodal PSD curves, prior studies proposed a conceptual hierarchical size structure to categorize different particle groups for suspended particulate matters: single fractions or primary particles (i.e., including primary clay particles, organic matter, and living organisms/bacteria colonies), flocculi (i.e., defined as a group of clay particles strongly bonded via interfacial or interparticle forces), microflocs consisting of primary particles and flocculi, and larger-sized macroflocs that are built up from all aforementioned particle groups (e.g., usually on the order of > ~200 μm) (Lee et al. 2012; Zhang et al. 2013b). A similar criterion for categorizing different particle groups is used in this paper, which was based on the mean value of each deconvoluted mode (i.e., phase). As a result, a mode with a mean of 1 to 10 μm belongs to primary particles, while flocculi, microflocs, and macroflocs have their means at 10 to 30, 30 to 200, and > 200 μm, respectively. Based on this criterion, the two statistical parameters (i.e., mean and particle number-based fraction) for all deconvoluted particle groups are summarized in Table 4.3. As the ionic strength increases, the fraction of primary particles decreases, while the flocculi and microfloc groups account for a higher percentage in the suspension, indicating that those primary particles gradually flocculate and aggregate, forming relatively larger-sized flocculi and microflocs. Also, primary particles and flocculi can be regarded as the main particle groups in the illite-salt suspensions, as indicated by the relatively higher fractions of these two particle groups and the total number of deconvoluted phases (Table 4.3).

Table 4.3 Summary of fraction and mean particle size for each deconvoluted constituent in illite-salt suspensions

Ionic strength (M)	Deconvoluted mode #	Mean size (μm)	Fraction (% by number)	Particle size group
0	1	2.34	7.15	Primary particles
	2	7.57	74.43	
	3	15.75	12.47	Flocculi
	4	21.22	5.31	
	5	32.32	0.64	Microflocs
0.09	1	1.70	0.85	Primary particles
	2	2.64	8.91	
	3	4.83	10.07	
	4	9.64	37.65	
	5	15.74	12.28	Flocculi
	6	22.69	29.47	
	7	46.38	0.76	Microflocs
0.17	1	1.84	3.26	Primary particles
	2	3.05	9.21	
	3	5.62	35.60	
	4	12.13	8.61	Flocculi
	5	24.06	39.59	
	6	46.44	3.73	Microflocs
0.60	1	1.82	2.08	Primary particles
	2	2.87	7.83	
	3	5.03	17.67	
	4	7.74	20.10	
	5	13.70	27.70	Flocculi
	6	19.33	20.17	
	7	35.25	4.45	Microflocs

Much effort was made to study the effects of salinity or ionic strength on the PSDs of clay suspensions (Kang et al. 2019; Liu et al. 2015). One classical theory adopted to account for the effects of ionic strength is the Derjaguin-Landau-Verwey-Overbeek (DLVO) theory (Derjaguin and Landau 1941; Verwey and J. T. G. Overbeek 1955), which postulates that the stability of a colloidal dispersion such as clay suspensions is primarily dictated by the interactions between the charged clay particles, i.e., the net force between the van der Waals (vdW) attraction and EDL repulsion (Mitchell and Soga 2005). It was effectively demonstrated that increasing the ionic strength or electrolyte concentration can suppress the EDL thickness, and thus the repulsion between the charged clay particles is gradually weakened. In fact, the Debye length (κ^{-1}), the thickness of double layer, is given as follows (Goetz 2010):

$$\kappa^{-1} = \sqrt{\frac{\varepsilon_{\mathrm{r}}\varepsilon_0 k_B T}{2\times 10^3 N_A e^2 I}} \tag{4.4}$$

where I is the ionic strength in molarity, ε_0 the permittivity of vacuum (8.854 × 10^{-12} F/m), ε_{r} the relative permittivity or dielectric constant of the solvent, k_{B} the Boltzmann constant (1.381 × 10^{-23} J/K), T the absolute temperature, N_{A} the Avogadro's number (6.022 × 10^{23}), and e the elementary charge (1.602 × 10^{-19} C). In the present study, the dielectric constant is 80.4, 79.2, 77.9, and 71.8 for 0, 0.09, 0.17, and 0.60 M NaCl solution, respectively (Meissner and Wentz 2004). Hence, the EDL thickness is estimated as 1.76, 1.35, and 0.65 nm for 0.09, 0.17, and 0.60 M ionic strength, while the theory does not work for pure water or 0 ionic strength. Therefore, the decreased EDL thickness due to the increased ionic strength results in a closer arrangement of illite particles, which then promotes the vdW attraction. As such, flocculation due to face-to-face and face-to-edge association prevails in the suspensions of higher ionic strength, which can interpret the PSD variations of illite suspensions at the four ionic strengths (Table 4.3)

As an important electrochemical parameter to quantify the EDL repulsion and thus the stability of clay dispersions, the Debye length indirectly reflects the distance within which the electrostatic potential of a charged surface develops in an electrolyte solution. Within this range, some characteristic potentials, the zeta potential (ζ), Stern potential, and surface potential, form on the slipping plane, Stern plane, and surface of negatively charged clay particles, respectively, due to the difference in the electric potential relative to a point in the bulk solution away from the interface caused by specific electrokinetic movement of ions (e.g., fixed ions adsorbed onto the charged surface and free ions moving in the solution under the thermodynamic energy) (Goetz 2010; Kaszuba et al. 2010; Kollannur and Arnepalli 2019). Most prior studies used the zeta potential to characterize the aggregation and flocculation behavior of suspended clay particles since it explicitly defines the mobility of charged particles in an electrical field in which the charged particles interact through the compressive and tangential movements of the slipping/shear plane at which the zeta potential is defined. Advanced techniques such as the zeta meter are widely used to estimate the zeta potential of clay suspensions via the measurement of electrophoretic mobility of colloidal particles. The zeta potential ζ can then be determined with the Henry equation:

$$U_E = \frac{2\varepsilon\xi F(\kappa\alpha)}{3\eta} \tag{4.5}$$

where U_E is the measured electrophoretic mobility, ε the dielectric constant of the bulk solution, $F(\kappa\alpha)$ the Henry function, η the viscosity of suspensions (Kang et al. 2019; Lu et al. 2020; Mietta et al. 2009). Similarly, the other two electrostatic parameters, Stern and surface potentials, can also help unravel the electrokinetic structure of the EDL and thus facilitate the interpretation of colloidal dispersion's stability. Building upon the pioneering work of Gouy-Chapman-Stern theory (Oldham 2008; Sposito 2018; Sridharan and Jayadeva 1982), numerous improvements or modifications to the EDL modeling were made to numerically determine the two potentials according to certain given electrochemical conditions (e.g., electrical intensity, surface charge density, dielectric property) (Hou et al. 2009; Li et al. 2004; Liu et al. 2015; Tang et al. 2015; Trefalt et al. 2016). In this study, the theory recently developed by (Liu et al. 2019) was employed to determine the Stern potential of illite suspensions at the four examined ionic strengths. One highlighted advantage of this theory is that the effect of dielectric saturation is considered in order to account for the dielectric decrease in a strong electrostatic field at the solid-liquid surface (Ben-Yaakov et al. 2011; Gupta and Stone 2018; Nakayama and Andelman 2015), which is usually ignored in some studies based on the Gouy-Chapman-Stern model. Figure 4a presents the calculated Stern potential of the illite suspensions at different ionic strengths, and it shows that the Stern potential decreases exponentially from -0.34 to, -0.32, and -0.29 V at 0.09, 0.17 and 0.60 M, respectively. With the determined Stern potentials, the potential at the midplane of two adjacent illite particles separated at nanoscale distances can then be estimated with the following equation (Tang et al. 2015):

$$\frac{\pi}{2}\left[1+\left(\frac{1}{2}\right)^{2} e^{\frac{2ZF\varphi\left(\frac{d}{2}\right)}{RT}}+\left(\frac{3}{8}\right)^{2} e^{\frac{4ZF\varphi(\frac{d}{2})}{RT}}\right]-\arcsin e^{\frac{ZF\varphi_0-ZF\varphi(\frac{d}{2})}{2RT}}=\frac{1}{4}d\kappa e^{-\frac{ZF\varphi(\frac{d}{2})}{2RT}} \tag{4.6}$$

where φ_0 is the Stern potential of clay particles determined with the theory developed by Liu *et al.* (2019), Z the valence of electrolyte ions (e.g., ±1 for the NaCl solution in this study), R the gas constant (8.314 J/K/mol), and $\varphi(d/2)$ is the mid-plane potential to be determined. Finally, based on the Langmuir equation (Ducker et al. 1992; Langmuir 1938), the EDL repulsion between two adjacent illite particles can be calculated with the following equation:

$$P_{EDL}(\lambda) = \frac{2}{102} RTc_0 \left\{ \cosh \left[\frac{F\varphi\left(\frac{d}{2}\right)}{RT} \right] - 1 \right\} \tag{7}$$

where c_0 is the electrolyte concentration of the bulk solution (M). The calculated EDL repulsion between two adjacent illite particles at selected distances (i.e., from 0.1 to 1 nm) is presented in Figure 4.4b. It shows that the EDL repulsion decreases with increasing both ionic strength and particle distance, which validates again the enhanced flocculation of illite particles due to increased ionic strength, as observed in the experiments.

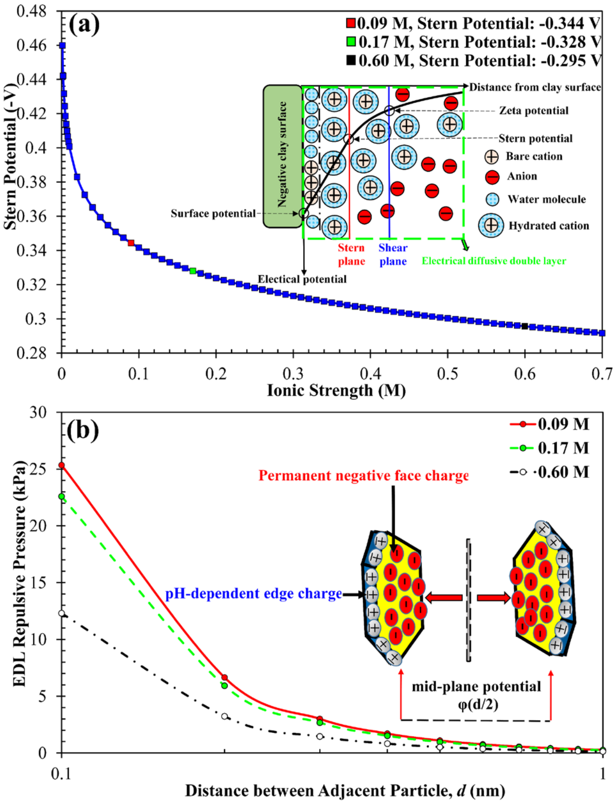

Figure 4.4 Quantification of surface chemistry of illite particles at different ionic strengths: (a) estimated stern potential (-V) versus ionic strength, which marks the potential value of ionic strength of 0.09, 0.17, and 0.60 M; (b) electrostatic repulsive pressure between the adjacent illite particles.

4.3.3 Effects of pH

Figure 4.5 shows the PSD curves of illite suspensions at the four ionic strengths and two titrated pHs, 4.51, and 2.25, and the corresponding deconvolution results are summarized in Tables 4 and 5. Similar to the illite suspensions at the original pH 8.61, multimodal PSD curves were observed for the two groups of suspensions with the acidic pHs. Again, at each acidic pH, increasing the ionic strength also promoted the flocculation, as demonstrated by the shift of the PSD curves toward the larger-sized ranges, together with the correspondingly decreased fractions of primary particle groups. For instance, the primary particles fraction even became zero at pH 4.51 (Table 4.4). This is due to the fact that a large percentage of primary particles joined together to form larger-sized flocs during the flocculation process.

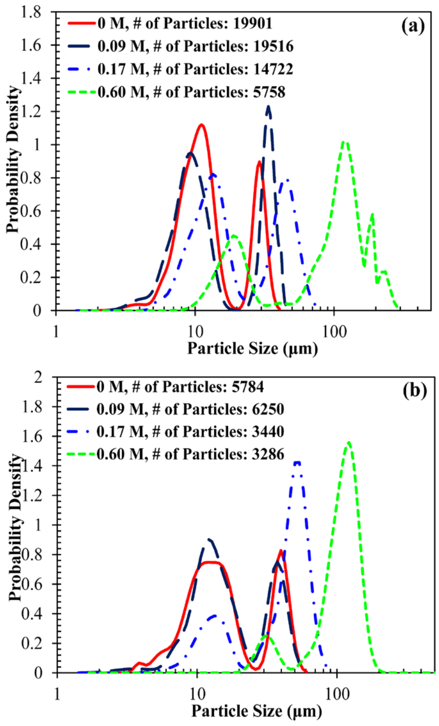

Figure 4.5 PDF curves of acid-titrated illite suspensions at the four ionic strengths: (a) pH 4.51; (b) pH 2.25

Table 4.4 Summary of fraction and mean particle size for each deconvoluted constituent in illite-salt-HCl suspensions (pH 4.51).

Ionic strength (M)	Deconvoluted mode #	Mean size (μm)	Fraction (% by number)	Particle size group
0	1	3.99	2.01	Primary particles
	2	5.78	2.33	
	3	8.65	32.46	
	4	11.99	38.48	Flocculi
	5	29.26	24.73	
0.09	1	4.22	3.55	Primary Particles
	2	6.15	7.00	
	3	9.18	43.69	
	4	12.28	11.44	Flocculi
	5	25.76	0.58	
	6	33.91	32.70	Microflocs
	7	41.60	1.04	
0.17	1	5.49	0.90	Primary Particles
	2	9.75	23.31	
	3	14.41	34.14	Flocculi
	4	27.36	2.41	
	5	45.57	39.24	Microflocs
0.60	1	15.70	12.14	Flocculi
	2	20.52	14.48	
	3	41.35	1.95	Microflocs
	4	77.68	11.62	
	5	123.19	46.87	
	6	183.87	7.03	
	7	228.41	5.92	Macroflocs

Figure 4.6 compares the CDF-type PSD curves of illite suspensions at the four ionic strengths and three pHs. It is worth noting that, compared with the original pH 8.61, the microfloc groups in the two acidic pHs suspensions account for higher fractions. Also, the highest ionic strength, 0.60 M, even further increases the fraction of microflocs, and the macroflocs with a particle size of > 200 μm are formed at this ionic strength (Tables 4 and 5). These results clearly demonstrate the coupling effects of low pHs (i.e., 4.51 and 2.25) and high ionic strengths (i.e., 0.60 M) that work together to promote flocculation of illite particles, resulting in even larger, silt/sand-sized macroflocs, which may involve the

merging and joining of primary illite particles, floccule, and microflocs. In fact, prior work (Tan et al. 2012; Zhang et al. 2013b) studying the effects of two exopolymers (i.e., xanthan gum and guar gum) with different polarities on the PSD kinetics of illite (IMt-1) suspensions found that, while the illite-exopolymer microflocs of ~100 μm in size formed by adding the guar gum at an exopolymer to clay ratio of > 5 wt.% or higher, no macroflocs of > 200 μm in size exist in the exopolymer-modified illite suspensions. Such a different phenomenon may be attributed to the fact that the illite suspensions in these studies were prepared in DI water at the original pH 8.61, and thus the acid-base surface properties of illite (as further discussed in the next paragraph) coupled with the ionic strength was not utilized.

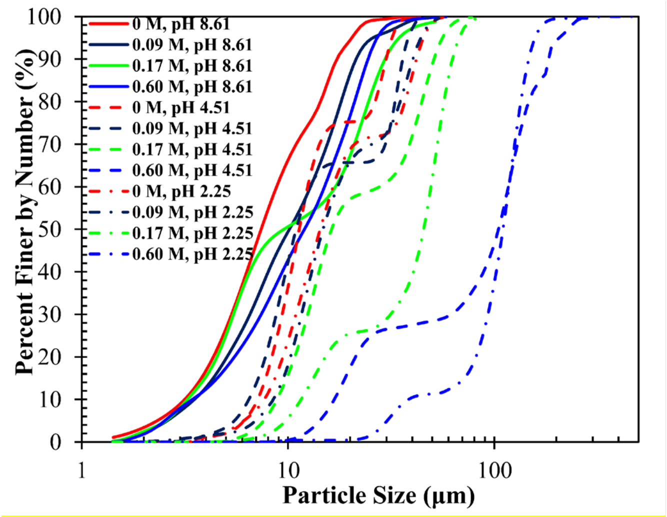

Figure 4.6 CDF curves of illite salt-HCl suspensions

As a typical 2:1 non-expanding mineral, illite mainly forms by the weathering of primary felsic silicates (e.g., feldspar and quartz) or through the alteration of other mica-group minerals (e.g., muscovite) under high pH conditions, which leads to its highly irregular crystalline structure responsible for the relatively higher negative layer charges due to isomorphous substitutions (Borkovec et al. 2012; Laird 2006; Neumann et al. 2002). Another feature of illite, also common to most clay minerals, is the octahedral Al-OH and tetrahedral Si-OH groups at the broken edges. Such hydroxyl-terminated planes increase the heterogeneity and complexity of surface charges of illite particles, depending upon the protonation/deprotonation process occurring on these amphoteric or pH-dependent charge sites (Bolt 1985; Du et al. 1997; Korolev and Nesterov 2018; Liu 2001; Tombácz and Szekeres 2004, 2006). Thus, for dilute aqueous solutions, the stability of illite suspensions can mostly be maintained due to the completely dispersed particle arrangements caused by the strong electrostatic repulsion due to the overlapped EDL of primary particle and hence the EDL repulsion (Van Olphen 1977). The reduced EDL or ion shielding of surface charges induced by increasing the ionic strength, to some extent, enables the particles to approach and interact with each other, thusly forming higher fractions of larger-sized flocs of up to ~45 μm in size, mainly through surface contact with face-to-face (FF) compacted, stacked particle arrangements (Deirieh et al. 2018; Dor et al. 2020; Gregory 1989).

The formation of microflocs and macroflocs with much larger sizes, however, is unfortunately rare, mainly owing to the alkaline pH 8.61 of the pure illite suspension. As such, the edge charges of illite particles are most likely to be negative provided that the PZC_{edge} is smaller than the suspension pH, thus preventing the edge-to-face (EF) arrangements that can reportedly help increase the size of flocs by forming patch-like networks through the attraction of two opposite charged surfaces (i.e., the permanent negative charges on the face and positive charges on edge) (Gupta et al. 2011; Liu et al. 2020a; Mietta et al. 2009; Wilkinson et al. 2018). Hence, understanding the PZC_{edge} of illite is of great significance to interpret the acid-base surface properties of illite particles and thus the formation mechanisms of micro- and macro-scale illite flocs. To date, most prior experimental studies used potentiometric titration, a routine technique to measure the PZC of amphoteric surfaces of oxides (e.g., alumina and silica) and also to characterize the surface acid-base properties of different clay minerals, such as the density of proton-active functional groups on clay mineral surfaces over a wide pH range (e.g., usually from the acidic to alkaline pH) coupled with varying ionic strengths (Du et al. 1997; Duc et al. 2005; Liu et al. 2018).

Unlike the typical results of the acid-base titration of oxides, however, the reversible net protons on clay mineral surfaces usually fail to intersect at a fixed point with different ionic strengths. Thus the PZC_{edge} of clay minerals cannot be directly determined from the titration curve. Particularly, it was widely reported that the surface proton concentration on the clay minerals is inversely proportional to the ionic strength of the solutions over a range of pHs (Gao and Mucci 2001; Hao et al. 2018; Jara et al. 2005; Tournassat et al. 2016). That is, there exist higher negative charges on the edge surface at low ionic strengths, which may be one of the reasons why there exists no significant difference in the PSD of illite suspensions at the three low ionic strengths (i.e., 0, 0.09, and 0.17 M) and three pHs (i.e., 8.61, 4.51, and 2.25).

To account explicitly for such effect of ionic strength on the PZC_{edge} of clay minerals, a conceptual model developed by Tombácz and Szekeres (2004) to explain the patch-wise surface charge heterogeneity of individual Na-montmorillonite particle under different ionic strengths and pHs is further extended here to illite, which is much thicker than the Na-montmorillonite 2:1 layer, as illustrated in Figure 4.7. Basically, the EDL can form on both the face with fixed charges and the edge with variable charges. When the ionic strength of indifferent electrolytes is low, much thicker EDL (also termed as the dominant EDL) forms on the clay face surface, while the edge surfaces have higher charge density but much smaller area, and hence the EDL thickness is much smaller. As such, a spill-over effect (Tombácz and Szekeres 2004) takes place, where the thicker face EDL extends around the edge to partially cover the smaller and thinner edge EDL, and hence the parts of the edge EDL near the two face surfaces are covered and hidden by the large, thicker face EDL. Further noteworthy is the difference in the EDL spillover between a Na-montmorillonite 2:1 layer and an illite particle. Since the latter is much thicker, complete spillover to hide the entire edge EDL is unlikely to occur for illite. The spillover may affect interparticle interactions in two different aspects: (1) the measurable edge charges become smaller due to the hidden part of the edge EDL covered by the face EDL spillover, and (2) the thicker face EDL spilled over the edge can separate and hence prevent close EF and EE arrangements, and thus flocculation may be difficult. On the contrary, the hidden EDL can emerge at higher ionic strengths (e.g., 0.60 M NaCl in this study), which suppress the dominant face EDL, and hence allow closer EF and EE arrangements. Therefore, the ionic strength of indifferent electrolytes plays a unique role in clay flocculation, which further affects the microfabrics resulting from the interactions between the individual clay particles and thus flocs with varied sizes. For instance, the formation of illite macroflocs of > 200 μm in size at 0.60 M NaCl ionic strength and $pH < PZC_{edge}$ is primarily caused by the strong electrostatic attraction between the oppositely charged sites on the face and edge surfaces, which renders the formation of EF hetero-coagulated fabric and FF stacking of particles due to the decreased EDL repulsion (as schematically illustrated in Figure 4.7). Both interparticle arrangements promote the joining of illite particles and hence the formation of large-sized, thick illite flocs with a complex flocculated-and-aggregated internal microfabric.

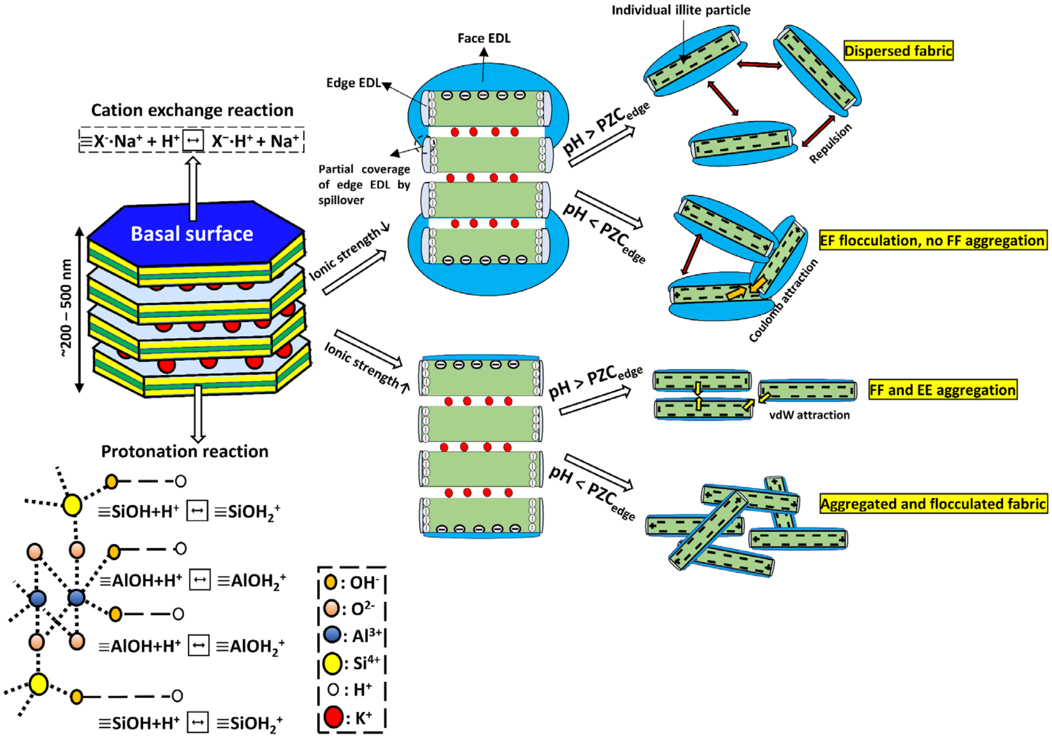

Figure 4.7 Schematic illustration of the origin of charge heterogeneity for individual illite particles, and formation of various microfabric patterns dedicated by the ionic strengths and pH of the illite suspensions (after Tombácz and Szekeres, 2004)

Finally, it is noteworthy that the determination of PZC_{edge} of the studied illite via standard potentiometric titration was not performed in this study. However, reference data is available from prior work (Shao et al. 2019) that used atomic force microscopy to quantify the edge and basal surface charges of illite (IMt-1) at different pHs with a fixed concentration of 0.01 M KCl solution. The result showed that, on the illite edge, an attractive interaction was observed at pH 3.0, while the interaction slightly changed to repulsion at pH 5.0 and then increased gradually at pH up to 10.0, suggesting that $\mathrm{PZC_{edge}}$ of the illite should be less than 3.0 in a 0.01 M KCl solution. This finding partially supports the experimental results obtained in the present study, i.e., larger-sized microflocs and macroflocs (> 200 μm) can form at pH 2.25 in a 0.60 M NaCl solution. For pH 4.51, however, these particle groups can still form in the same 0.60 M NaCl solution. Such contradiction can then be explained by the aforementioned coupled effects of ionic strength and pH on the flocculation of illite particles.

4.3.4 Effects of hydrodynamic shearing

Figure 4.8 and Figure 4.9 presents the multimodal PDF- and CDF-based PSD curves of illite suspensions at fixed 0.60 M NaCl solution and pH 8.61, but prepared with three shaking speeds and three shaking durations (Table 4.2). The shifting of the PSD curves clearly shows that larger-sized flocs gradually form with increasing the shaking duration. At each shaking speed, the median size d_{50} tends to increase with the shaking time, indicating the temporal flocculation process (i.e., from 10 to 60 min). Particularly, the d_{50} obtained at 150 oscillation/min and 60 min duration is nearly the same as the counterpart obtained at 24 h shaking time, implying that a steady state of PSD evolution was reached at 60 min shaking. This agrees well with the general conclusion that the PSD kinetics of shear-induced flocculation usually reach a steady-state within a relatively short period (e.g., 10 to 60 min) (Mietta et al. 2009; Wang et al. 2018; Yu et al. 2011; Zhang et al. 2013b, 2019a). Another consistent trend is that, at the same duration of 10 or 60 min, the d_{50} decreases as the shaking speed increases from 150 to 300 oscillation/min, while the d_{50} at the duration of 30 min shows the opposite trend with increasing the shaking speed, implying a transition state of the PSD evolution caused by varying the shaking speed. Based on the results of PDF-based deconvolution of the multimodal PSD curves, Figure 4.10 summarizes the PSD kinetics of the illite suspensions affected by different hydrodynamic flowing conditions. Clearly, the means of different particle groups at different shaking speeds increase with shaking duration, while the fractions of primary particles, but not the counterparts of flocculi and microflocs, generally decrease with increasing shaking duration, indicating that more smaller particles join together during the continuous shaking to form larger-sized flocculi and microflocs.

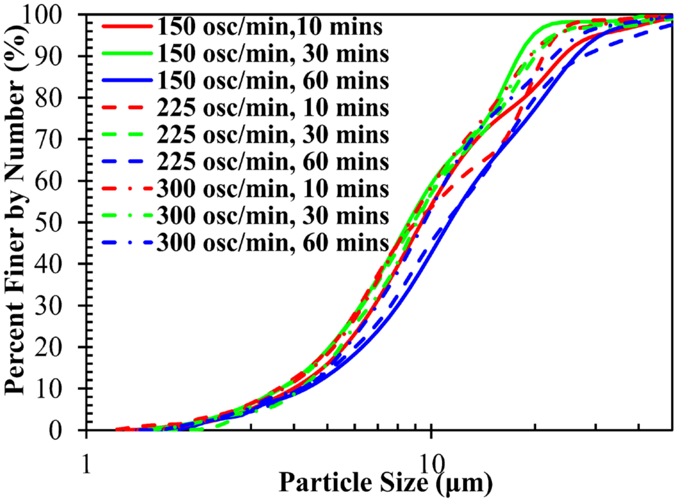

Figure 4.8 PDF curves of illite suspensions under different hydrodynamic conditions: (a) 150 oscillation/min; (b) 225 oscillation/min; (c) 300 oscillation/min

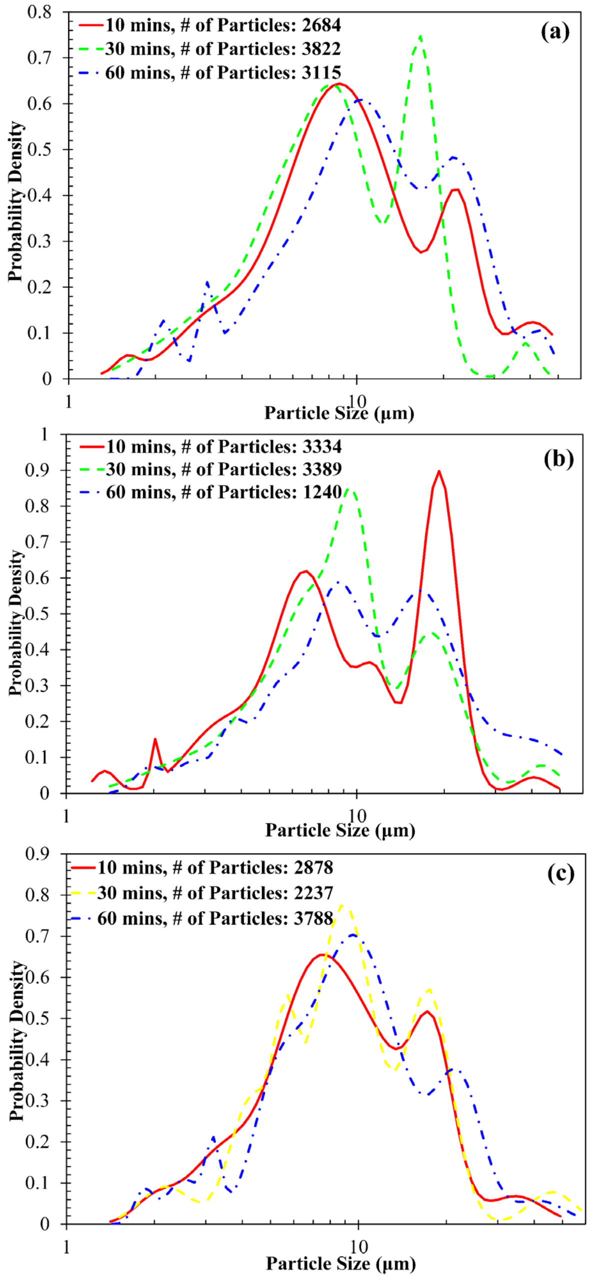

Figure 4.9 CDF curves of flocculated illite suspensions under different hydrodynamic conditions

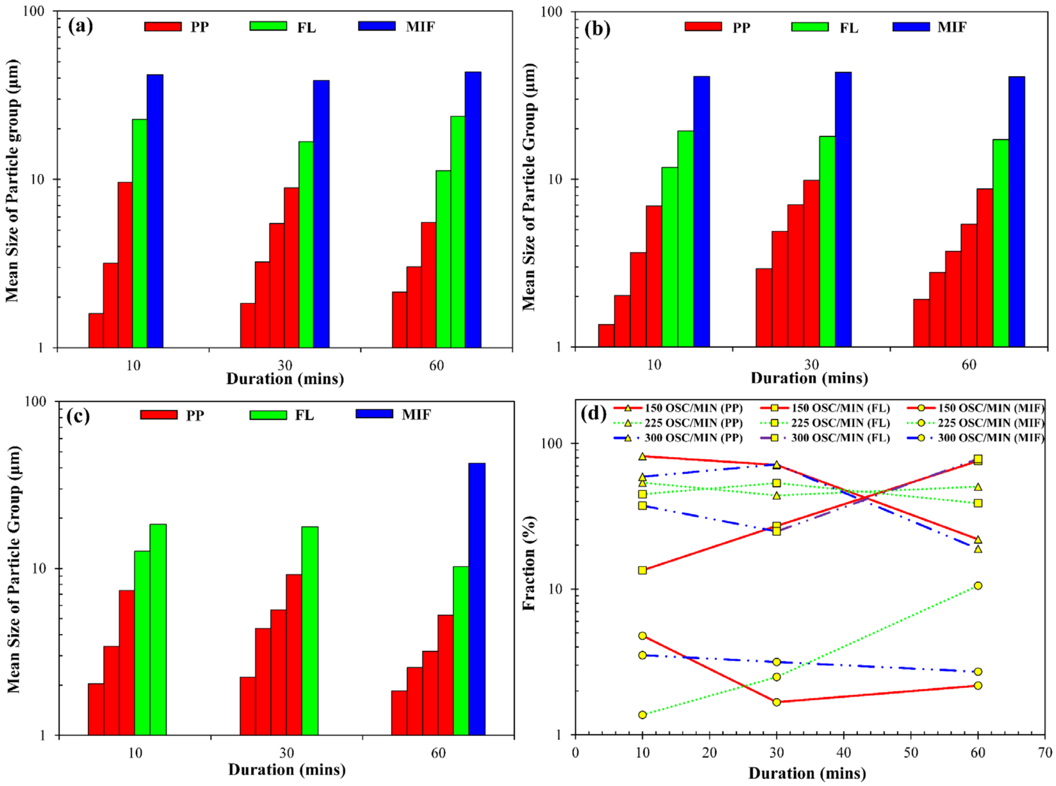

Figure 4.10 Mean size of deconvoluted particle groups in terms of hydrodynamic shearing force: (a) 150 oscillation/min; (b) 225 oscillation/min; (c) 300 oscillation/min; (d) fraction (% by number) of particle size groups at different durations and shaking speeds (Primary particles: PP; Flocculi: FL; Microflocs: MIF)

The above results clearly demonstrate the effects of hydrodynamic shearing conditions (i.e., shaking speed and duration) on the flocculation of suspended illite particles and thus variable PSD kinetics. Essentially, the PSD kinetics of illite flocs in flowing water is controlled by the hydrodynamic shear stresses applied to the flocs, which are usually characterized by the shear rate G for a homogenous and isotropic turbulence (Camp and Stein 1943):

$$G = \sqrt{\frac{\varepsilon}{\nu}} \tag{4.8}$$

where ε is the rate of energy dissipation per unit mass of fluid and v the kinematic viscosity, which can then be related to the floc size by the following equation (Parker et al. 1972):

$$d_0 = CG^{-\gamma} \tag{4.9}$$

where d_0 is the floc size, C the constant of floc strength coefficient, and γ the stable floc size exponent. Linearization of Eq. (4.9) enables the explicit demonstration of the relationship between the floc size and shear rate, i.e., for the same method used for particle flocculation experiments, the final floc size is negatively proportional to the average gradient. Based upon this theoretical relationship, the change in floc size can also be analyzed from the perspective of transfer of turbulent energy as a result of moving eddies with different sizes (Bache 2004; Jarvis et al. 2005a; Landhal and Mollo-Christensen 1992; Marchetti et al. 2013), as described by the Kolmogoroff microscale:

$$\eta = \left(\frac{\mu^3}{\varepsilon} \right)^{1/4} \tag{4.10}$$

where η is the Kolmogoroff's microscale of turbulence and μ the kinetic viscosity. With these theoretical bases, a better understanding of the flocculation and PSD kinetics in illite suspensions induced by different hydrodynamic shearing can be achieved. As the shaking speed increases, the average shearing gradient or shearing rate increases, and thus the induced hydrodynamic shear stress becomes more turbulent, which usually contains various eddies with very small sized ones, resulting in a higher energy dissipation that is responsible for floc breakdown. Hence, smaller flocs tend to be formed due to the increased breakdown, as characterized by the median size d_{50} of the overall PSD.

Furthermore, based on the variations in the d_{50} for the three shaking speeds at a given shaking duration, the hydrodynamic shear stress induced by different shaking speeds, to some extent, affects the strength of flocs and thus also the size evolution. Two mechanisms were proposed for the breakdown of flocs under different shearing conditions, including surface erosion and large-scale fragmentation (Jarvis et al. 2005a). While the former refers to the process where the relatively smaller particles are removed from the surface of existing flocs exerted by tangential stress, the latter is the cleavage of flocs into certain number of smaller pieces applied by the tensile stress (Yeung and Pelton 1996). The reason for such different breakage modes may be related to the effects of initial strength dictated by the hydrodynamic shear stress. That is, the higher the applied hydrodynamic shear stress, the stronger the newly formed flocs at the initial stages of flocculation (e.g., at 10 and 30 min durations) and thus no reduction in particle sizes. This explains the variation in the d_{50} for the three shaking speeds, i.e., the overall particle sizes decrease from 150 to 225 oscillation/min, while the counterparts at 300 oscillation/min show the opposite trend. After the steady-state (i.e., 60 min duration) is reached, however, continuous shaking at different speeds leads to different final floc sizes, i.e., the d_{50} at 150 and 225 oscillation/min are relatively greater than that at the 300 oscillation/min, which may be due to the continuous prevalent breakage due to floc collision more than floc re-formation at the higher shaking speeds (He et al. 2012; Lee and Kim 2018; Wang et al. 2018; Zhang et al. 2019a).

Finally, one more secondary factor that may affect the PSD kinetics of clay suspensions is the time-dependent thixotropy, a strengthening phenomenon widely observed in colloidal dispersions and emulsions (e.g., paints). In general, the magnitude or intensity of shearing decreases the stiffness and strength of colloidal suspensions. However, the clay suspension considered in this study had a very low concentration, 0.4 g/L, which makes the thixotropic hardening process less important, when compared with the hydrodynamic shearing. In other words, shearing can further decrease the strength of individual clay flocs due to the reversed process of thixotropy, and hence higher shear stresses breakdown more flocs. Nevertheless, the illite flocs may experience thixotropic hardening and strength regaining upon resting or after the shearing stops (Zhang et al. 2013a).

4.3.5 Practical implications

Significant effort was made to investigate clay flocculation and pertinent PSD kinetics of suspended cohesive sediments in natural waters and laboratory conditions over the past decades, partly due to the widespread abundance of clay minerals in natural environments and their physicochemically active surfaces that usually result in highly complex, dynamic interactions in the aquatic settings. As a representative, non-expanding 2:1 clay mineral with relatively higher layer charges, the colloidal systems composed of dispersed illite particles at low ionic strengths and high pHs are usually quite stable. However, at varying the aquatic chemistry conditions (e.g., elevated salinities and acidic pHs), complex PSD kinetics can be observed via the formation of flocs of up to a few hundred (e.g., ~ 300 - 400) micrometers in size. In addition to the chemical conditions, illite flocculation is also significantly affected by the physical processes, such as the hydrodynamic forcing that applies shear or tensile stresses to the suspended particles and flocs.

The above results and findings on the PSD kinetics of illite suspensions and the underlying illite-water-salt interactions can provide insights into geotechnical and geoenvironmental practices where illite-rich geomaterials are involved, such as flocculation and coagulation of suspended particles in sludge dewatering, drilling mud stability and disposal (e.g., the flocculation of illite particles in drilling muds due to the transformation of smectite to illite in the high temperature and high-pressure environments), and management of clay-rich tailings (Du et al. 2018; Kiliaris and Papaspyrides 2010; Liu et al. 2020a; Shaikh et al. 2017; Wei et al. 2018; Zhao et al. 2021).

Furthermore, as one of the main solid components (e.g., clay minerals) of suspended cohesive sediments in natural aquatic environments, understanding the PSD kinetics of illite under different chemical and physical conditions (e.g., salinity, pH, hydrodynamic shearing) has many important environmental implications. For example, upon completion of the flocculation process, the resulting larger flocs settle faster to the bottom of the water body when compared with smaller primary particles and other suspended solids, due to the porous structure of flocs that allows the creeping flow through the pores. They then finally become an important, load-bearing skeleton constituent of fine-grained cohesive sediments that are of great importance to the healthy functioning of the natural aquatic ecosystem. Moreover, the PSD of these flocs are further complicated upon re-suspension and subsequent transport with other cohesive sediments by the highly dynamic aqueous flow (Hermawan et al. 2003, 2004; Muka 2015). Therefore, the PSD kinetics of clay flocculation is a key parameter in predicting the settling velocity of flocs by estimating the flocs' microstructure and density that both play an important role in developing numerical models for the transport, settling, and re-suspension of cohesive sediments (Tran and Strom 2019; Yang et al. 2009; Zhang et al. 2009).

Finally, knowledge of the particle size, an essential parameter quantifying the dimension of flocs, is crucial for characterizing the mechanical properties of clay flocs, since the size or diameter of flocs is mathematically demanded by the mechanical constitutive laws. With the size data, the mechanical properties (e.g., elastic moduli, yield stress) of flocs can then be compared and normalized to offer valuable information concerning the flocs in specific scenarios, such as floc breakdown and re-aggregation, compaction and consolidation of the bottom bed made of settled flocs, optical properties of the water with flocs, and remote sensing (e.g., acoustic wave propagation and scattering) in estuarine environments (Green and Blough 1994; Hatcher et al. 2001; Hill 1998; Zhang et al. 2013b).

4.4 Conclusions

A systematic experimental investigation was conducted to investigate the particle size distribution kinetics of flocculated illite suspensions affected by ionic strength, pH, and hydrodynamic shearing. By employing a new data binning criterion, the Bin Size Index method, the experimental particle size histograms of illite flocs prepared under different environmental conditions were constructed with a rational optimal bin size, followed by probability density function-based deconvolution. Based on the above analyses of results, the main conclusions can be drawn as follows:

- Increasing the ionic strength of the clay suspensions promotes larger-sized illite flocs, due to the suppression of the electrical double layer on clay face surfaces, which is closely related to the electrokinetic potential of illite particles;
- Acidic pHs result in higher fractions of larger-sized particle size groups, including microflocs of ~50 to 100 μm and macroflocs of > 200 μm in size. The critical pH for flocculation is affected by both the ionic strength and the point of zero charge of illite edge surface; A lower pH further facilitates the flocculation, due to opposite charges on the face and edge surfaces, which leads to face-to-edge electrostatic attractions;
- An interesting, shearing-dependent evolution pattern of particle size distributions was observed, and the highest hydrodynamic shearing leads to smaller but likely stronger illite flocs with a median size of ~9 mm;
- The new Bin Size Index method developed to assist data binning, histogram construction, and subsequent deconvolution analysis yields more accurate results with different, clearly distinguished characteristic particle groups.

Appendix: Procedure of Image Processing Using ImageJ

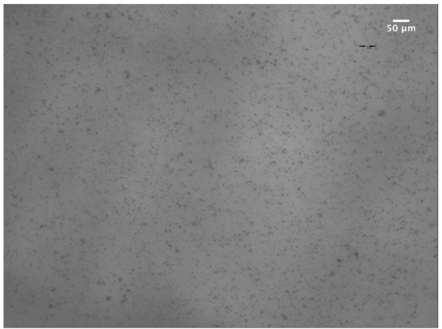

1. Convert the selected image to 8-bit type

2. Subtraction of uneven background light

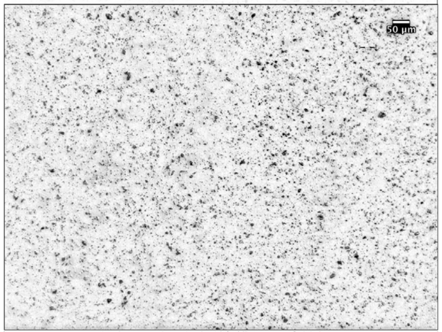

3. Contrasting and segmentation for differentiating the particle border

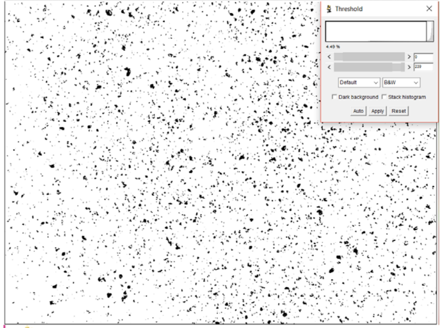

4. Thresholding for producing a binary image of black colored particles with white background

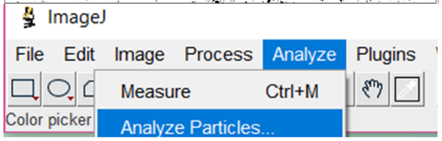

5. Measurement of particle sizes by running builit-in "Analyze Particles" function

Acknowledgements

This work was supported by the U.S. National Science Foundation (NSF) under Award No. CMMI 1702881. The first author also received partial support from the Charles F. Perrell Scholarship. Any opinions, findings, and conclusions expressed in this paper are those of the authors and do not necessarily reflect the views of the NSF.

CHAPTER 5

MECHANICS AND MICROFABRIC OF CLAY AGGREGATES UNRAVELED BY MICROCOMPRESSION TESTING

A systematic experimental investigation is presented of the mechanics and microfabric of clay aggregates of three source clay minerals, kaolinite (KGa-1b), illite (IMt-1), and Na-smectite (SWy-2), that are representative of three major species of clay minerals abundant in natural soils. Clay-salt (NaCl) suspensions with varying salinity (2, 5, 10, 20, 35 ppt) were subject to a swing motion by a wrist-action shaker to prepare clay aggregates. A custom setup for compression testing was used to exert unconfined vertical loading on the individual clay aggregates, followed by data interpretation using Hertz elastic contact theory that derives two important elastic properties (i.e., Young's modulus, yield shear strength) of individual aggregates. We use Weibull statistical analysis to generate expected mean values of Young's modulus and yield shear strength. The results show that the mechanical characteristics of clay aggregates are affected by the mineralogical compositions and porewater chemistry that control the clay particle interactions. Moreover, the Weibull modulus of aggregates of KGa-1b aggregates and the other two minerals shows a contrasting trend with increasing salinity, indicating the difference of the dominant microfabric pattern existing in these aggregates. Finally, an innovative method for characterizing multiple aggregates (two-clay aggregate column, three-clay-aggregate column, and agglomerate of clay aggregates) under confined loading scenarios is presented, which can provide insights into the advancement of understanding of the clay behavior from the inter-aggregate perspective.

5.1 Introduction

In contrast to most continuous bodies (continua), soils are distinctly characterized by their particulate-based properties that inherently dedicate the behaviors of bulk soils in response to external mechanical loading, i.e., the macroscopic behaviors of soils (e.g., consolidation, shearing, creeping, fracture) derive from the microscale or mesoscale particle interactions (Mitchell and Soga 2005). Given such unique mechanisms in terms of the multi-scale loading transmission within the soil skeleton, there has been extensive prior research to experimentally and numerically investigate constitutive laws and properties of soils as typical particulate materials. For instance, with the progressive development of grain-scale discrete analysis methods over the past decades, notably the discrete element method (DEM), major advancements in understanding the micromechanics of cohesionless granular soils (i.e., sands and gravels with the individual particle length scale of mm) have been achieved mainly by generating three-dimensional (3D) agglomerate model composed of a massive number of smaller spherical sub-particles (Cundall and Strack 1979). Particle-to-particle interactions, such as interparticle contact forces and particle crushing at the microscale, can then be observed at the level of individual granules or at the particle assembly level being subject to the simulated external loading (e.g., compression, shearing) (De Bono and McDowell 2014; Cil et al. 2013; Cil and Alshibli 2012; Shi et al. 2016; Wu and Wang 2020). The mechanical properties of granules computed from simulation (e.g., crushing strength, yield strength, Young's modulus) can be further verified by the load-deformation curves from corresponding experimental measurements (e.g., one-dimensional compression testing) which are usually convenient to conduct due to the large size (i.e., ~mm to m) of the specimens (Amirrahmat et al. 2020; Cil and Alshibli 2014; Liu et al. 2021; Wang et al. 2015b).

Compared with the significant works on granular soils, however, much less progress has been made in understanding the behavior of clays (representative of fine-grained cohesive soils) as a particulate system, which is mainly attributed to the distinct characteristics of clay minerals, the primary constituents of clays consisting of a group of phyllosilicate minerals. Unlike individual granules, the size of individual clay particles (stacks of crystalline sheet arrangements) is usually in the range of < 2 μm and they usually possess a platy-like shape with a relatively high specific surface area (SSA) (Moore and Reynolds 1997), which makes it experimentally challenging to directly perform mechanical testing on the individual clay particles as easily done on the granular particles, except for using some advanced microscopy-based techniques (e.g., atomic force microscopy) that are generally expensive and high demand the experimental skills of users (Kunz et al. 2009). Also, owing to the characteristic isomorphous substitutions (i.e., defects in the crystal structure of clay minerals mainly involving the substitutions of Al^{3+} for Si^{4+} and Mg^{2+} for Al^{3+} in a tetrahedral and octahedral sheet, respectively), naturally occurring clay minerals possess different degrees of permanent negative charges on the face surface and pH-dependent charges on the broken edge surfaces (Çelik 2004; Yariv and Cross 1979). These intrinsic surface charges make clay minerals chemically active in all-natural and laboratory aqueous environments, leading to very complex surface forces (combination of van der Waals force, electrostatic repulsion, and other interaction forces or bonding) such that the conventional modeling methods (e.g., DEM and finite element method (FEM)) are inherently challenging to simulate the particle-level interactions of clay particles, particularly in the aqueous environments.

Although the complex geometrical characteristics and active surface properties result in difficulties in studying the mechanics of individual clay particles, these features, on the other hand, coincidentally provide opportunities from the different size scales. Owing to their charged surface and high SSA, individual clay particles are prone to intensively interact with dissolved ions, molecules, and a variety of particulate materials with the chemically active surface (a process known as the flocculation and aggregation of the clay minerals), forming groups of mesoscale clay particles (i.e., size range in the order of ~10 to ~10^2 μm) structurally associated via small-scale surface and interfacial forces (Maggi 2005; Shaikh et al. 2017; Zhang et al. 2013b) whose particle size and mechanical properties are highly dependent upon the formation environment that involves highly complex particle interaction mechanism. One key factor is water chemistry, including the types and concentrations of dissolved ions, salts, or high-molecular-weight polymers with functional groups that render different polarities (e.g., extracellular polymeric substances (EPS)) (Tan et al. 2014b), which facilitates the formation of larger-sized clay particles mainly by: (1) suppressing the electrical double layer (EDL) of dispersed clay particles from the increase in the ionic concentrations of suspensions (DLVO theory) (Derjaguin and Landau 1993, 1941); (2) adjusting the pH-dependent edge charge to positive (acid-base reactions) (Konduri and Fatehi 2017; Tombácz and Szekeres 2004; Wilkinson et al. 2018); (3) bonding the clay particles either during the process of re-precipitation or recrystallization (resulting in the formation of cementation) (Zhang et al. 2004a); or (4) via the bridging-chain effects from the EPS (Furukawa et al. 2009). These interactions, in turn, result in the formation of a variety of microfabrics within the particle groups, primarily including face-to-face (FF), face-to-edge (FE), and edge-to-edge (EE) associated particle assemblages that significantly dictate the hydro-mechanical response (e.g., shear resistance, creep, consolidation properties) based upon the porous structure throughout the three-dimensional particulate space (Deirieh et al. 2018; Delage et al. 1996; Kim and Palomino 2009; Li et al. 2020; Martin and Ladd 1975). Furthermore, the hydrodynamic flowing condition in natural aqueous environments significantly impacts the flocculation and aggregation process by exerting shear stress within the cohesive sediments (of which clay minerals are the main solid constituents) that determines the survival of newly formed particle groups (Jarvis et al. 2005b), i.e., relatively larger-sized clay particle groups are formed as a result of their higher shear strength for resisting against the flowing stress (Mietta et al. 2009). Through transportation and sedimentation, these particle groups are progressively distributed and finally deposited as the basic skeleton of clays that bridges the micro-scale clay particles and macro-scale bulk clays in the terrestrial and marine environments (Mehta et al. 1989). To date, three different terms, i.e., *aggregate* (Dor et al. 2020; Guérin et al. 2019; Moruzzi et al. 2017; Neumann et al. 2002; Tombácz and Szekeres 2006; Zhang et al. 2004b), *floc* (Lavallee et al. 2020; Lee et al. 2012; Tan et al. 2012; Ye et al. 2020; Zhang et al. 2013b, 2019b), and *cluster* (Chang et al. 2009; Kobayashi 1999; Likos and Lu 2001) have been used in the literature to describe these particle groups. Since there still exists no unified term for the description, *aggregate* is selected here for denoting such a fundamental unit of clays for the following sections.

In summary, to study the mechanics of clays from a particulate perspective, it is necessary to employ the coarsening techniques (i.e., flocculation and aggregation of individual clay particles) to prepare mesoscale clay aggregates, considering the complex surface properties and geometry of individual particles that usually render the measurement challenges. This paper presents a systematic experimental study that employs a custom microcompression technique to investigate the mechanical properties (e.g., Young's modulus, yield shear strength) and microfabric of individual aggregates of three source clay minerals, i.e., kaolinite, illite, and Na-smectite, which are abundant in natural soils and representative of different mineralogical compositions with their distinct physicochemical properties. Crystalline Sodium Chloride (NaCl) was used to prepare the saline solution with five salinity levels (2, 5, 10, 20, 35 ppt) which serve as the different background ionic strength for promoting the formation of aggregates. By directly characterizing the individual mesoscale aggregate behavior, the result from this experimental study is expected to provide insights into the understanding of clay mechanics under various water chemistry at the mesoscale level, which further facilitates the development of a bottom-up framework of clay behavior.

5.2 Materials and methods

5.2.1 Clay minerals and preparation of clay aggregates

Three source clay minerals acquired from the US Clay Mineral Society Repository, namely kaolinite (KGa-1b), illite (IMt-1), Na-smectite (SWy-2) were selected as the model minerals for their high purity and abundance in natural soils, whose physicochemical properties are summarized in Table 4.1. To prepare clay aggregates, 0.12 g dry powder of the three clay minerals was firstly soaked in a centrifuge tube filled with 10 mL deionized (DI) water for 16 hours, after which the overnight soaked clay suspension was rapidly mixed with 290 mL NaCl solution with the five salinities for 5 mins in a high-speed stirrer (which is traditionally used for hydrometer test) for better dispersion and unification of clay suspension, finally resulting in a 0.4 g/l pure clay or clay-salt suspension. The well-dispersed suspension was then transferred to a round-bottom flask followed by being subject to a swing-mode vibration using the Burrell Model 95 wrist-action shaker (Burrell Scientific, Pittsburgh, PA, USA) at a shaking speed of 150 oscillation/min for 24 hours. During the continuous vibration induced by the shaker, the clay aggregates were formed in the round-bottom flask because of the effective collisions between particles that overcome the shearing breakage. Particularly, due to its relatively higher layer charge and pH, the illite suspension in saltwater was adjusted by 0.1 N HCl solution to achieve a pH of ~2.8 to 3.0, which was observed to promote the flocculation and aggregation of the illite sample. The underlying reason is that due to their higher layer charges, individual illite particles have a strong repulsive force that prevents aggregation. By adjusting the pH to a value below the point of zero charges, illite suspensions are not stable . Hence, flocculation and aggregation occur, resulting in the formation of mesoscale clay aggregates with the size of greater than ~ 100 μm. Thus, three types of clay minerals and five different salinity levels were used to prepare clay suspensions at a fixed concentration of 0.4 g/l, resulting in 15 different groups of clay aggregates (each with ~14 to 25 aggregates) with sizes in the range of 90 to ~700 μm were selected for each salinity level, considering the high variability in the size of the prepared aggregates.

5.2.2 Micromechanical compression testing setup

Individual clay aggregates were then carefully selected under the microscope and transferred to a homemade fluid cell filled with clear solution taken from the supernatant of the clay suspensions (i.e., after clay aggregates settled to the bottom). The compression of individual clay aggregates was performed in the newly built micromechanical testing system adapted from a GeoJac loading system (Trautwein Soil Testing Equipment, Inc., USA) (Figure 5.1) that controls the whole loading process. Given that the water-formed clay aggregates are naturally soft and tenuous, a miniature load cell with a capacity of 10 mg (Load Cell Central, Inc., USA) was attached to the loading system to meet the high-sensitivity measurement requirement. For each test, individual clay aggregates were subjected to a unidirectional compression between two smooth clean aluminum platens (i.e., the top platen is the punch of the load cell, while the bottom one is attached to the bottom of the fluid cell) at a controlled displacement rate of 0.03 mm/min, and the entire process of loading is also real-time, video-recorded continuously to monitor the change in size and shape of clay aggregates. Finally, the load-deformation data were processed by calibrating the deformation effects of the load cell and supernatant buoyancy and then prepared to extract the mechanical properties of clay aggregates.

5.2.3 Hertzian elastic contact theory

Johnson (1985) presents an analytical solution to the contact problem between an elastic sphere and rigid plates based on Hertzian elastic contact theory, which is used for analyzing the load versus deformation curves of tested clay aggregates. By considering a smooth and frictionless contact scenario in which the soft aggregate sample is compressed between two relatively more rigid plates, the reduced modulus E_{r} measuring the stiffness of aggregate-platen plates contact can be derived with the following equation:

$$E_{\mathrm{r}} = \frac{3P}{\left(Dd^{3}\right)^{1/2}} \tag{5.1}$$

where P is the load applied on the tested aggregate in the elastic regime, D is the nominal diameter of the tested aggregates, and d is the deformation of the tested aggregate (the sum of deformation for two hemispheres being compressed). To determine the onset of yield, the results are plotted with $3P/D^{1/2}$ versus $d^{3/2}$ (Eq (5.1)) to identify the deviation from the ideal linear regression in the experimental load-deformation curve. This method also leads to the determination of yielding shear stress τ of the tested aggregate (Antonyuk et al. 2005; Liu et al. 2021; Zhang et al. 2013a) based on Tresca's yield criterion, which is computed as:

$$\tau = 0.31 p_{\mathrm{max}} = 0.31\left(\frac{24 P_y E_{\mathrm{r}}{}^2}{\pi^3 D^2}\right)^{1/3} \tag{5.2}$$

To calculate Young's modulus of the tested aggregate, the following equation (Oliver and Pharr 1992) is used:

$$\frac{1}{E_r} = \frac{1 - \nu_1^2}{E_1} + \frac{1 - \nu_2^2}{E_2} \tag{5.3}$$

where E_1 and E_2 are Young's modulus of the tested aggregate and substrate, respectively, and ν_1 and ν_2 are their corresponding Poisson's ratios. Noteworthy is that due to the relatively higher Young's modulus of aluminum (in the magnitude of GPa) compared with that of the softer aggregate ($E_2 \gg E_1$, $E_2 \to \infty$), Eq. (5.3) can then be converted into the following equation:

$$\frac{1}{E_{\mathrm{r}}} = \frac{1 - \nu_1^2}{E_1} \tag{5.4}$$

Particularly, it is clear from Eq. (5.4) that the Poisson's ratio has little or no effect on the calculation of Young's modulus for the tested aggregate, therefore a constant Poisson's ratio of 0.3 that has been assumed for general granulate materials is used in this study for all tested aggregates.

5.2.4 Weibull distribution

Owing to the complexity of internal structure and variation of size, there is a large data scatter is expected in derived values of E and τ for all tested aggregates. This scatter is attributed to structural flaws (or weak links) within each aggregate. Here we use Weibull statistical analysis (Weibull, 1939; Weibull, 1951), to interprete variation of the strength data with aggregate size flaw orientation. According to this approach, extracted mechanical properties follow a cumulative distribution in which $F(\mathrm{x})$ represents the probability of failure for individual aggregate:

$$F(\mathrm{x}) = 1 - e^{-\left(\frac{x}{\lambda}\right)^{k}} \tag{5.5}$$

where $x > 0$ is the variable of interest (i.e., E, τ), $k > 0$ is the shape parameter (or Weibull modulus for the distribution of material strength) which will be particularly discussed in later sections, and $\lambda > 0$ is the scale parameter (or nominal strength x_0) of the distribution. By conducting logarithmic arrangement for both sides, Eq (5) can be reformulated as:

$$\ln(-\ln(1 - F(x))) = k \ln\left(\frac{x}{\lambda}\right) = k \ln x_i + b = k \ln \frac{x}{x_0} + b \tag{5.6}$$

Eq. (5.6) depicts the regression line between $\ln(-\ln(1-F(x)))$ and $\ln x_i$; however, the corresponding F_i for each independent variable x_i remains to be determined. To solve this issue, the mean rank method (Huang et al. 2014), which involves the relationship between the rank of experimental data point i and the total number of all data point n, is employed with the following equation:

$$F_i = \frac{i}{n+1} \tag{5.7}$$

With Eq. (5.7), the experimental data points can be fit with Eq. (5.6) to derive the value of k and b through the linear regression for the experimental data points, which in turn, determine the shape parameter, λ, as follows:

$$\lambda = e^{-\frac{b}{k}} \tag{5.8}$$

Finally, the statistical mean value or characteristic value of extracted mechanical properties is determined using the gamma function:

$$E(x) = \lambda \Gamma\left(1 + \frac{1}{k}\right) \tag{5.9}$$

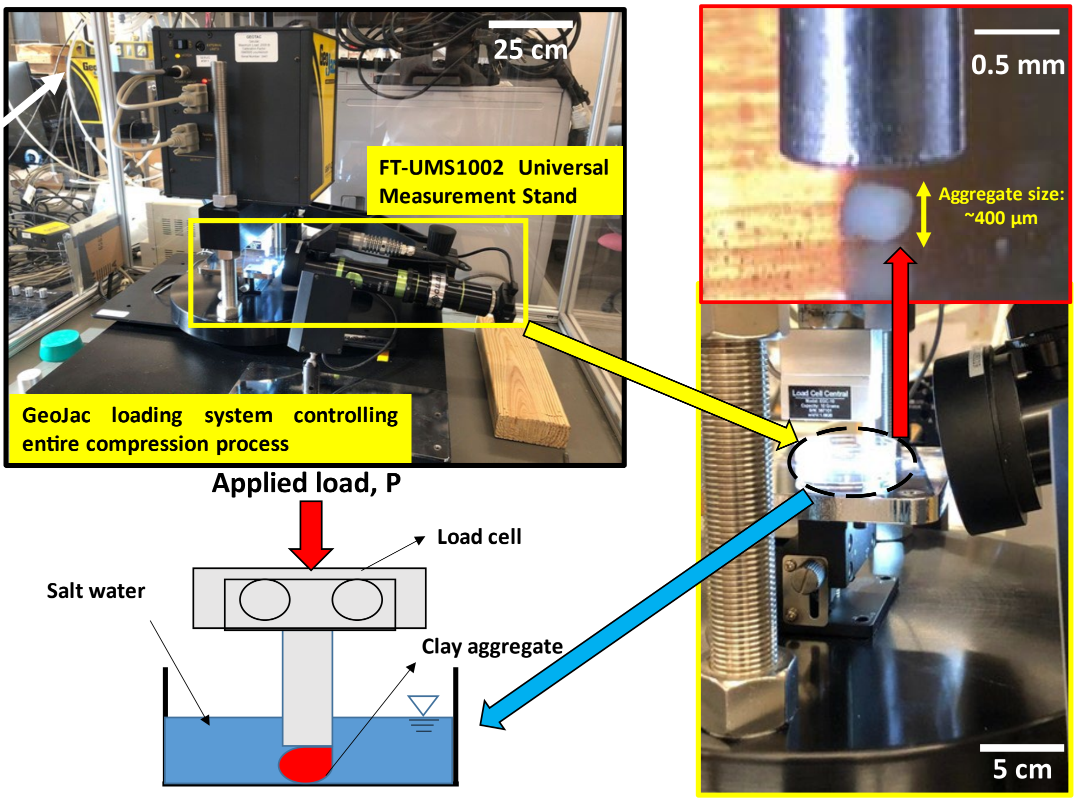

Figure 5.1 Compression testing system of clay aggregates

5.3 Results and discussion

5.3.1 Qualitative description and quantitative extraction of mechanical properties

Typical load-deformation curves of the KGa-1b, IMt-1, and SWy-2 aggregates are presented in Figure 5.2a to c. It is shown that, as compressive loading is continuously applied, three consecutive deformation stages can be discerned among all tested aggregates, including (1) a *purely elastic stage* in which the load shows nearly a linear relationship with the increasing deformation within very small deformation ranges (i.e., $d < \sim 0.01$ mm); (2) followed by a slight decrease of the load P that marks the onset of *elastic-plastic stage* characterized by a reduction of load resistance due to microstructural collapse primarily attributed to local buckling and yielding; and (3) finally, a deformation hardening pattern manifesting increasing rate of load resistance to deformation which is primarily due to densification effects caused by the intensive interactions of EDL between the clay particles, suggesting fully plastic deformation. Such distinct deformation features demonstrate that the clay aggregate is intrinsically a cellular material with a multiscale, heterogeneous microstructure of clay aggregates that involves complex porous distributions, similar to the metallic hollow sphere (Song et al. 2017). Another interesting finding is the distinct variation of local deformation features among the three tested minerals. While the load-deformation curves of IMt-1 and SWy-2 (Figure 5.2b,c) aggregates manifest continuous, smooth load- deformation response, the kaolinite exhibits characteristic fluctuations in load response, suggesting a brittle behavior that is characteristic of localized slip mechanisms within the aggregate. This can also be seen from the representative optical images of the three tested minerals, i.e., significant cracks and openings are progressively formed across the surface of KGa-1b aggregates, while no similar phenomenon exists in the other two aggregates. A simple explanation for such apparent discrepancy follows. As a well-crystallized mineral with low defect occurring in the isomorphous substitution, the relatively lower surface charge (-0.06 e per unit) of KGa-1b significantly reduces the thickness of the EDL compared to IMt-1 and SWy-2 (when dispersed in an aqueous environment), and thus, there exists much more extensive mechanical contact between KGa-1b particles, Figure 5.2d to f demonstrate the process of extracting the mechanical properties (E, τ) using the Hertzian elastic contact theory. By replotting the load-deformation curves in Figure 5.2a to c with $3P/D^{0.5}$ and $d^{1.5}$ as the two axes, E_r of the tested aggregates can be determined from the initial linear slope (i.e., elastic contact line) of the replotted curves beyond which the *elastic-plastic stage* is reached, as marked by the significant deviation of data point from the normalized elastic contact line (the slope of all normalized elastic contact lines is equal to 1, which is calculated by dividing the $3P/(D^{0.5}d^{1.5})$ by the extracted E_r in the insets of Figure 5.2d to f. E and τ of each aggregate can then be calculated with Eq. (5.2) to (5.4), as summarized in the corresponding insets, quantitatively indicating that the tested KGa-1b aggregates possess much higher E and τ than that of IMt-1 and SWy-2.

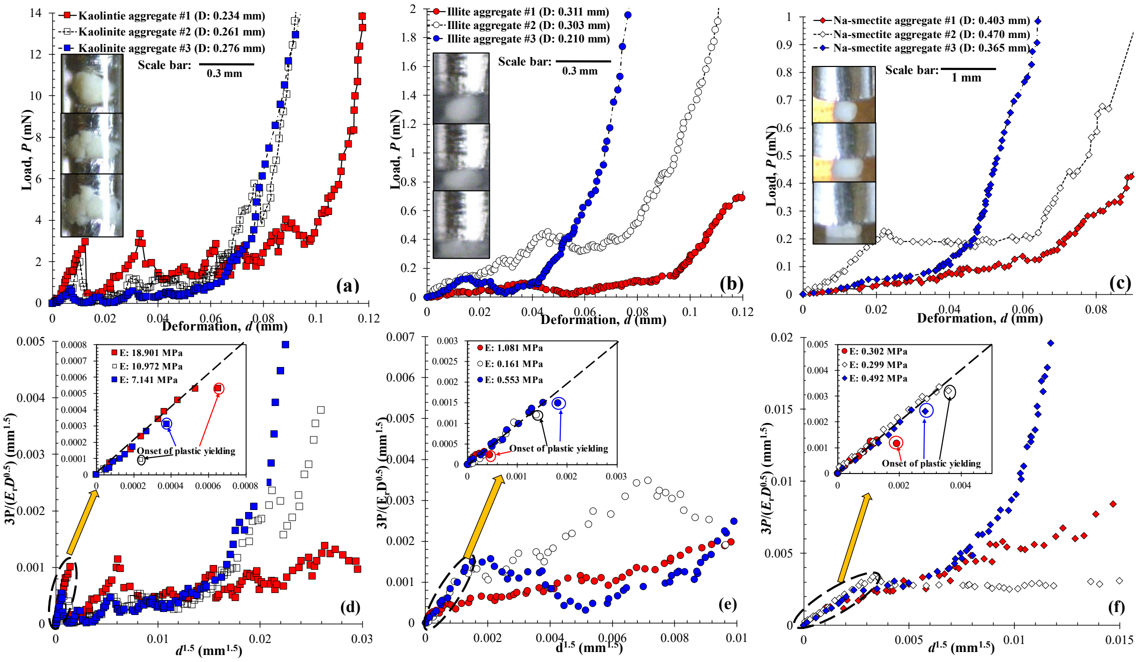

Figure 5.2 typical load-deformation curves of KGa-1b, IMt-1, and SWy-2 aggregates (a to c) and their corresponding Hertzian elastic contact curves (d to f)

5.3.2 Statistical analyses

With the data analytics above, E and τ of all tested aggregates at five ionic salinities are derived from the pertinent *P-d* curves and summarized in Figure 5.3 against the corresponding D. It is shown that, while there exists a generally decreasing trend of E and τ with D for all aggregates, highly data scattering is discerned even for aggregates at the same ionic strength (i.e., the values of both properties can be same for some aggregates with diverse D). The formation of clay aggregates involves extensive interactions between suspended particles possessing active surface properties, leading to a complex microstructure associated with random microfabric depending upon the water chemistry, which in turn increases the measurement variability due to the generation of flaws/defects across the aggregates. Prior studies have also demonstrated the similar data scattering of cohesionless granules (e.g., quartz sand, glassy sphere, coal particle) using Hertzian elastic theory (Dong et al. 2018; Liu et al. 2021; Portnikov and Kalman 2014). Although these granules possess a relatively simpler microstructure and more uniform mineral composition in comparison with clay aggregates, there still exist a certain amount of randomly-occurring crystal defects (e.g., dislocations, joints) in these particles that essentially dictate the scattered results, which is further affected by the size of tested particles that usually varies.

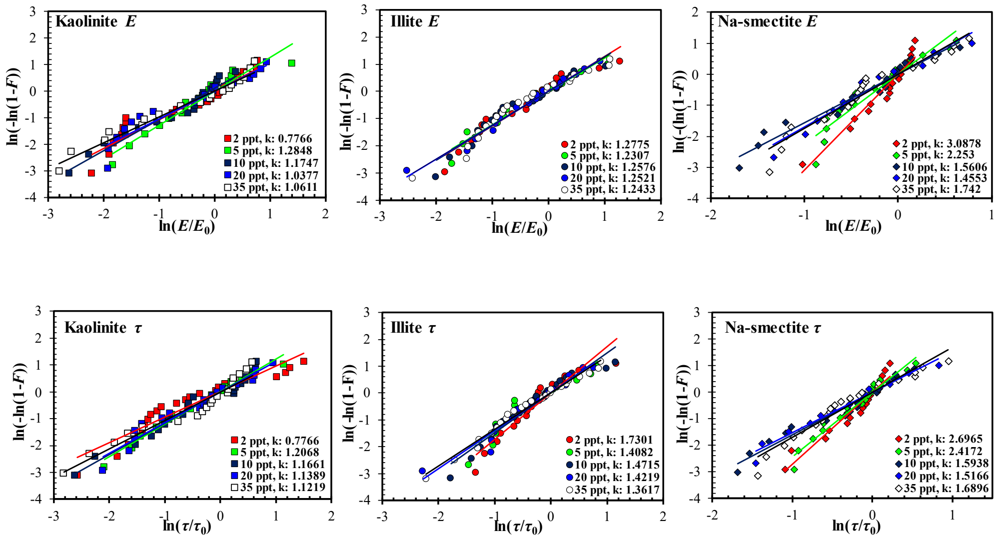

Figure 5.3 E and τ of all tested aggregates at five salinities

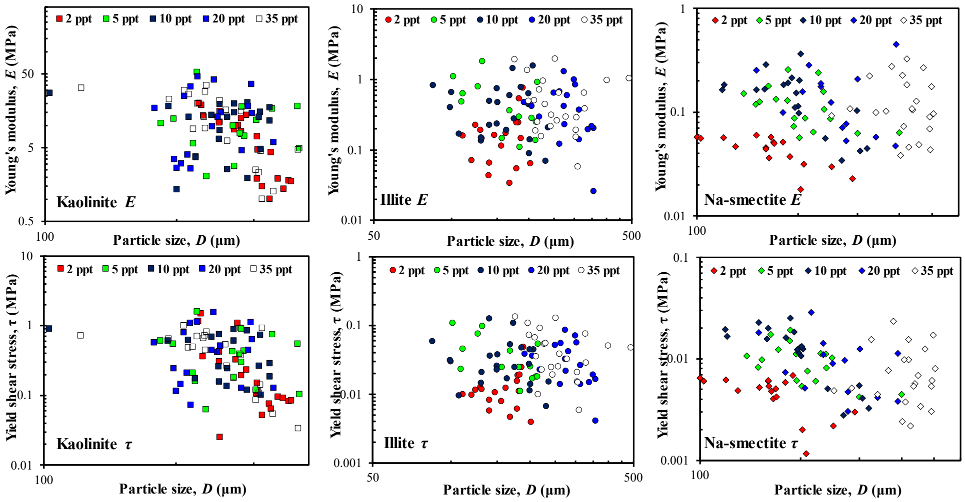

Figure 5.4 Weibull distribution of the E and τ for tested clay aggregates at each salinity

To statistically summarize and interpret the highly scattered results of tested aggregates, the extracted E and τ were processed following Weibull theory (Eq. (5.5) to (5.9)) that aims to account for the scattered properties of materials caused by the defects.

Figure 5.4 depicts the Weibull distribution of the E and τ for tested clay aggregates at each salinity. All measured data can be fitted well with the straight line described by Eq. (5.6), and all fitting lines, due to the normalization effects of nominal value (i.e., E_0, τ_0), intersect at the origin point that corresponds to a failure probability of 63.2% based on Weibull theory. The slope of all fitting straight lines (i.e., k values) can then be extracted for calculating the expected mean values of the measured E and τ.

5.3.3 Effects of porewater chemistry

Figure 5.5 presents the statistical mean values of E and τ, as well as the corresponding k values (derived from the calculation of expected mean values of E and τ) obtained from the aggregates at each salinity, respectively. Of the three tested minerals, KGa-1b aggregates possess the highest expected mean values of E and τ, which are much higher than that of IMt-1, followed by SWy-2 aggregates. As stated earlier, direct mechanical contact plays a dominant role in the particle interactions of KGa-1b aggregates, which renders them to exhibit much higher resistance under external loading. On the contrary, the relatively higher SSA and layer charge of IMt-1 and SWy-2 cause them to form aggregates of which the particle interactions are mainly controlled by the surface electrical forces in the saltwater, and thus, much weaker resistance is demonstrated from the results of microcompression testing. These differences in mechanical properties can also be explained by the well-established fact that the nano-scale interlayer bonding varies with each tested mineral: kaolintie particle is a 1:1 structured particle formed via the repetition of tetrahedron-octahedron (TO) layers linked by hydrogen bond, whose bonding energy is much higher than that of the IMt-1 and SWy-2 as 2:1 structured particles that are formed via the stacking and combination of TOT layers bonded with the electrostatic attraction (i.e., specifically referring to the poorly hydrated potassium cations between the adjacent IMt-1 layers), fully hydrated cations (i.e., specifically for the SWy-2 layers), and van der Waals forces.

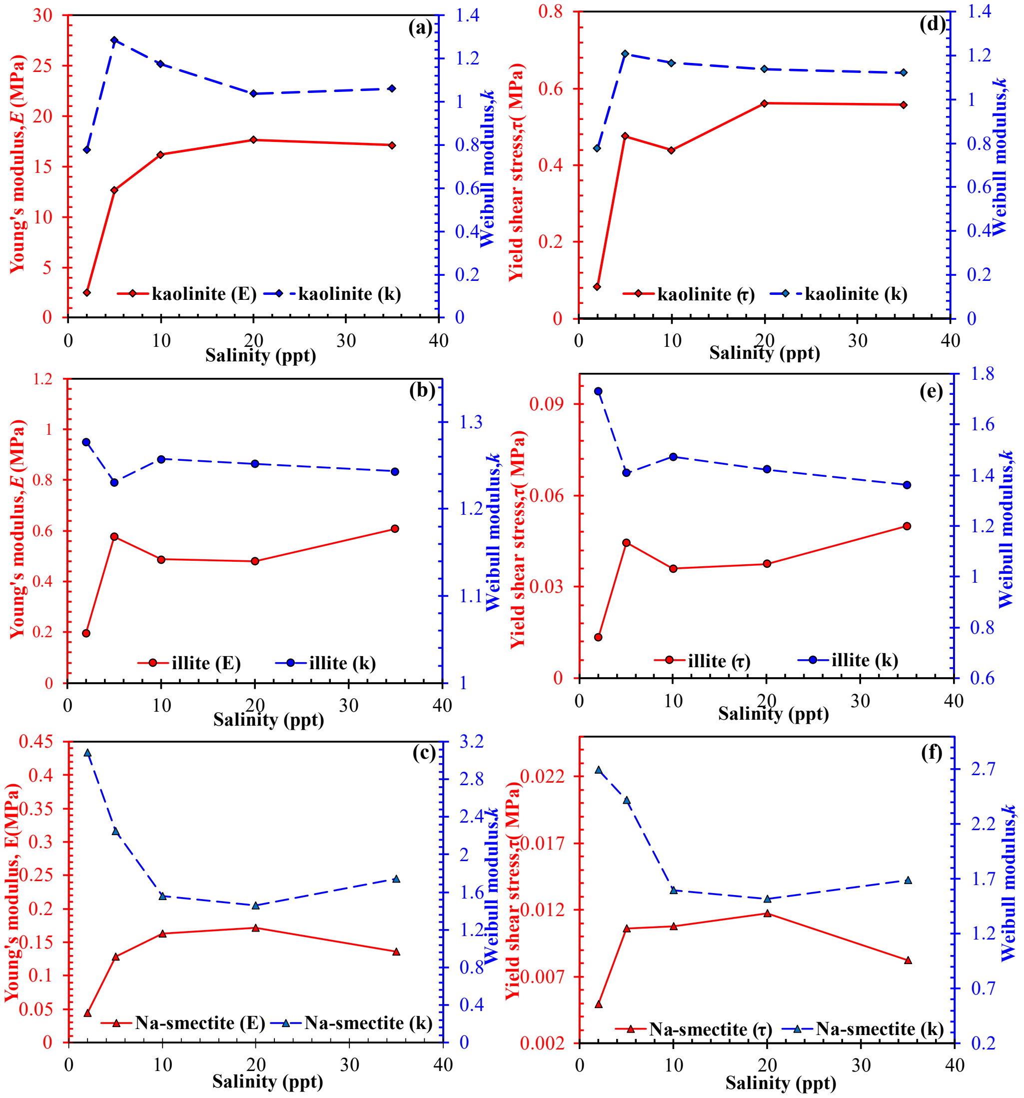

Figure 5.5 Statistical mean values of *E*: (a) to (c) and *τ*: (d) to (f) and corresponding Weibull modulus versus salinity for the aggregates of three tested minerals

With the increasing porewater ionic strength, aggregates of the three tested minerals exhibit similar increasing patterns in the derived mechanical properties, i.e., statistical mean values of E and τ of each mineral gradually increase with the porewater ionic strength and reach their respective highest values at 20 or 35 ppt. Like other colloidal particles dispersed in liquids (i.e., sol-gel materials), the formation of clay aggregates essentially reflects the destabilization of clay dispersion which is primarily dedicated by the interactions of the dispersed particles possessing active surface properties. The attraction forces between dispersed particles tend to prevail over the repulsive ones (imparted by the EDL of clay minerals) with the increasing ionic strength, promoting the formation of stronger aggregates. The largest change occurs in the range 2 to 5 ppt. While these phenomena are reasonable for IMt-1 and SWy-2 with a much higher surface charge, it is interesting to note that KGa-1b can also exhibit similar gain stiffness and yield strength in the range of salinity. Despite the very low layer charge of KGa-1b that renders the formation of much thinner EDL than that of IMt-1 and SWy-2, when dispersed in a water environment without salt addition or at very low ionic strength (e.g., 2 ppt), limited repulsive forces can still exist between KGa-1b particles. Hence, when such limited repulsion is overcome by increasing the ionic strength, the entire surface of KGa-1b is exposed to the particle interaction that can induce intensive body friction when KGa-1b aggregate is being compressed, yielding higher E and τ.

The derived k also shows interesting patterns with salinity. As a descriptor originally proposed to quantify the variability of the measured material properties, the value of k essentially represents a measure of uniformity in the material behavior that is dictated by the distribution of structural flaws (Jayatilaka and Trustrum 1977). A higher k

values indicates that the material behaves more uniformly and thus the measured properties are less scattered, due to the consistent distribution of structural flaws; while higher variability in material properties is caused by flaws that are randomly distributed within each measured material, leading to a lower *k*. For KGa-1b aggregates, the value of *k* sharply increases for salinity in the range 2 to 5 ppt, and then a constant is gradually reached as ionic strength increases. Based upon the aforementioned theory, such increment can reflect that the microfabric of KGa-1b aggregate gradually evolves into a more uniform structure with the increasing ionic strength, which can be caused by the formation of FF associated particle assemblage that involves the dense packing of KGa-1b particles exclusively along the vertical direction (aligning with the compressive loading), as schematically illustrated in Figure 5.6a.

However, the opposite trend of *k* is observed for IMt-1 and SWy-2 aggregates, which most likely is affected by the pH or acidity of aquatic environments. Clay minerals are known to possess both permanent negative charges on the particle surface and pH-dependent charges on the edge surface which exhibit amphoteric properties by protonation (i.e., adsorption of H^+) and deprotonation (i.e., loss of H^+) reactions depending upon the pH of aquatic environments (Delhorme et al. 2010). As pH reduces below a critical value, PZC_{edge} (Sposito et al. 1999; Tombácz and Szekeres 2004), the charge of the edge surface behaves positive such that the flocculation of clay minerals occurs due to the attraction between the dissimilarly-charged edge, and surface of the clay particles. Under this condition, the main microfabric of resulting aggregates is EF associated particle assemblage, which, compared with FF-dominated aggregates, significantly increases the measurement variability (i.e., decreasing *k*) of mechanical properties obtained from each aggregate, due to the formation of much more random particle arrangement that stems from the high aspect ratio of clay minerals (i.e., the basal surface has much higher area than that of the edge surface), which provides the edge surface of one particle with diverse contact points distributed on the basal surface of another one (i.e., the classic card-house microfabric), as schematically illustrated in Figure 5.6b.

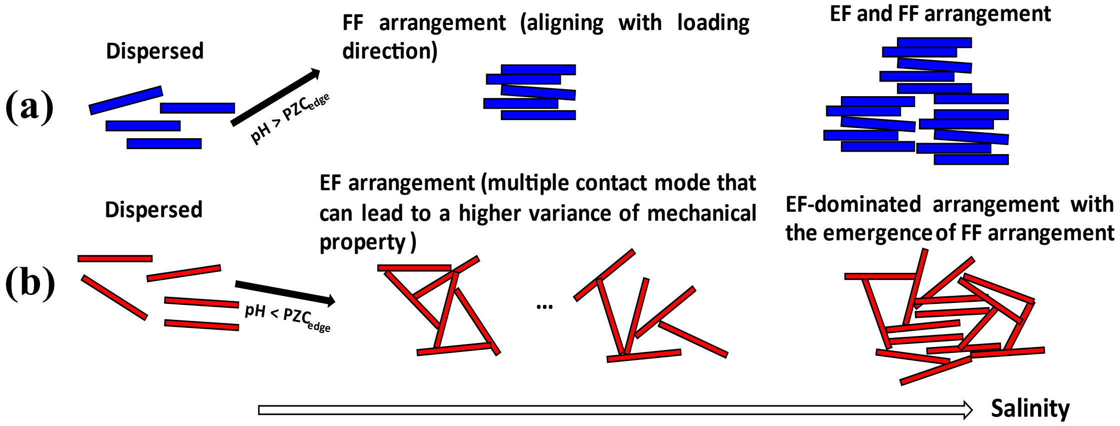

Figure 5.6 Effects of microfabric on the measurement of aggregate's mechanical properties under different water chemistry

For the determination of PZC_{edge} of these three minerals, prior works have yielded reference data for KGa-1b, IMt-1, and SWy-2, whose PZC_{edge} is in the range of 3.5 to 4 (Au et al. 2015; Kumar et al. 2017; Tombácz and Szekeres 2006), 3 to 3.5 (Lan et al. 2007; Shao et al. 2019), and 6 to 6.5 (Tombácz and Szekeres 2004), respectively. Hence, with the data of pH for KGa-1b (pH 5.97) and SWy-2 (pH 6.44) summarized in Table 4.1, and pH 2.25 particularly used for the preparation of illite aggregates, the inference for the dominant type of microfabric within these aggregates can be validated.

5.3.4 Comparison with previous data

Owing to their small size and extremely soft consistency, few studies have been reported to systematically study the mechanics and microfabric evolution of clay aggregates affected by various factors, such as mineralogical compositions, ionic strength, and pH of aquatic environments. Thus, a direct comparison of data considering all these factors is not feasible in the present study. Fortunately, there still exists limited data on the KGa-1b aggregates reported by a novel study Zhang et al. 2013a) that introduced microcompression testing (which provided an exemplary methodology for the present study) to investigate the thixotropic behavior of saltwater KGa-1b aggregates (10 ppt salinity) aging for various durations. It shows that the expected mean value of E obtained from the aging duration at 0 days (which is 15.98 MPa when Poisson's ratio of KGa-1b aggregate is assumed to be 0.03) is very close to our study (16.21 MPa), while a large discrepancy for the expected mean value of τ exists between each study (i.e., 0.23 MPa is obtained at 0 day, which is smaller than 0.44 MPa in our study). One possible reason for this discrepancy can be due to the difference in the size and shape of aggregates between each study, whose effects on the derivation of elasticity and yielding strength have been demonstrated in previous findings (Liu et al. 2021; Nakata et al. 2001; Qian et al. 2019). The yielding strength of a particle is significantly affected by the variation of size and irregular shape of particles that affects the crystal flaws within the particle and interpretation of local contact behavior, respectively. The elasticity of particle, on the other hand, is determined by the type and distribution of atomic bonds but not so much by the effects from the particle size and shape, which thus accounts for the consistency of derived E between each study.

Also, based on the results from the thixotropy study (Zhang et al. 2013a), it is noteworthy that the corresponding *k* values for both mechanical properties show an increasing trend with the aging durations, which can be well fitted by a stretched exponential thixotropy model. This finding indicates the formation of a more uniform microstructure of KGa-1b aggregates with aging, which is in agreement with the results obtained in the present study, regardless of the different environmental variables used (i.e., ionic strength versus aging time). While it is still ambiguous about whether FF-associated particle assemblage is the main type of microfabric that can reflect such uniformity (and also whether the EF-associated one increases the randomness of microfabric), a most recent study that employs one-dimension X-ray diffraction to probe the microfabric evolution of soft clay during thixotropy can provide insights into this issue (Peng et al. 2022). Orientation index (OI) (Brindley and Kurtossy 1961; Zhang et al. 2003), a ratio of the intensity of a suitable basal reflection to that of non-basal prism reflection, was used in this study for the interpretation of the microscopic changes. The results showed that, when aggregates consisting of FF-associated clay particles are formed, OI increases due to the preferred particle orientation along with the [001] lattice directions; on the other hand, flocculated microfabric associated with EF mode can decrease the value of OI due to the formation of more random particle arrangement, which thus indirectly validates the inference on the effects of ionic strength and pH on the microfabric evolution of clay aggregates.

5.4 Conclusions

This chapter presents a systematic experimental study to investigate the mechanics and microfabric of mesoscale clay aggregates prepared with different mineralogical compositions and salinities. By employing a newly developed measurement system with high sensitivity, the load and displacement of individual clay aggregates subject to compression are precisely recorded for further data interpretation. Based upon the above results and discussion, the following conclusions can be drawn:

- The contrasting deformation behavior of KGa-1b to that of the IMt-1 and SWy-2 aggregates results from the difference of layer charge, an inherent property of clay minerals that determines the dominant type of interparticle interactions.
- Young's modulus and yield shear strength of individual clay aggregates were derived using Hertz elastic contact theory. It shows that Young's modulus of the KGa-1b aggregates (in an order of several MPa) is much higher than that of the SWy-2 aggregates (in an order of several hundred kPa), and Young's modulus of the IMt-1 aggregates ranges in between. Same trends were also found for their yield shear strengths.
- With Weibull statistical analysis, the expected mean values of Young's modulus and yield shear strength at all salinities are derived for aggregates of the three tested minerals. It shows that higher Young's modulus and yield shear strength are promoted with increasing salinity, primarily due to the suppression of the electrical double layer on clay surfaces with the increasing ionic strength induced by the monovalent salt.

- With increasing salinity, the Weibull modulus of KGa-1b aggregates exhibits an increasing trend, indicating a more uniform microstructure is formed associated with face-to-face microfabric. The opposite trend, however, is found for IMt-1 and SWy-2 aggregates, which is essentially caused by the formation of edge-to-face microfabric that increases the non-uniformity of aggregate's microstructure, when the pH of the aquatic environment is below the point of zero charge of IMt-1 and SWy-2 edge surface.

Acknowledgements

This work was supported by the U.S. National Science Foundation (NSF) under Award No. CMMI 1702881. The first author also received partial support from the Charles F. Perrell Scholarship. Any opinions, findings, and conclusions expressed in this paper are those of the authors and do not necessarily reflect the views of the NSF.

CHAPTER 6

ELASTIC BEHAVIOR OF LIGHT-INDUCED STATICALLY CULTIVATED OXYGENIC PHOTOGRANULE

This paper presents an experimental study concerning the elastic behavior of light-induced oxygenic granules (OPGs) statically cultivated at different periods (March and June). Quasi-static uniaxial compression testing was employed on the OPGs to plot the load-deformation curves, which exhibit different deformation features for each group of OPGs. To quantify the elastic behaviors of OPGs being tested, Hertz elastic contact theory was used to derive the mechanical properties, including reduced modulus, Young's modulus, and yield shear stress, which were then interpreted with Weibull distribution to derive the expected mean value of derived Young's modulus and yield shear stress. Also, Weibull modulus, a useful structural descriptor proposed in Weibull statistical analysis, was used to help characterize the internal structure that significantly affect the mechanical properties of OPGs.

6.1 Introduction

Oxygenic photogranules (OPGs), first found by Park and Dolan (2015) who incubated activated sludge in unagitated and sealed vials subject to stimuli of natural light for several months, have recently gained growing interests from environmental and bioengineering field as a cost-effective alternative in wastewater treatment compared with the conventional, energy-intensive activated sludge process (consuming upwards of 8 billion kilowatt hours of electricity each year) (Alto 2013) that has to provide a constant supply of oxygen to support contaminant removal by the microorganisms in the activated sludge. Essentially, OPGs can be considered as a group of biofilms due to the characteristic formation mechanisms. That is, a group of bacteria from the activated sludge interact intensively with various types of stimuli (e.g., organic matters, light, oxygens, shear stress), leading to the formation of a complex assemblage of bacteria closely intertwined with the three-dimensional extracellular polymeric substances (EPS) which primarily serves as the matrix maintaining biofilm's structural integrity (Boudarel et al. 2018). Over the past decades, the microbiology community has conducted extensive research on biofilms in different aspects. Among these research interests, biofilm mechanics has emerged as an interdisciplinary research, has emerged as a popular topic to response of biofilms under different loading conditions (e.g., compressive, tensile, shear stresses) that are real-world situations, and then, develop reliable and efficient strategies for biofilm-based processes (e.g., bioremediation, nanomaterials synthesis, antimicrobial screening) as well as advance our understanding of biofilm life-cycle (formation mechanism affected by environment stimuli). A wide range of methods have been used to characterize mechanical properties of biofilms for measuring relevant mechanical parameters. One of the most widely reported techniques, static rheology test, is used to study the time-dependent behavior of biofilms, including creep recovery test (Ferry 1980; Towler et al. 2003) and stress relaxation test (Peterson et al. 2013) that measures the deformation of biofilms over time at a constant applied stress and that records the stress as a function of time after imposing a specified level of straining. The recorded data can then be fitted with some classical rheological models (spring-dashpot element arrangement) such as the Kelvin-Voigt model (Abe et al. 2011), Burgers model (Findley et al. 1977; Vinogradov et al. 2004) or the generalized Maxwell model (He et al. 2013), to derive the apparent elastic modulus (E_i) and apparent viscosity (η_i) of biofilms. Another noteworthy technique is the uniaxial compression test, which has been widely applied for the identification of mechanical properties of typical engineering materials (e.g., steel, concrete, soil), involving a process during which the tested sample is vertically compressed between two rigid plates/rods (usually the upper one moves downward while the lower one being stable) at a constant loading rate, hence leading to the determination of elastic properties including Young’s modulus (apparent elastic modulus) (E) and yield stress (τ) through the stress-strain curves of the tested sample. In particular, these properties can only be determined at small strains where recoverable elastic response is explained. One prominent advantage of the uniaxial compression test is the simplicity that enables testing operators to easily develop methods suitable for the biofilms of interest, i.e., mounting a miniature load cell (recording load in the order of millinewtons) to the loading system for measuring small stress that the weak and porous biofilms can withstand (Körstgens *et al.* 2001a, 2001b; Paramonova *et al.* 2009a, 2009b; Safari *et al.* 2015). The shear rheometric test and uniaxial compression test can both be classified as types of bulk parameter testing, which characterizes the macroscopic mechanical properties of biofilms treated as homogenous materials. However, biofilms are three-dimensional structures that compose of EPS matrix crossed by pores that irregularly segment the embedded bacteria into different micro/nano colonies. Hence, biofilms exhibit heterogeneities in their mechanical properties that vary over different length scales (from nano-, to micro-, and macro-scales). Based on this fact, various types of techniques/methods have been employed to perform tests on the biofilms that consider heterogeneities over different scales, such as microindentation (Chen et al. 2005a), micropipette (Poppele and Hozalski 2003), atomic force microscopy (AFM) (Ahimou et al. 2007), and magnetic tweezers (Galy et al. 2012).

Despite the diversities of testing types and derived mechanical parameters, the prior research has concluded tthat biofilms are viscoelastic materials which, depending on the applied loading/unloading rate during deformation (strain-rate dependence on time), both exhibit elastic and viscous behaviors by recovering their original length (storing energy) and will yield and flow like a viscous liquid (dissipating energy) when the yield stress is exceeded (Peterson et al. 2015). This consistent standpoint provides a framework for further studies on the biofilms with which they can be conducted surrounding the feature associated with viscoelasticity. For example, in the context of OPGs applied in wastewater treatment, nonuniform hydrodynamic conditions are expected to exert shearing stresses on the surface of OPGs that are formed in the reactor, which subjects the OPGs to varying degrees of deformation, resulting in disturbance of the internal structure. Knowing the elastic properties of the OPGs in advance can help characterize the mechanical behaviors at small deformations, which in turn offers baseline parameters (elastic moduli in the viscoelastic models) for subsequent works to which they can refer for controlling the process of wastewater treatment. Also, owing to the gravitational effects, OPGs will settle to the bottom of reactor after they treat or consume polluted materials, eventually making up a load-bearing bed of OPGs clustering on the bottom. Careful considerations are then necessary in investigating the behavior of OPGs over time to understand the long-term stabilities of OPGs, such as consolidation settlement (deformation of OPGs with the continuously external loading), creep settlement (deformation of OPGs when external loading is constant), and stress relaxation (stress variation of OPGs during the detachment from the bottom bed). These studies are all closely correlated with the viscoelastic behaviors which can be investigated by the techniques/methods.

In summary, the mechanical properties of OPGs are of key importance for understanding their performance in the process wastewater treatment, and there are many techniques/methods available for applying to characterize the mechanical properties of OPGs. This paper aims to evaluate the elastic behavior of OPGs via uniaxial compression testing that can be employed for measuring the macroscopic mechanical properties of biofilms. Two groups of statically cultivated OPGs collected from different cultivation periods (March and June) were chosen as the studied materials for the experimental measurements. It is expected that such a study can provide subsequent researchers and field engineers with accurate measurements of OPGs' elastic properties and valuable information concerning the mechanical responses of OPGs during compression loading.

6.2 Materials and methods

6.2.1 Materials

Ten and twelve samples of statically grown OPGs were collected from March and June cultivation groups for compression testing, respectively. Due to the geometry of tested OPGs that are not ideally spherical, nominal diameter D_0 was employed instead to quantify the size of OPGs. To measure the nominal diameter, Vernier caliper was first used to measure the maximum length, diagonal length and minimum length of bottom surface of OPGs, and then, with these lengths, the average length of bottom surface for each sample can be calculated, which in turn leads to the cross-sectional area of the sample A_0 by assuming the bottom surface is circular. To finalize the determination of nominal diameter for these OPGs samples, Eq. (6.1) proposed by (Körstgens *et al.* 2001a) was used:□

$$D_0 = \frac{m_0}{\rho_0 A_0} \tag{6.1}$$

Where m_0 is the mass of each sample, and ρ_0 is the mean density of OPGs samples, which was measured as 1.147×10^{-3} g/cm^3 based on the assumption that the statically grown OPGs are homogeneous materials. The nominal diameters of all tested OPGs along with their cross-sectional areas and mass were summarized in Table 6.1.

6.2.2 Compression testing of individual OPGs

Each collected sample was carefully picked up from their respective scintillation vials using a soft tweezer, which was rinsed with 10% ethanol solution after each collection for eliminating potential contaminations. A smooth and clean glass slide was then prepared to serve as a substrate for supporting the selected OPGs. In consideration of the soft and weak nature of biofilms, a miniature load cell (Load Cell Central, Inc., Milan, PA) with a maximum load capacity of 50 milligrams (490 mN) and a load resolution of as small as 0.02 mN was mounted onto the GeoJac loading frame (Trautwein Soil Testing Equipment, Inc., USA) placed in the acrylic glass enclosure, which can help prevent the air and dust flows (Figure 6.1). In particular, to satisfy the condition of diametrical compression (granule being compressed between two flat punch), a polished glass sheet with dimensions of 8 ×5×0.5 mm was smoothly cut from the same type of the substrate, which was firstly glued with an aluminum load button using hot melt glue, and then attached to the miniature load cell to serve as the upper flat punch (Figure 1c). The entire process of compression was controlled by the GeoJac loading frame to perform vertically quasi-static loading and unloading loop on the OPGs at a constant displacement rate of 0.05 mm/min. Noteworthy is that the maximum vertical load applied on each sample is in the range of 285 to 490 kPa, which in fact has no impact on the results of our current study, since the process of failure or breakage is generally not considered in the uniaxial compression testing on biofilms. To observe the deformation process of OPGs, the high-resolution microscope installed next to the GeoJac loading frame was used to capture multi-time images of the OPGs along with the microscale structural change at an assigned area, as shown in Figure 6.2. Finally, after removing the environmental effects that lead to the confusion of data recording (deformation of load cell, negative surface tensions), the real load on OPGs versus deformation of OPGs curves were generated for each OPGs samples being compressed.

Table 6.1 Summary of the mass and size for OPGs of two groups

March group			
Label of OPGs	Mass, m (g)	Cross-sectional area, A_0(mm^2)	Nominal diameter, D_0 (mm)
#1	2.01	279.08	6.30
#2	3.14	447.14	6.14
#3	1.32	227.80	5.05
#4	2.91	426.58	5.95
#5	1.27	272.95	4.05
#6	0.18	26.04	5.87
#7	0.85	94.98	7.81
#8	0.81	72.94	9.64
#9	0.80	80.19	8.66
#10	0.73	91.37	6.99

June group			
Label of OPGs	Mass, m (g)	Cross-sectional area, A_0 (mm^2)	Nominal diameter, D_0 (mm)
#1	3.17	340.50	8.11
#2	3.31	349.64	8.25
#3	2.78	466.37	5.19
#4	2.48	408.26	5.29
#5	1.03	176.68	5.09
#6	1.14	115.12	8.61
#7	1.94	176.62	9.56
#8	0.52	94.34	8.32
#9	0.98	90.01	9.47
#10	0.46	54.46	7.38
#11	0.72	66.97	9.39
#12	1.38	110.01	10.91

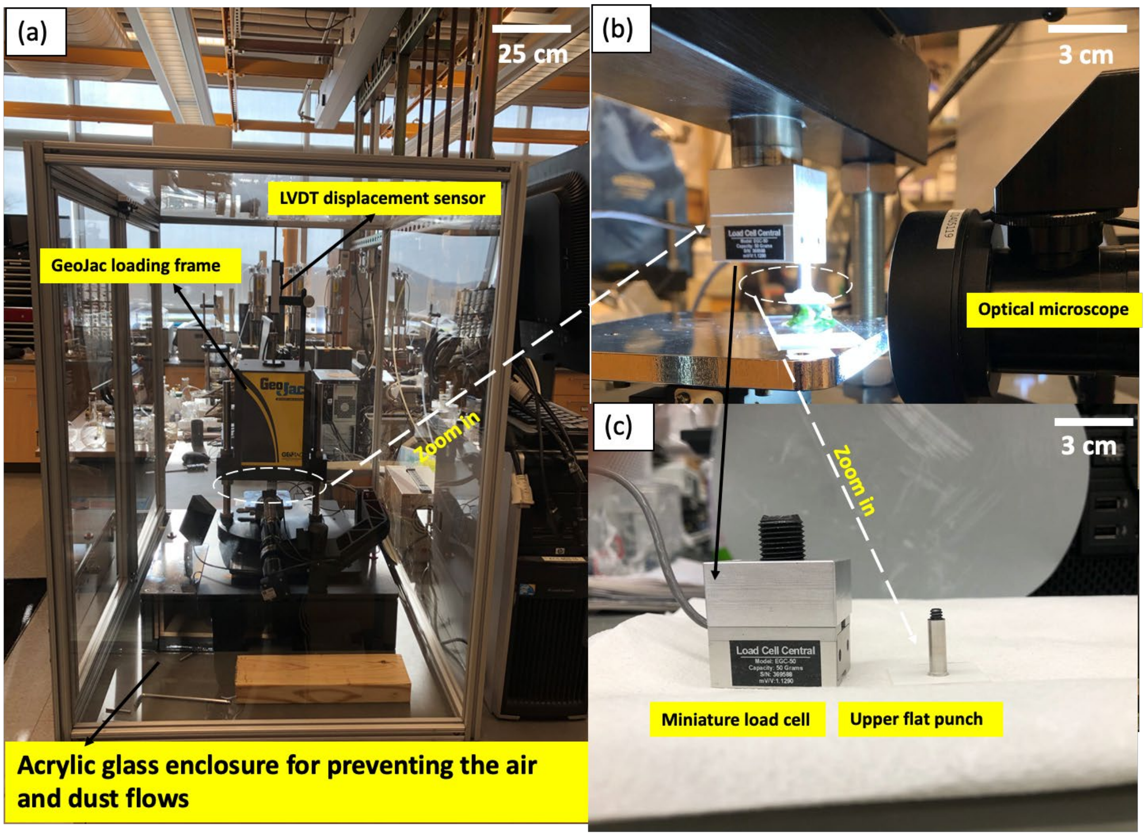

Figure 6.1 Experimental set up for the compression testing of individual OPGs: (a) the GeoJac loading frame placed in the acrylic glass encolure; (b) OPGis being compressed under the observation of an optical microscope; (c) close-ups of miniacture load cell and the upper flat punch that compress the individual OPGs

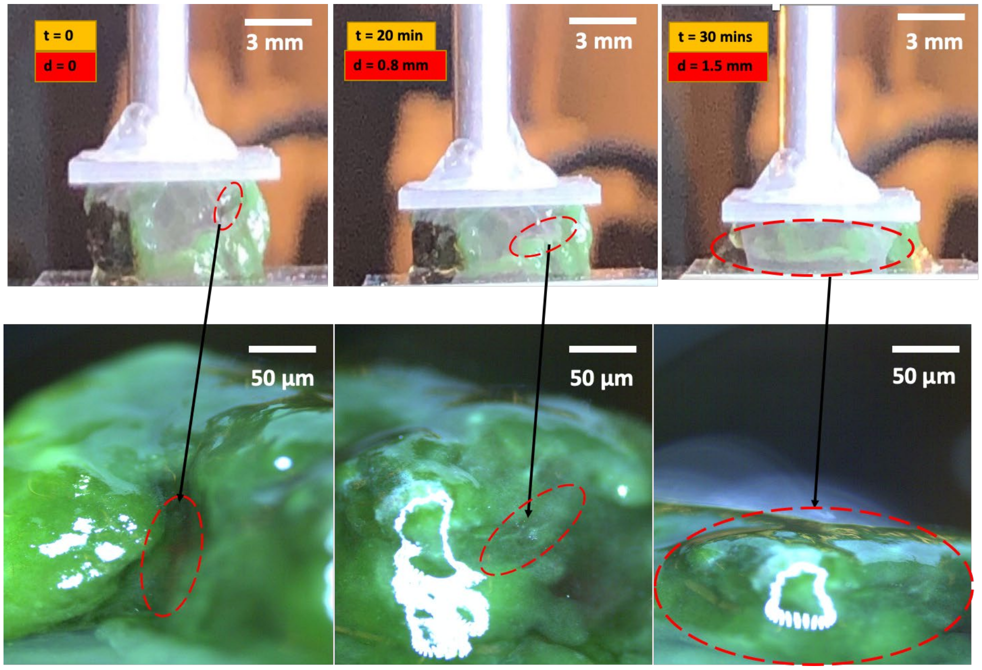

Figure 6.2 Real-time images of the OPG deformation details (the lower images show the pore densification at microscale during compression)

6.2.3 Hertz elastic contact theory

Hertz elastic contact theory (Johnson 1985), an analytical solution to the contact problem between the elastic sphere and rigid plates, was used for analyzing the load versus deformation curves of tested OPGs. By considering a smooth and frictionless contact scenario in which the soft OPG sample is compressed between two relatively more rigid glass plate, the reduced modulus E_r measuring the stiffness of OPG-glass plates contact can be derived with the following equation (Yin 2013):

$$E_r = \frac{3P}{(D_0 d^3)^{1/2}} \tag{6.2}$$

where P is the load applied on the tested OPG in the elastic regime, D the nominal diameter of the tested OPGs, and d is the deformation of tested OPG (the sum of deformation for two OPGs' hemisphere being compressed). To determine the elastic stage beyond which the tested OPG starts yielding, the Hertz elastic contact line plotted with $3P/D_0^{1/2}$ versus $d^{3/2}$ (Eq (6.2)) is used to fit the experimental load-deformation curve, which can mark the onset of plastic yielding by locating the point where the Hertz elastic contact line deviates from the experimental load-deformation curve. This method also leads to the determination of yielding shear stress τ_y of the tested OPG, which is calculated as (Zhang *et al*. 2013):

$$\tau_y = 0.31 p_{\max} = 0.31 \left(\frac{24 P_y E_r^2}{\pi^3 D^2} \right)^{1/3} \tag{6.3}$$

where $p_{\max}$ is the maximum contact pressure in the elliptical pressure function describing the load distribution within the contact area and P_y is the applied load when yielding happens, as expressed with the following equation:

$$\left(\frac{p}{p_{\max}} \right)^2 = 1 - \left(\frac{r}{r_c} \right)^2 \tag{6.4}$$

where r_c is the radius of contact area, as calculated with the following equation:

$$r_c = \left(\frac{3PD_0}{8E^*} \right)^{1/3} \tag{6.5}$$

To calculate the Young's modulus of the tested OPG, following equation (Song et al. 2017) is used:

$$\frac{1}{E_r} = \frac{1 - v_1^2}{E_1} + \frac{1 - v_2^2}{E_2} \tag{6.6}$$

Where E_1 and E_2 are the Young's modulus of the tested OPG and glass, respectively, and υ_1 and υ_2 their corresponding Poisson's ratios. Noteworthy is that due to the relatively higher Young's modulus of glass (in the magnititude of GPa) that has been reported in previous literatures (Philipps et al. 2017; Youn & Kang 2005), Eq. (6.6) can then be converted into following equation ($E_2 >> E_1$, $E_2 \rightarrow \infty$):

$$E_1 = E_r(1 - v_1^2) \tag{6.7}$$

It is clear from Eq. (6.7) that the Poisson's ratio has little or no effect on the calculation of Young's modulus for the tested OPG, therefore a constant Poisson's ratio of 0.3 that has been assumed for general granulate materials is used in this study for all tested OPGs.

6.2.4 Statistical analysis

Owing to the complexity of internal structure and variation of size, large data scattering is expected in the determination of E and τ for all tested OPGs. As such, to accurately interpret and analyze the extracted mechanical properties (i.e., to determine the statistical mean or characteristic value of the derived mechanical properties), Weibull statistical analysis (Weibull, 1939; Weibull, 1951), an analytical method that attributes the variation of the strength data to the distribution of sizes and orientations of the structural flaws (weak links) clustering in the tested materials, is employed here to summarize the extracted mechanical properties, with following cumulative equation in which $F(\mathrm{x})$ represents the possibility of failure for individual OPG:

$$F(\mathrm{x}) = 1 - e^{-\left(\frac{x}{\lambda}\right)^k} \tag{6.8}$$

where $x > 0$ is the variable of interest (i.e., E, τ), $k>0$ is the shape parameter (or Weibull modulus for the distribution of material strength) which will be particularly discussed in later sections, and $\lambda > 0$ is the scale parameter (or nominal strength x_0) of the distribution. By conducting logarithmic arrangement for both sides, Eq (6.8) can be reformulated as:

$$\ln\left(-\ln\left(1-F(x)\right)\right)=k\ln\left(\frac{x}{\lambda}\right)=k\ln x_i+b=k\ln\frac{x}{x_0}+b \tag{6.9}$$

Eq. (6.9) depicts the regression line between ln(-ln(1-$F(x)$)) and lnx_i; however, the corresponding F_i for each independent variable x_i remains to be determined. To solve this issue, the mean rank method (Huang et al. 2014), which involves the relationship between the rank of experimental data point i and the total number of all data point n, is employed with the following equation:

$$F_i=\frac{i}{n+1} \tag{6.10}$$

With Eq. (6.10), the experimental data points can be fit with Eq. (6.9) to derive the value of k and b through the linear regression for the experimental data points, which in turn help determine the shape parameter λ with the following equation:

$$\lambda=e^{-\frac{b}{k}} \tag{6.11}$$

Finally, the statistical mean value or characteristic value of extracted mechanical properties is determined using the Gamma function:

$$E(x)=\lambda\Gamma\left(1+\frac{1}{k}\right) \tag{6.12}$$

6.3 Results and discussion

6.3.1 Qualitative description and extraction of mechanical properties

The load-deformation curves obtained from the uniaxial compression tests are shown in Figure 6.3 for the two groups of OPGs, respectively. In general, similar deformation features during each loading-unloading cycle are observed from the two groups of OPGs (upward concave curve pattern under loading and unloading), despite the different nominal diameters and granule geometry. However, the OPGs of June group show higher scattering throughout the entire process of compression (i.e., random spreading of loading-unloading curves) than that of March group, five curves of which (March #3, #4, #7, #8, #9) nearly overlap within a specific range of deformation (d: 0-3.87mm). This discrepancy may possibly be caused by the higher structural randomness (e.g., nonuniform distribution of microporosity) inside the OPGs of June group (Song et al. 2018), while preferred orientation of particles at micro/nano scale may exist within the OPGs of March group (Sjoblom 2016) that leads to the concentration of curves. Also, all curves show varying degrees of local serrations (mostly obvious in March #1 and June #6), indicating that all OPGs being tested experience structural buckling and yielding within the pores crossing the bacteria and matrix.

To quantitatively extract the mechanical properties, the loading-unloading curves in Figure 6a and b are replotted by Hertzian contact theory, with $3P/D_0^{1/2}$ and $d^{3/2}$ as the ordinate and abscissa axis, respectively. Figure 6.4 shows two example curves replotted with loading-unloading curves of OPGs from March and June groups, where the reduced modulus E_r for each OPG is determined through the linear fitting to the repotted curves, thus deriving the Young's modulus E. Table 6.2 summarizes the reduced modulus, Young's modulus and yield shear stress of OPGs from each group, which yields Young's modulus with arithmetic average of 20.71±20.29 kPa and yield shear stress of 0.66±0.57 kPa for March group, while June group has a lower Young's modulus with arithmetic average of 13.88±13.09 kPa and yield stress of 0.42±0.37 kPa (± means standard deviation). Also, due to the variation of granule size and inherently nonuniform distribution of pores, the Young's modulus and yield shear stress of OPGs from each group vary significantly with granule diameter D, that is, no strong correlation exists between the parameters and diameters (Figure 6.5). Therefore, to effectively interpret the highly scattered derived data, Weibull statistical analysis was performed for each group, as illustrated in the next section.

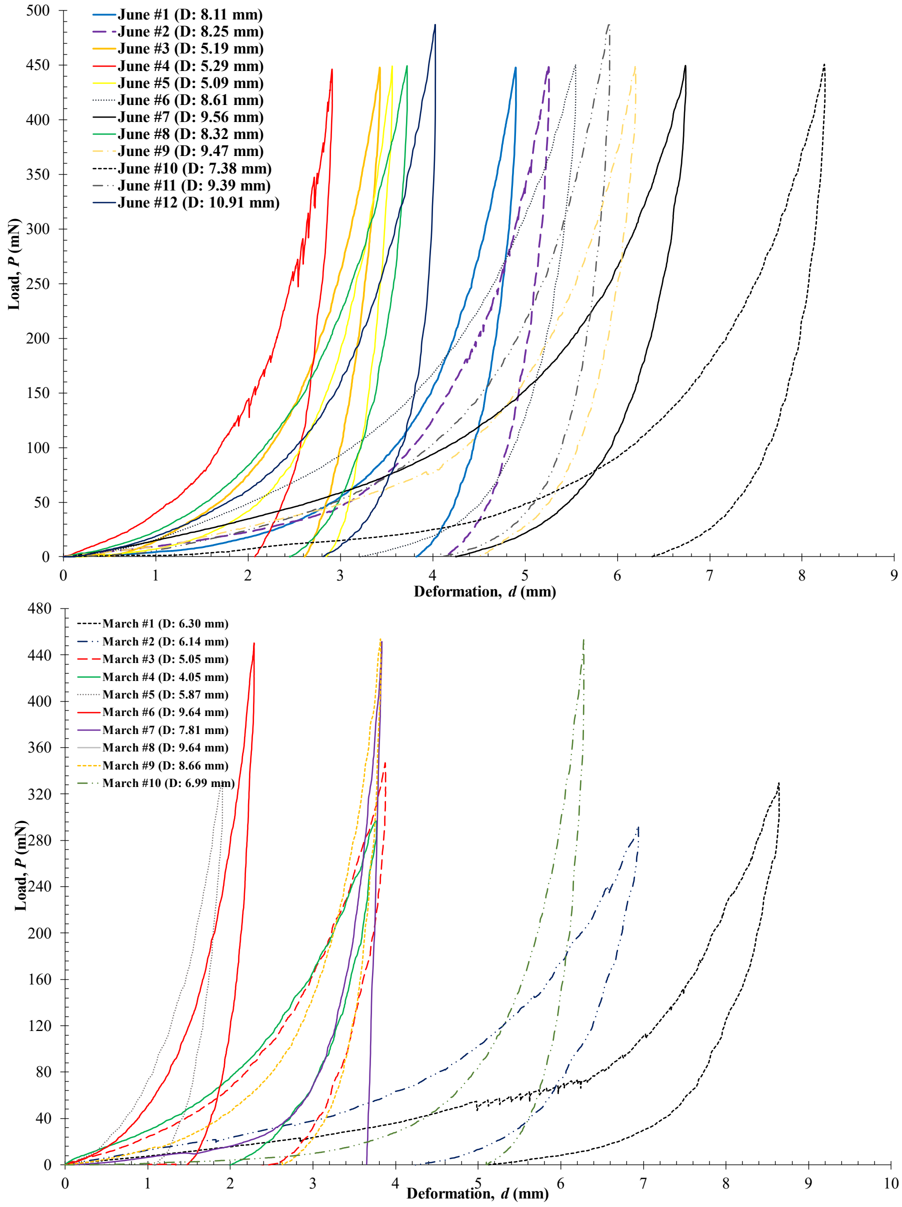

Figure 6.3 Load-deformation curves of individual OPGs from March and June group.

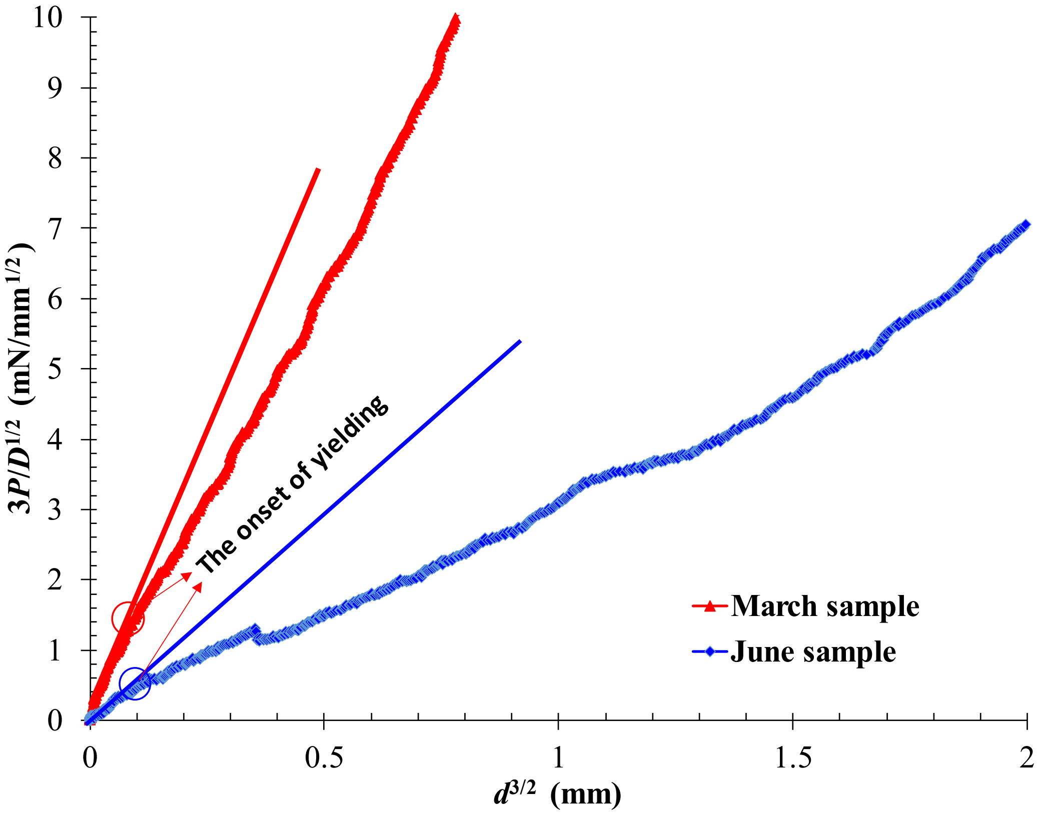

Figure 6.4 Example curve showing the application of Hertz contact line for deriving the E_r.

Table 6.2 Summary of derived mechanical properties (E*, E, τ) for OPGs of two groups

March group			
Label of OPGs	Reduced modulus, E^* (kPa)	Young’s modulus, E (kPa)	Yield shear stress, τ (kPa)
#1	7.63	6.94	0.10
#2	12.15	11.06	0.19
#3	22.01	20.06	0.99
#4	32.54	29.61	1.04
#5	25.93	23.59	0.54
#6	72.17	65.68	2.04
#7	5.76	5.24	0.18
#8	15.52	14.13	0.39
#9	13.15	11.96	0.38
#10	5.76	5.24	0.07
June group			
Label of OPGs	Reduced modulus (kPa)	Young’s modulus, E (kPa)	Yield shear stress, τ (kPa)
#1	3.00	2.73	0.10
#2	8.74	7.95	0.15
#3	4.72	4.29	0.13
#4	30.91	28.13	0.94
#5	5.80	5.28	0.30
#6	13.15	11.97	0.68
#7	21.87	19.90	0.36
#8	43.38	39.47	1.23
#9	2.98	2.71	0.11
#10	22.31	20.30	0.69
#11	8.13	7.40	0.27
#12	1.72	1.57	0.10

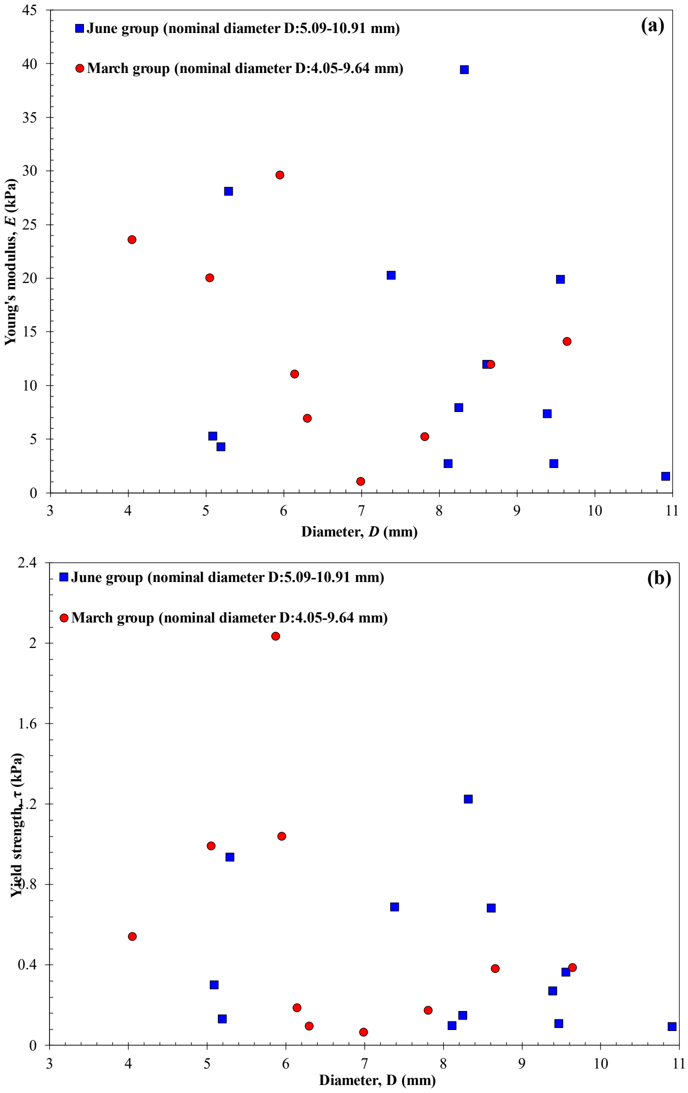

Figure 6.5 Variation of derived mechanical properties with size for each group: (a) Young's modulus; (b): yield strength

6.3.2 Weibull statistical analysis of mechanical properties

Figure 6.6 plots the Weibull distribution of extracted mechanical properties (E, τ) for OPGs from March and June group, in which the correlation coefficient R^2 and Weibull modulus k (i.e., the slope of the straight line for fitting the data) are included in the plots. Based on the regression results, the data consistency is satisfactory due to the high R^2 of each group. However, in comparison with the June group, March group has higher k values of Weibull distribution for both extracted mechanical properties, which, with Eq. (6.12), yields the expected mean value of Young's modulus E of 21.82 ± 19.76 and 15.20 ± 14.30 kPa with that of yield shear stress τ of 0.70 ± 0.58 and 0.46 ± 0.44 kPa, for OPGs of March group and June group, respectively. Apparently, there exists a possible relationship between Weibull modulus and the mechanical properties. A possible explanation for this hypothesis follows.

As stated earlier, Weibull distribution links the statistical variation of the measured material properties (e.g., E and τ in this study) with inherent structural flaws (weak links) of the tested material, which can be characterized by the Weibull modulus k. Generally, when k value is greater than 1, the material is expected to behave more uniform due to the evenly distributed flaws, thus higher strength and less scattered properties. On the contrary, higher data scattering in measured properties results from the non-uniformly distributed flaws, leading to a smaller k with value not greater than 1 (Jayatilaka & Trustrum 1977; Klein 2009). In fact, this explanation can indirectly be validated by the experimental load-deformation curves for each group (Figure 7.3), where several June samples show similarity in properties indicated by curves overlapping, while June group shows higher scattering that each curve is quite distinct from others.

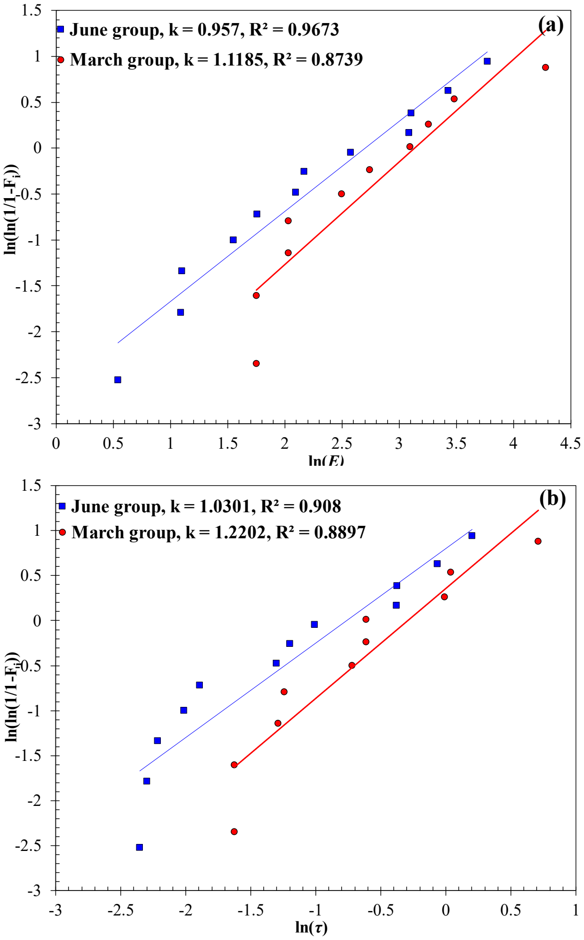

Figure 6.6 Weibull analysis of derived mechanical properties for each group: (a) Young's modulus; (b): yield strength

6.3.3 Comparison with prior studies

On the determination of elastic mechanical properties (e.g., *E*, *τ*) for biofilms by uniaxial compression testing, prior studies have reported relevant data obtained from wide variety of biofilms, as summarized in Figure 8 where each dot plotted represents the reported value of *E* and *τ*. Depending on the different biofilm types and cultivation conditions (e.g., metal ions concentration, varied shear rates, cultivation durations, temperature) applied, the extracted Young's modulus varies significantly among these studies (i.e., in the order of 0.01 to 10 kPa). While yield shear stress is as important as Young's modulus in evaluating the elastic behavior of biofilms, available data regarding the yield shear stress was only reported by Körstgens et al. (2001a, 2001b). Also, for the OPGs of March and June group, their Young's modulus and yield shear stress derived from Hertz contact theory are reported in the Figure 10 to directly compare with the previous data. Clearly, while most biofilms exhibit relatively lower Young's modulus, the P.aeruginosa (SG81) biofilms tested by Körstgens et al. (2001a, 2001b) yield higher Young's modulus ranging from 6.5 to 47.5 kPa with corresponding yield shear stress ranging from 0.9 to 1.6 kPa, which is interestingly close to our results obtained from the OPGs. The data similarity in derived elastic properties for these two types of biofilms can be most likely due to the analogous growth conditions, i.e., P.aeruginosa and OPGs biofilms were both statically cultivated (without exerting shear stress during cultivation) using bacterial strains isolated from the wastewater system (e.g., activated sludge). This specific formation mechanism distinguishes the P. aeruginosa and OPGs from other biofilms reported in Figure 6.7 which were prepared using different source strains (e.g., bacterial or fungal species or mixed-culture environmental biofilms) with applied hydrodynamic shear stress, thus inherently resulting in different values of elastic properties owing to the variation of EPS composition and biofilm architecture (Liu & Tay 2002; Purevdorj et al. 2002). Another important factor causing the data similarity could be the closeness of loading rate applied in the uniaxial compression testing for each biofilm (i.e., 1 μm/s for P.aeruginosa whereas 0.83 μm/s for OPGs). In general, for highly porous materials with tenuous and fractal structures such as biofilms and cohesive sediment (mixture of silt and clay), the applied loading rate has a significant effect on their mechanical properties by facilitating the generation of excess pore air or water pressure, which in turn makes the skeleton of materials bear effects of external loading depending on the pore sizes and magnitude of loading rates (e.g., undrained shear strength) (Schlue et al. 2010). Also, during loading, the hydrodynamic drag is developed within the porous structure, which renders viscous effects on the materials that help dissipate the strain energy (Clarke & Hird 2012). Therefore, with the aforementioned effects of loading rate, similar characteristics in resistance against external loading (e.g., E, τ) can be interpreted for P.aeruginosa and OPGs biofilms.

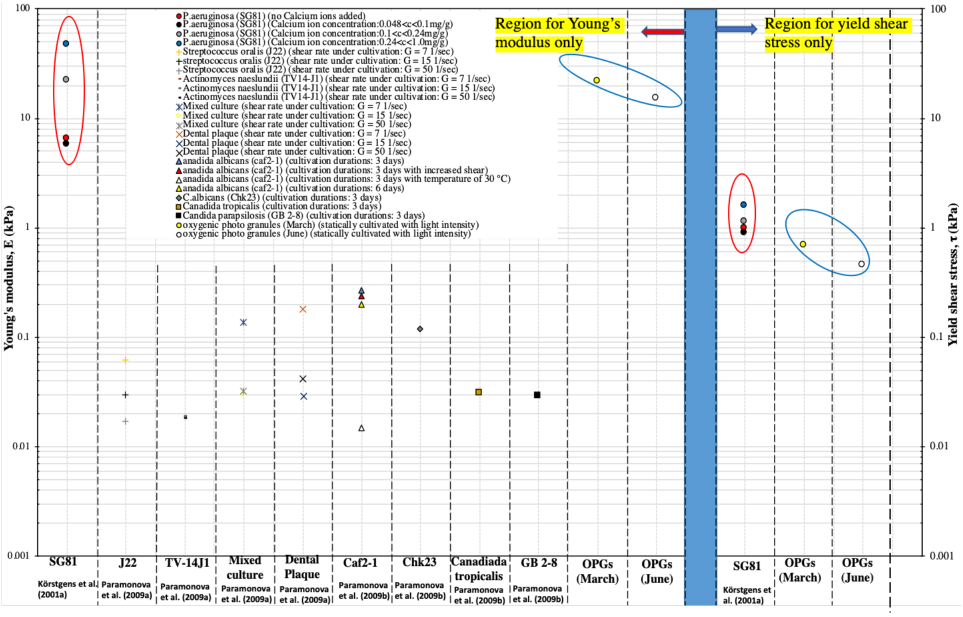

Figure 6.7 Data comparison with previous studies in terms of the mechanical properties (red circles and blue circles represent the results of P.aeruginosa and OPGs, respectively)

6.4 Conclusions

This paper presents an experimental study to evaluate the elastic behavior of individual oxygenic photogranules from two groups (March and June) that are statically cultivated with the controlled light conditions. Based on the above analysis and discussion, important conclusions can be drawn as follows:

- OPGs from March and June group exhibit different mechanical characteristics under external loading, as clearly shown in the load-deformation curves recorded through quasi-static uniaxial compression testing conducted on each OPGs sample. While curves of OPGs from June group show scattered patterns, data uniformity is demonstrated in the March group where overlapping of curves happens. This discrepancy could be explained with the Weibull modulus k, which is a structural descriptor that basically characterizes the distribution of weak links or flaws inherently clustering in the internal structure of materials.
- Hertz elastic contact theory is used for deriving elastic properties (reduced modulus, Young's modulus, yield shear stress) for the two groups of OPGs. Due to the nature of structural heterogeneities that lead to the highly data scattering, Weibull distribution is then used as the analysis method for obtaining the expected mean values of derived elastic properties. The expected mean value of Young's modulus is 21.82 ± 19.76 and 15.20 ± 14.30 kPa , while corresponding yield shear stress is 0.70 ± 0.58 and 0.46 ± 0.44 kPa, for March and June group, respectively.

- Through the data comparison with prior studies, the OPGs biofilms show data similarity in elastic properties with the P. aeruginosa biofilms reported by Körstgens et al. (2001a, 2001b), which could be accounted for with the similar cultivation conditions and loading rate applied on biofilms in each study.

Acknowledgements

This work was supported by the U.S. National Science Foundation (NSF) under Award No. CMMI 1702881. The first author also received partial support from the Charles F. Perrell Scholarship. Any opinions, findings, and conclusions expressed in this paper are those of the authors and do not necessarily reflect the views of the NSF.

CHAPTER 7

CONCLUSIONS AND FUTURE WORK

7.1 Conclusions

The overall objective of this dissertation was to understand the underlying particle interaction mechanism for the flocculation and aggregation of clay minerals, mechanics of clay aggregates and biofilm granules by developing systematic techniques and data analytics that can be extended to the research of multiscale, composite materials in the future. In this section, a summary of the major findings obtained through all experimental studies on the clay aggregates and biofilm granules is presented as follows:

- The new data binning method is a useful tool in helping select the optimal bin size for the construction of histogram after a complete validation process from the synthetic and experimental data, which benefits the future study that involves the statistical analysis of individual constituents of composite materials.
- A simple, inexpensive method was developed to prepare micro- and macroscale clay aggregates with size of > 100 μm, which can be used as a cost-effective approach for the further research that involves the large-sized clay aggregates.
- A framework was successfully applied to account for the effects of ionic strength and pH on the flocculation and aggregation of clay minerals and corresponding size kinetics under these conditions.

- The mechanical behavior of clay was successfully investigated as a particulate system by conducting a systematic experiment on the unconfined compression testing of mesoscale clay aggregates prepared with different mineralogy and water chemistry. Interfacial forces play an important role in controlling the mechanical properties of clay aggregates and microfabric pattern, which, in turn, is affected by the water chemistry.
- The newly developed techniques and data analytics originally developed for the mechanical behavior of individual clay aggregates were examined by conducting the experimental studies on the OPGs, a form of macroscale aggregates composed of biofilms. The new findings here can not only provide reference data for the further studies of biofilm's mechanics, but also links the research opportunity between geotechnical and biological communities.

7.2 Future perspectives

Despite the new findings obtained from this dissertation, there are still several potential research topics that can be explored in the future, which are briefly described as follows:

(1) The PDF-based deconvolution, of which the optimal bin size for constructing the histogram can be determined by BSI method, still has disadvantages that the number of modes is uncertain at the same bin size. Thus, future efforts can be made to improve the current BSI method by accurately determining the number of modes for each tested bin size.

(2) The clay aggregates used for the characterization of mechanical behavior in this dissertation are basically micro-and macroscale ones with particle size of >~100 μm. Future study of aggregate's mechanics smaller than this size range, for example, particle groups with size range of ~10 to 30 μm (i.e., flocculi/pellets), will be interesting and promising to unravel the mechanics of clay at microscale.

(3) Numerical simulations quantifying the clay particle orientation of aggregates during compression will provide more insights into the development of multiscale mechanics and fabric evolution

(4) Future efforts are worth making in conducting the experimental investigation of complexes composed of different biofilms and clay minerals, which can be of great interest to the geotechnical and environmental communities.

BIBLIOGRAPHY

Abe, Y., Polyakov, P., Skali-Lami, S., and Francius, G. (2011). “Elasticity and physico-chemical properties during drinking water biofilm formation.” *Biofouling*.

Ahimou, F., Semmens, M. J., Novak, P. J., and Haugstad, G. (2007). “Biofilm cohesiveness measurement using a novel atomic force microscopy methodology.” *Applied and Environmental Microbiology*.

Akaike, H. (1974). “A New Look at the Statistical Model Identification.” *IEEE Transactions on Automatic Control*.

Alimova, A., Katz, A., Steiner, N., Rudolph, E., Wei, H., Steiner, J. C., and Gottlieb, P. (2009). “Bacteria-clay interaction: Structural changes in smectite induced during biofilm formation.” *Clays and Clay Minerals*, 57(2), 205–212.

Alimova, A., Roberts, M., Katz, A., Rudolph, E., Steiner, J. C., Alfano, R. R., and Gottlieb, P. (2006). “Effects of smectite clay on biofilm formation by microorganisms.” *Biofilms*, 3(1), 47–54.

Alldredge, A. L., and Silver, M. W. (1988). “Characteristics, dynamics and significance of marine snow.” *Progress in Oceanography*.

Alshibli, K., Cil, M. B., Kenesei, P., and Lienert, U. (2013). “Strain tensor determination of compressed individual silica sand particles using high-energy synchrotron diffraction.” *Granular Matter*.

Alto, P. (2013). *Electricity Use and Management in the Municipal Water Supply and Wastewater Industries*. *Electric Power Research Institute*.

Amirrahmat, S., Imseeh, W. H., Alshibli, K. A., Kenesei, P., Jarrar, Z. A., and Sharma, H. (2020). “3D Experimental Measurements of Evolution of Force Chains in Natural Silica Sand.” *Journal of Geotechnical and Geoenvironmental Engineering*, 146(5), 04020027.

Andrews, S., Nover, D., and Schladow, S. G. (2010). “Using laser diffraction data to obtain accurate particle size distributions: The role of particle composition.” *Limnology and Oceanography: Methods*.

Antonyuk, S., Tomas, J., Heinrich, S., and Mörl, L. (2005). “Breakage behaviour of spherical granulates by compression.” 60, 4031–4044.

Au, P. I., Clode, P., Smart, R. S. C., and Leong, Y. K. (2015). “Surface chemistry-microstructure-rheology of high and low crystallinity KGa-1b and KGa-2 kaolinite suspensions.” *Colloids and Surfaces A: Physicochemical and Engineering Aspects*, Elsevier B.V., 484, 354–364.

Bache, D. H. (2004). “Floc rupture and turbulence: A framework for analysis.” *Chemical Engineering Science*.

Ben-Yaakov, D., Andelman, D., and Podgornik, R. (2011). “Dielectric decrement as a source of ion-specific effects.” *Journal of Chemical Physics*.

Bennett, K. C., Berla, L. A., Nix, W. D., and Borja, R. I. (2015). “Instrumented nanoindentation and 3D mechanistic modeling of a shale at multiple scales.” *Acta Geotechnica*.

Bergaya, F., and Lagaly, G. (2006). “Chapter 1 General Introduction: Clays, Clay Minerals, and Clay Science.” *Developments in Clay Science*.

Bhat, H., and Kumar, N. (2010). “On the derivation of the Bayesian Information Criterion.” *School of Natural Sciences, University of California*, (November), 1–4.

De Boer, A. H., Gjaltema, D., Hagedoorn, P., and Frijlink, H. W. (2002). "Characterization of inhalation aerosols: A critical evaluation of cascade impactor analysis and laser diffraction technique." *International Journal of Pharmaceutics*.

Bolt, G. H. (1985). "The Surface Chemistry of Soils." *Clays and Clay Minerals*.

De Bono, J. P., and McDowell, G. R. (2014). "DEM of triaxial tests on crushable sand." *Granular Matter*, 16(4), 551–562.

Borba, A., Vareda, J. P., Durães, L., Portugal, A., and Simões, P. N. (2017). "Spectroscopic characterization of silica aerogels prepared using several precursors-effect on the formation of molecular clusters." *New Journal of Chemistry*, 41(14), 6742–6759.

Borkovec, M., Szilagyi, I., Popa, I., Finessi, M., Sinha, P., Maroni, P., and Papastavrou, G. (2012). "Investigating forces between charged particles in the presence of oppositely charged polyelectrolytes with the multi-particle colloidal probe technique." *Advances in Colloid and Interface Science*.

Boudarel, H., Mathias, J. D., Blaysat, B., and Grédiac, M. (2018). "Towards standardized mechanical characterization of microbial biofilms: analysis and critical review." *npj Biofilms and Microbiomes*, Springer US, 4(1), 1–15.

Brigatti, M. F., Galan, E., and Theng, B. K. G. (2006). "Chapter 2 Structures and Mineralogy of Clay Minerals." *Developments in Clay Science*.

Brigatti, M. F., Galán, E., and Theng, B. K. G. (2013). "Structure and Mineralogy of Clay Minerals." *Developments in Clay Science*.

Brindley, and Kurtossy. (1961). "Quantitative determination of kaolinite by X-ray diffraction." *Journal of the mineralogical society of America*, 46(11–12), 1205–1215.

Brown, J. M., Abramson, E. H., and Angel, R. J. (2006). "Triclinic elastic constants for low albite." *Physics and Chemistry of Minerals*, 33(4), 256–265.

Camp, T., and Stein, P. (1943). "Velocity gradients and internal work in fluid motion." *Boston Society of Civil Engineers*.

Çelik, M. S. (2004). "Electrokinetic behavior of clay surfaces." *Interface Science and Technology*, 1(C), 57–89.

Celis, R., Koskinen, W. C., Hermosin, M. C., and Cornejo, J. (1999). "Sorption and desorption of triadimefon by soils and model soil colloids." *Journal of Agricultural and Food Chemistry*, 47(2), 776–781.

Chang, C. S., Deng, Y., and Yang, Z. (2017). "Modeling of Minimum Void Ratio for Granular Soil with Effect of Particle Size Distribution." *Journal of Engineering Mechanics*.

Chang, C. S., Hicher, P.-Y., Yin, Z. Y., and Kong, L. R. (2009). "Elastoplastic Model for Clay with Microstructural Consideration." *Journal of Engineering Mechanics*.

Chang, C. S., Meidani, M., and Deng, Y. (2018). "Role of morphologic indices on the variation of limiting void ratios for uniform sands." *Geotechnique Letters*.

Chen, M. J., Zhang, Z., and Bott, T. R. (2005a). "Effects of operating conditions on the adhesive strength of Pseudomonas fluorescens biofilms in tubes." *Colloids and Surfaces B: Biointerfaces*.

Chen, M. S., Wartel, S., and Temmerman, S. (2005b). "Seasonal variation of floc characteristics on tidal flats, the Scheldt estuary." *Hydrobiologia*.

Cil, M. B., and Alshibli, K. A. (2012). "3D assessment of fracture of sand particles using discrete element method." *Geotechnique Letters*.

Cil, M. B., and Alshibli, K. A. (2014). "3D evolution of sand fracture under 1D compression." *Geotechnique*.

Cil, M. B., Alshibli, K. A., McDowell, G. R., and Li, H. (2013). "Discussion: 3D assessment of fracture of sand particles using discrete element method." *Geotechnique Letters*, 3(JAN/MAR), 13–15.

Clarke, S. D., and Hird, C. C. (2012). "Modelling of viscous effects in natural clays." *Canadian Geotechnical Journal*.

Collins, K., and Mcgown, A. (1974). "The Form and Function of Microfabric Features in a Variety of Natural Soils." *Geotechnique*.

Collins, R. (1984). "Characterization of expansive soil microfabric."

Cundall, P., and Strack, O. (1979). "A discrete numerical model for granular assemblies." *Geeotechnique*, 29(29), 47–65.

Dean, J. A. (1990). "Lange's handbook of chemistry." *Materials and Manufacturing Processes*.

Deirieh, A., Chang, I. Y., Whittaker, M. L., Weigand, S., Keane, D., Rix, J., Germaine, J. T., Joester, D., and Flemings, P. B. (2018). "Particle arrangements in clay slurries: The case against the honeycomb structure." *Applied Clay Science*.

DeJong, M. J., and Ulm, F. J. (2007). "The nanogranular behavior of C-S-H at elevated temperatures (up to 700 °C)." *Cement and Concrete Research*.

Delage, P., Audiguier, M., Cui, Y. J., and Howat, M. D. (1996). "Microstructure of a compacted silt." *Canadian Geotechnical Journal*, 33(1), 150–158.

Delhorme, M., Labbez, C., Caillet, C., and Thomas, F. (2010). "Acid-base properties of 2:1 clays. I. modeling the role of electrostatics." *Langmuir*.

Derjaguin, B., and Landau, L. (1993). "Theory of the stability of strongly charged lyophobic sols and of the adhesion of strongly charged particles in solutions of electrolytes." *Progress in Surface Science*.

Derjaguin, B. V, and Landau, L. (1941). "Theory of stability of highly charged lyophobic sols and adhesion of highly charged particles in solutions of electrolytes." *Acta Physico-Chimica USSR*.

Dobrynin, A. V., and Rubinstein, M. (2005). "Theory of polyelectrolytes in solutions and at surfaces." *Progress in Polymer Science (Oxford)*.

Dong, J., Cheng, Y., Hu, B., Hao, C., Tu, Q., and Liu, Z. (2018). "Experimental study of the mechanical properties of intact and tectonic coal via compression of a single particle." *Powder Technology*, Elsevier B.V., 325, 412–419.

Dor, M., Levi-Kalisman, Y., Day-Stirrat, R. J., Mishael, Y., and Emmanuel, S. (2020). "Assembly of clay mineral platelets, tactoids, and aggregates: Effect of mineral structure and solution salinity." *Journal of Colloid and Interface Science*.

Droppo, I. G., Leppard, G. G., Flannigan, D. T., and Liss, S. N. (1997). "The freshwater floc: A functional relationship of water and organic and inorganic floc constituents affecting suspended sediment properties." *Water, Air, and Soil Pollution*.

Du, J., Hu, L., Meegoda, J. N., and Zhang, G. (2018). "Shale softening: Observations, phenomenological behavior, and mechanisms." *Applied Clay Science*, Elsevier, 161(May), 290–300.

Du, Q., Sun, Z., Forsling, W., and Tang, H. (1997). "Acid-base properties of aqueous illite surfaces." *Journal of Colloid and Interface Science*.

Duc, M., Gaboriaud, F., and Thomas, F. (2005). "Sensitivity of the acid-base properties of clays to the methods of preparation and measurement: 2. Evidence from continuous potentiometric titrations." *Journal of Colloid and Interface Science*.

Ducker, W., Senden, T., and Pashley, R. (1992). "Measurement of forces in liquids using a force microscope." *Langmuir*, 8(7), 1831–1836.

Eisma, D. (1986). "Flocculation and de-flocculation of suspended matter in estuaries." *Netherlands Journal of Sea Research*.

Elfrink, B., and Baldock, T. (2002). "Hydrodynamics and sediment transport in the swash zone: A review and perspectives." *Coastal Engineering*.

Eliyahu, M., Emmanuel, S., Day-Stirrat, R. J., and Macaulay, C. I. (2015). "Mechanical properties of organic matter in shales mapped at the nanometer scale." *Marine and Petroleum Geology*, Elsevier Ltd, 59, 294–304.

Ferry, J. D. (1980). *Viscoelastic Properties of Polymers, 3rd Edition*.

Findley, W. N., Lai, J. S., Onaran, K., and Christensen, R. M. (1977). "Creep and Relaxation of Nonlinear Viscoelastic Materials With an Introduction to Linear Viscoelasticity." *Journal of Applied Mechanics*.

François, R. J. (1987). "Strength of aluminium hydroxide flocs." *Water Research*.

Freedman, D., and Diaconis, P. (1981). "On the histogram as a density estimator:L2 theory." *Zeitschrift für Wahrscheinlichkeitstheorie und Verwandte Gebiete*, 57(4), 453–476.

Furukawa, Y., Reed, A. H., and Zhang, G. (2014). "Effect of organic matter on estuarine flocculation: A laboratory study using montmorillonite, humic acid, xanthan gum, guar gum and natural estuarine flocs." *Geochemical Transactions*.

Furukawa, Y., Watkins, J. L., Kim, J., Curry, K. J., and Bennett, R. H. (2009). "Aggregation of montmorillonite and organic matter in aqueous media containing artificial seawater." *Geochemical Transactions*.

Gagliano, M. C., Ismail, S. B., Stams, A. J. M., Plugge, C. M., Temmink, H., and Van Lier, J. B. (2017). "Biofilm formation and granule properties in anaerobic digestion at high salinity." *Water Research*.

Galy, O., Latour-Lambert, P., Zrelli, K., Ghigo, J. M., Beloin, C., and Henry, N. (2012). "Mapping of bacterial biofilm local mechanics by magnetic microparticle actuation." *Biophysical Journal*.

Gao, Y., and Mucci, A. (2001). "Acid base reaction, phosphate and arsenate complexation, and thier competitive adsorption at the surface of geothite in 0.7 M nacl solution." *Geochimica et Cosmochimica Acta*.

García-García, S., Jonsson, M., and Wold, S. (2006). "Temperature effect on the stability of bentonite colloids in water." *Journal of Colloid and Interface Science*.

Gens, A., and Alonso, E. E. (1992). "A framework for the behaviour of unsaturated expansive clays." *Canadian Geotechnical Journal*, 29(6), 1013–1032.

Gittings, M. R., Cipelletti, L., Trappe, V., Weitz, D. A., In, M., and Lal, J. (2001). "The effect of solvent and ions on the structure and rheological properties of guar solutions." *Journal of Physical Chemistry A*.

Goetz, A. S. D. and P. J. (2010). *Characterization of Liquids, Nano- and Microparticulates, and Porous Bodies Using Ultrasound. Studies in Interface Science*.

Goldberg, S., Forster, H. S., and Godfrey, C. L. (1996). "Molybdenum Adsorption on Oxides, Clay Minerals, and Soils." *Soil Science Society of America Journal*.

Govoreanu, R., Saveyn, H., Van Der Meeren, P., Nopens, I., and Vanrolleghem, P. A. (2009). "A methodological approach for direct quantification of the activated sludge floc size distribution by using different techniques." *Water Science and Technology*.

Govoreanu, R., Seghers, D., Nopens, I., De Clercq, B., Saveyn, H., Capalozza, C., Van Der Meeren, P., Verstraete, W., Top, E., and Vanrolleghem, P. A. (2003). "Linking floc structure and settling properties to activated sludge population dynamics in an SBR." *Water Science and Technology*.

Graf, W. H. (1999). "Erosion and sedimentation." *Journal of Hydraulic Engineering*, 125(5), 554–555.

Greaves, D., Boxall, J., Mulligan, J., Montesi, A., Creek, J., Dendy Sloan, E., and Koh, C. A. (2008). "Measuring the particle size of a known distribution using the focused beam reflectance measurement technique." *Chemical Engineering Science*.

Green, S. A., and Blough, N. V. (1994). "Optical absorption and fluorescence properties of chromophoric dissolved organic matter in natural waters." *Limnology and Oceanography*.

Gregory, J. (1988). "Polymer adsorption and flocculation in sheared suspensions." *Colloids and Surfaces*.

Gregory, J. (1989). "Fundamentals of flocculation." *Critical Reviews in Environmental Control*.

Gu, X., and Evans, L. J. (2008). "Surface complexation modelling of Cd(II), Cu(II), Ni(II), Pb(II) and Zn(II) adsorption onto kaolinite." *Geochimica et Cosmochimica Acta*.

Guérin, L., Frances, C., Liné, A., and Coufort-Saudejaud, C. (2019). "Fractal dimensions and morphological characteristics of aggregates formed in different physico-chemical and mechanical flocculation environments." *Colloids and Surfaces A: Physicochemical and Engineering Aspects*.

Gupta, A., and Stone, H. A. (2018). "Electrical Double Layers: Effects of Asymmetry in Electrolyte Valence on Steric Effects, Dielectric Decrement, and Ion-Ion Correlations." *Langmuir*.

Gupta, V., Hampton, M. A., Stokes, J. R., Nguyen, A. V., and Miller, J. D. (2011). "Particle interactions in kaolinite suspensions and corresponding aggregate structures." *Journal of Colloid and Interface Science*.

Han, Q., Qu, Z., and Ye, Z. (2018). "Research on the mechanical behaviour of shale based on multiscale analysis." *Royal Society Open Science*.

Hao, W., Flynn, S. L., Alessi, D. S., and Konhauser, K. O. (2018). "Change of the point of zero net proton charge (pHPZNPC) of clay minerals with ionic strength." *Chemical Geology*.

Harris, R. H., and Mitchell, R. (1973). "The role of polymers in microbial aggregation." *Annual review of microbiology*.

Harvey, C. C., and Murray, H. H. (1997). "Industrial clays in the 21st century: A perspective of exploration, technology and utilization." *Applied Clay Science*.

Hatcher, A., Hill, P., and Grant, J. (2001). "Optical backscatter of marine flocs." *Journal of Sea Research*.

He, W., Nan, J., Li, H., and Li, S. (2012). "Characteristic analysis on temporal evolution of floc size and structure in low-shear flow." *Water Research*, Elsevier Ltd, 46(2), 509–520.

He, Y., Peterson, B. W., Jongsma, M. A., Ren, Y., Sharma, P. K., Busscher, H. J., and van der Mei, H. C. (2013). "Stress Relaxation Analysis Facilitates a Quantitative Approach towards Antimicrobial Penetration into Biofilms." *PLoS ONE*.

Heath, A. R., Fawell, P. D., Bahri, P. A., and Swift, J. D. (2002). "Estimating average particle size by focused beam reflectance measurement (FBRM)." *Particle and Particle Systems Characterization*.

Hermawan, M., Bushell, G., Bickert, G., and Amal, R. (2003). "Relationship between floc short range structure and sediment compaction." *Particle and Particle Systems Characterization*.

Hermawan, M., Bushell, G., Bickert, G., and Amal, R. (2004). "Characterisation of short-range structure of silica aggregates-implication to sediment compaction." *International Journal of Mineral Processing*.

Heyliger, P., Ledbetter, H., and Kim, S. (2003a). "Elastic constants of natural quartz." *The Journal of the Acoustical Society of America*, 114(2), 644–650.

Heyliger, P., Ledbetter, H., and Kim, S. (2003b). "Elastic constants of natural quartz." *The Journal of the Acoustical Society of America*.

Hill, P. S. (1998). "Controls on floc size in the sea." *Oceanography*.

Hou, D., Li, D., Hua, P., Jiang, J., and Zhang, G. (2019). "Statistical modelling of compressive strength controlled by porosity and pore size distribution for cementitious materials." *Cement and Concrete Composites*.

Hou, D., Zhang, G., Pant, R. R., Shen, J. S., Liu, M., and Luo, H. (2016). "Nanoindentation characterization of a Ternary clay-based composite used in ancient chinese construction." *Materials*.

Hou, J., Li, H., Zhu, H., and Wu, L. (2009). "Determination of Clay Surface Potential: A More Reliable Approach." *Soil Science Society of America Journal*, 73(5), 1658–1663.

Hower, J., and Mowatt, T. (1966). "The mineralogy of illites and mixed-layer illite/montmorillonite." *Amer. Mineral*.

Huang, H. (1993). "Porosity-size relationship of drilling mud flocs: Fractal structure." *Clays and Clay Minerals*.

Huang, R., Wang, Y., Cheng, S., Liu, S., and Cheng, L. (2015). "Selection of logging-based TOC calculation methods for shale reservoirs: A case study of the Jiaoshiba shale gas field in the Sichuan Basin." *Natural Gas Industry B*.

Israelachvili, J. N. (2011). "Steric (Polymer-Mediated) and Thermal Fluctuation Forces." *Intermolecular and Surface Forces*.

Janek, M., and Lagaly, G. (2001). "Proton saturation and rheological properties of smectite dispersions." *Applied Clay Science*.

Jara, A. A., Goldberg, S., and Mora, M. L. (2005). "Studies of the surface charge of amorphous aluminosilicates using surface complexation models." *Journal of Colloid and Interface Science*.

Jarvis, P., Jefferson, B., Gregory, J., and Parsons, S. A. (2005a). "A review of floc strength and breakage." *Water Research*, 39(14), 3121–3137.

Jarvis, P., Jefferson, B., Gregory, J., and Parsons, S. A. (2005b). "A review of floc strength and breakage." *Water Research*.

Jayatilaka, A. D. S., and Trustrum, K. (1977). "Statistical approach to brittle fracture." *Journal of Materials Science*.

Johnson, N. L., W. Kemp, A., and Kotz, S. (2005). *Univariate Discrete Distributions: Third Edition*. *Univariate Discrete Distributions: Third Edition*.

Kang, X., Xia, Z., Chen, R., Liu, P., and Yang, W. (2019). "Effects of inorganic cations and organic polymers on the physicochemical properties and microfabrics of kaolinite suspensions." *Applied Clay Science*.

Karthiga Devi, K., and Natarajan, K. A. (2015). "Production and characterization of bioflocculants for mineral processing applications." *International Journal of Mineral Processing*.

Kaszuba, M., Corbett, J., Watson, F. M. N., and Jones, A. (2010). "High-concentration zeta potential measurements using light-scattering techniques." *Philosophical Transactions of the Royal Society A: Mathematical, Physical and Engineering Sciences*.

Keyvani, A., and Strom, K. (2013). "A fully-automated image processing technique to improve measurement of suspended particles and flocs by removing out-of-focus objects." *Computers and Geosciences*.

Keyvani, A., and Strom, K. (2014). "Influence of cycles of high and low turbulent shear on the growth rate and equilibrium size of mud flocs." *Marine Geology*, Elsevier B.V., 354, 1–14.

Kiliaris, P., and Papaspyrides, C. D. (2010). "Polymer/layered silicate (clay) nanocomposites: An overview of flame retardancy." *Progress in Polymer Science (Oxford)*, Elsevier Ltd, 35(7), 902–958.

Kim, S., and Palomino, A. M. (2009). "Polyacrylamide-treated kaolin: A fabric study." *Applied Clay Science*, Elsevier B.V., 45(4), 270–279.

Kinter, E., and Diamond, S. (1956). "Gravimetric Determination of Monolayer Glycerol Complexes of Clay Minerals." *Clays and Clay Minerals*, 5(1), 318–333.

Kleijn, W. B., and Oster, J. D. (1982). "A model of clay swelling and tactoid formation." *Clays & Clay Minerals*.

Klein, C. A. (2009). "Characteristic strength, Weibull modulus, and failure probability of fused silica glass." *Optical Engineering*.

Kobayashi, M. (1999). "Breakup of fractal floes in a turbulent flow." *Langmuir*.

Kollannur, N. J., and Arnepalli, D. N. (2019). "Methodology for Determining Point of Zero Salt Effect of Clays in Terms of Surface Charge Properties." *Journal of Materials in Civil Engineering*.

Konduri, M. K. R., and Fatehi, P. (2017). "Influence of pH and ionic strength on flocculation of clay suspensions with cationic xylan copolymer." *Colloids and Surfaces A: Physicochemical and Engineering Aspects*.

Korolev, V. A., and Nesterov, D. S. (2018). "Regulation of clay particles charge for design of protective electrokinetic barriers." *Journal of Hazardous Materials*.

Körstgens, V., Flemming, H. C., Wingender, J., and Borchard, W. (n.d.). "Uniaxial compression measurement device for investigation of the mechanical stability of biofilms." *Journal of Microbiological Methods*.

Körstgens, V., Flemming, H. C., Wingender, J., and Borchard, W. (n.d.). "Influence of calcium ions on the mechanical properties of a model biofilm of mucoid Pseudomonas aeruginosa." *Water Science and Technology*.

Kranenburg, C. (1994). "The fractal structure of cohesive sediment aggregates." *Estuarine, Coastal and Shelf Science*.

Kühnel, R. A. (1990). "Handbook of determinative methods in clay mineralogy." *Applied Clay Science*, 5(2), 190–191.

Kumar, N., Andersson, M. P., Van Den Ende, D., Mugele, F., and Siretanu, I. (2017).

"Probing the Surface Charge on the Basal Planes of Kaolinite Particles with High-Resolution Atomic Force Microscopy." *Langmuir*, 33(50), 14226–14237.

Kunz, D. A., Max, E., Weinkamer, R., Lunkenbein, T., Breu, J., and Fery, A. (2009). "Deformation Measurements on Thin Clay Tactoids." 1816–1820.

Kuprenas, R., Tran, D., and Strom, K. (2018). "A Shear-Limited Flocculation Model for Dynamically Predicting Average Floc Size." *Journal of Geophysical Research: Oceans*.

L.Johnson, K. (1985). *Contact mechanics. Cambridge University Press, Cambridge, New York.*

Laird, D. A. (2006). "Influence of layer charge on swelling of smectites." *Applied Clay Science*.

Lambe, and Whitman. (1969). "Soil Mechanics." John Wiley and Sons.

Lan, Y., Deng, B., Kim, C., and Thornton, E. C. (2007). "Influence of soil minerals on chromium(VI) reduction by sulfide under anoxic conditions." *Geochemical Transactions*, 8(Vi), 1–10.

Landhal, M. T., and Mollo-Christensen, E. (1992). *Turbulence and random processes in fluid mechanics*. Cambridge University Press.

Langmuir, I. (1938). "The role of attractive and repulsive forces in the formation of tactoids, thixotropic gels, protein crystals and coacervates." *The Journal of Chemical Physics*.

Lavallee, K. D., Kineke, G. C., and Milligan, T. G. (2020). "Variability of Cohesive Particle Characteristics in an Energetic Estuary: Flocs vs. Aggregates." *Estuaries and Coasts*, Estuaries and Coasts, 43(1), 39–55.

Lee, B. J., Fettweis, M., Toorman, E., and Molz, F. J. (2012). "Multimodality of a particle size distribution of cohesive suspended particulate matters in a coastal zone." *Journal of Geophysical Research: Oceans*, 117(3).

Lee, H., and Kim, C. (2018). "Experimental study on reversible formation of 2D flocs from plate-like particles dispersed in Newtonian fluid under torsional flow." *Colloids and Surfaces A: Physicochemical and Engineering Aspects*.

Lefebvre, G., and Delage, P. (1986). "The use of mercury intrusion porosimetry for the analysis of soft clay microstructure." *Recent developments in laboratory and field tests and analysis of geotechnical problems. Proc. symposium, Bangkok, 1983*.

Van Leussen, W. (2011). "Macroflocs, fine-grained sediment transports, and their longitudinal variations in the Ems Estuary." *Ocean Dynamics*.

Lewis, W. M. (2009). "Ecological Zonation in Lakes." *Encyclopedia of Inland Waters*.

Li, H., Chen, J., Peng, C., Min, F., and Song, S. (2020). "Salt coagulation or flocculation? In situ zeta potential study on ion correlation and slime coating with the presence of clay: A case of coal slurry aggregation." *Environmental Research*.

Li, H., Qing, C. Le, Wei, S. Q., and Jiang, X. J. (2004). "An approach to the method for determination of surface potential on solid/liquid interface: Theory." *Journal of Colloid and Interface Science*, 275(1), 172–176.

Li, M., Wilkinson, D., and Patchigolla, K. (2005). "Comparison of particle size distributions measured using different techniques." *Particulate Science and Technology*.

Li, W., Rezakhani, R., Jin, C., Zhou, X., and Cusatis, G. (2017). "A multiscale framework for the simulation of the anisotropic mechanical behavior of shale." *International*

Journal for Numerical and Analytical Methods in Geomechanics.

Li, X., Zhai, X., Chu, H. P., and Zhang, J. (2008). "Characterization of the Flocculation Process from the Evolution of Particle Size Distributions." *Journal of Environmental Engineering*.

Li, Y., Luo, S., Lu, M., Wu, Y., Zhou, N., Wang, D., Lu, Y., and Zhang, G. (2021). "Cross-scale characterization of sandstones via statistical nanoindentation: Evaluation of data analytics and upscaling models." *International Journal of Rock Mechanics and Mining Sciences*, Elsevier Ltd, 142(February), 104738.

van Lier, J. B., van der Zee, F. P., Frijters, C. T. M. J., and Ersahin, M. E. (2015). "Celebrating 40 years anaerobic sludge bed reactors for industrial wastewater treatment." *Reviews in Environmental Science and Biotechnology*.

Likos, W. J., and Lu, N. (2001). "A Laser Technique to Quantify the Size, Porosity, and Density of Clay Clusters during Sedimentation." *Geotechnical Testing Journal*.

Lin, B., and Cerato, A. B. (2014). "Applications of SEM and ESEM in microstructural investigation of shale-weathered expansive soils along swelling-shrinkage cycles." *Engineering Geology*.

Liu, C., Liu, F., Song, J., Ma, F., Wang, D., and Zhang, G. (2021). "On the measurements of individual particle properties via compression and crushing." *Journal of Rock Mechanics and Geotechnical Engineering*, Elsevier Ltd, 13(2), 377–389.

Liu, D., Edraki, M., Fawell, P., and Berry, L. (2020a). "Improved water recovery: A review of clay-rich tailings and saline water interactions." *Powder Technology*.

Liu, D., and Peng, Y. (2014). "Reducing the entrainment of clay minerals in flotation using tap and saline water." *Powder Technology*.

Liu, W. (2001). "Modeling description and spectroscopic evidence of surface acid-base properties of natural illites." *Water Research*.

Liu, W., Zhang, L., and Luo, N. (2020b). "Elastic modulus evolution of rocks under heating–cooling cycles." *Scientific Reports*, Nature Publishing Group UK, 10(1), 1–9.

Liu, X., Hu, F., Ding, W., Tian, R., Li, R., and Li, H. (2015). "A how-to approach for estimation of surface/Stern potentials considering ionic size and polarization." *Analyst*, Royal Society of Chemistry, 140(21), 7217–7224.

Liu, X., Tian, R., Du, W., Li, R., Ding, W., and Li, H. (2019). "A theory to determine the surface potentials of clay particles in electrolyte solutions." *Applied Clay Science*.

Liu, Y., Alessi, D. S., Flynn, S. L., Alam, M. S., Hao, W., Gingras, M., Zhao, H., and Konhauser, K. O. (2018). "Acid-base properties of kaolinite, montmorillonite and illite at marine ionic strength." *Chemical Geology*.

Liu, Y., and Tay, J. H. (2002). "The essential role of hydrodynamic shear force in the formation of biofilm and granular sludge." *Water Research*.

Liu, Z., Liu, F., Ma, F., Wang, M., Bai, X., Zheng, Y., Yin, H., and Zhang, G. (2016). "Collapsibility, composition, and microstructure of loess in china." *Canadian Geotechnical Journal*, 53(4), 673–686.

Long, J., Xu, Z., and Masliyah, J. H. (2006). "Role of illite-illite interactions in oil sands processing." *Colloids and Surfaces A: Physicochemical and Engineering Aspects*.

Lu, Y., Li, Y., Wu, Y., Luo, S., Jin, Y., and Zhang, G. (2020). "Characterization of Shale Softening by Large Volume-Based Nanoindentation." *Rock Mechanics and Rock Engineering*, Springer Vienna, 53(3), 1393–1409.

Luckham, P. F., and Rossi, S. (1999). “Colloidal and rheological properties of bentonite suspensions.” *Advances in Colloid and Interface Science*.

Luo, S., Kim, D., Wu, Y., Li, Y., Wang, D., Song, J., DeGroot, D. J., and Zhang, G. (2021). *Big Data Nanoindentation and Analytics Reveal the Multi-Staged, Progressively-Homogenized, Depth-Dependent Upscaling of Rocks’ Properties*. *Rock Mechanics and Rock Engineering*, Springer Vienna.

Luo, S., Lu, Y., Wu, Y., Song, J., DeGroot, D. J., Jin, Y., and Zhang, G. (2020). “Cross-scale characterization of the elasticity of shales: Statistical nanoindentation and data analytics.” *Journal of the Mechanics and Physics of Solids*, Elsevier Ltd, 140, 103945.

Ma, F., Song, J., Luo, S., DeGroot, D. J., Bai, X., and Zhang, G. (2019). “Distinct responses of nanostructured layered muscovite to uniform and nonuniform straining.” *Journal of Materials Science*, Springer US, 54(2), 1077–1098.

Maggi, F. (2005). “Flocculation dynamics of cohesive sediment.” *Communications on Hydraulic and Geotechnical Engineering*.

Manning, A. J., and Bass, S. J. (2006). “Variability in cohesive sediment settling fluxes: Observations under different estuarine tidal conditions.” *Marine Geology*.

Marchetti, M. C., Joanny, J. F., Ramaswamy, S., Liverpool, T. B., Prost, J., Rao, M., and Simha, R. A. (2013). “Hydrodynamics of soft active matter.” *Reviews of Modern Physics*.

Martin, R. T., and Ladd, C. C. (1975). “Fabric of consolidated kaolinite.” *Clays and Clay Minerals*, 23(1), 17–25.

Matsuo, T., and Unno, H. (1981). “Forces acting on floc and strength of floc.” *Journal of the Environmental Engineering Division*, 107(3).

Maximova, N., and Dahl, O. (2006). “Environmental implications of aggregation phenomena: Current understanding.” *Current Opinion in Colloid and Interface Science*.

Mazzoli, A., and Moriconi, G. (2014). “Particle size, size distribution and morphological evaluation of glass fiber reinforced plastic (GRP) industrial by-product.” *Micron*.

McCave, I. N., Bryant, R. J., Cook, H. F., and Coughanowr, C. A. (1986). “Evaluation of a laser-diffraction-size analyzer for use with natural sediments.” *Journal of Sedimentary Research*.

McGown A; Collins K. (1975). “The microfabrics of some expansive and collapsing soils.”

Mehta, A. J., Hayter, E. J., Parker, W. R., Krone, R. B., and Teeter, A. M. (1989). “Cohesive Sediment Transport. I: Process Description.” *Journal of Hydraulic Engineering*.

Meissner, T., and Wentz, F. (2004). “The complex dielectric constant of pure and sea water from microwave satellite observations.” *IEEE Transactions on Geoscience and Remote Sensing*, 42(9), 1836–1849.

Men, D., Patel, M. K., Usov, I. O., Toiammou, M., Monnet, I., Pivin, J. C., Porter, J. R., and Mecartney, M. L. (2013). “Radiation damage in multiphase ceramics.” *Journal of Nuclear Materials*.

Merkel, C., Deuschle, J., Griesshaber, E., Enders, S., Steinhauser, E., Hochleitner, R., Brand, U., and Schmahl, W. W. (2009). “Mechanical properties of modern calcite-(Mergerlia truncata) and phosphate-shelled brachiopods (Discradisca stella and Lingula anatina) determined by nanoindentation.” *Journal of Structural Biology*, Elsevier Inc., 168(3), 396–408.

Mietta, F., Chassagne, C., Manning, A. J., and Winterwerp, J. C. (2009). "Influence of shear rate, organic matter content, pH and salinity on mud flocculation." *Ocean Dynamics*.

Mikkelsen, O. A., Hill, P. S., and Milligan, T. G. (2006). "Single-grain, microfloc and macrofloc volume variations observed with a LISST-100 and a digital floc camera." *Journal of Sea Research*.

Mitchell, J., and Soga, K. (2005). *Fundamentals of Soil Behavior*. *Wiley*.

Miyahara, K., Adachi, Y., Nakaishi, K., and Ohtsubo, M. (2002). "Settling velocity of a sodium montmorillonite floc under high ionic strength." *Colloids and Surfaces A: Physicochemical and Engineering Aspects*.

Moore, D., and Reynolds, R. (1997). *X-Ray Diffraction and the Identification and Analysis of Clay Minerals*. Oxford University Press, New York.

Moruzzi, R. B., de Oliveira, A. L., da Conceição, F. T., Gregory, J., and Campos, L. C. (2017). "Fractal dimension of large aggregates under different flocculation conditions." *Science of the Total Environment*.

Muka, S. (2015). "Marine Biology." *A Companion to the History of American Science*.

Murray, H. H. (2000). "Traditional and new applications for kaolin, smectite, and palygorskite: A general overview." *Applied Clay Science*.

Nakata, Y., Kato, Y., Hyodo, M., Hyde, A., and Murata, H. (2001). "One-dimensional compression behaviour of uniformly graded sand related to single particle crushing strength." *Soils and Foundations*, 41(2), 39–51.

Nakayama, Y., and Andelman, D. (2015). "Differential capacitance of the electric double layer: The interplay between ion finite size and dielectric decrement." *Journal of Chemical Physics*.

Neumann, M. G., Gessner, F., Schmitt, C. C., and Sartori, R. (2002). "Influence of the layer charge and clay particle size on the interactions between the cationic dye methylene blue and clays in an aqueous suspension." *Journal of Colloid and Interface Science*.

Okaiyeto, K., Nwodo, U. U., Mabinya, L. V., Okoli, A. S., and Okoh, A. I. (2016). "Evaluation of flocculating performance of a thermostable bioflocculant produced by marine Bacillus sp." *Environmental Technology (United Kingdom)*.

Oldham, K. B. (2008). "A Gouy-Chapman-Stern model of the double layer at a (metal)/(ionic liquid) interface." *Journal of Electroanalytical Chemistry*.

Oliver, W. C., and Pharr, G. M. (1992). "An improved technique for determining hardness and elastic modulus using load and displacement sensing indentation experiments." *Journal of Materials Research*.

Van Olphen, H. (1977). *An introduction to clay colloid chemistry, for clay technologists, geologists, and soil scientists. An introduction to clay colloid chemistry, for clay technologists, geologists, and soil scientists.*

Owen, A. T., Fawell, P. D., Swift, J. D., Labbett, D. M., Benn, F. A., and Farrow, J. B. (2008). "Using turbulent pipe flow to study the factors affecting polymer-bridging flocculation of mineral systems." *International Journal of Mineral Processing*.

Paramonova, E., Kalmykowa, O. J., Van Der Mei, H. C., Busscher, H. J., and Sharma, P. K. (2009a). "Impact of hydrodynamics on oral biofilm strength." *Journal of Dental Research*.

Paramonova, E., Krom, B. P., van der Mei, H. C., Busscher, H. J., and Sharma, P. K. (2009b). "Hyphal content determines the compression strength of Candida albicans biofilms." *Microbiology*.

Park, and Dolan. (2015). "Algal-sludge granule for wastewater treatment and bioenergy feedstock generation."

Parker, D., Kaufman, W., and Jenkis, D. (1972). "Floc breakup in turbulent flocculation processes." *ASCE J Sanit Eng Div*.

Partheniades, E. (2009). *Cohesive Sediments in Open Channels*. *Cohesive Sediments in Open Channels*.

Peng, J., Luo, S., Wang, D., Cao, Y., DeGroot, D. J., and Zhang, G. (2022). "Multiple Thixotropisms of Liquid Limit–Consistency Clays Unraveled by Multiscale Experimentation." *Journal of Geotechnical and Geoenvironmental Engineering*, 148(1), 1–14.

Peterson, B. W., He, Y., Ren, Y., Zerdoum, A., Libera, M. R., Sharma, P. K., van Winkelhoff, A. J., Neut, D., Stoodley, P., van der Mei, H. C., and Busscher, H. J. (2015). "Viscoelasticity of biofilms and their recalcitrance to mechanical and chemical challenges." *FEMS Microbiology Reviews*.

Peterson, B. W., van der Mei, H. C., Sjollema, J., Busscher, H. J., and Sharma, P. K. (2013). "A distinguishable role of eDNA in the viscoelastic relaxation of biofilms." *mBio*.

Pevear, D. R. (1999). "Illite and hydrocarbon exploration." *Proceedings of the National Academy of Sciences of the United States of America*.

Philipps, K., Stoffel, R. P., Dronskowski, R., and Conradt, R. (2017). "Experimental and theoretical investigation of the elastic moduli of silicate glasses and crystals." *Frontiers in Materials*.

Poppele, E. H., and Hozalski, R. M. (2003). "Micro-cantilever method for measuring the tensile strength of biofilms and microbial flocs." *Journal of Microbiological Methods*.

Portnikov, D., and Kalman, H. (2014). "Determination of elastic properties of particles using single particle compression test." *Powder Technology*, Elsevier B.V., 268, 244–252.

Purevdorj, B., Costerton, J. W., and Stoodley, P. (2002). "Influence of hydrodynamics and cell signaling on the structure and behavior of Pseudomonas aeruginosa biofilms." *Applied and Environmental Microbiology*.

Qian, G., Lei, W., Yu, Z., and Berto, F. (2019). "Statistical size scaling of breakage strength of irregularly-shaped particles." *Theoretical and Applied Fracture Mechanics*, Elsevier, 102(April), 51–58.

Quirk;, and Aylmore. (1971). "Domains and quasi- crystalline regions in clay systems."

Richtering, W. (2019). "The Colloidal Domain – where physics, chemistry, biology and technology meet." *Applied Rheology*.

Safari, A., Tukovic, Z., Walter, M., Casey, E., and Ivankovic, A. (2015). "Mechanical properties of a mature biofilm from a wastewater system: from microscale to macroscale level." *Biofouling*.

Schlue, B. F., Moerz, T., and Kreiter, S. (2010). "Influence of shear rate on undrained vane shear strength of organic harbor mud." *Journal of Geotechnical and Geoenvironmental Engineering*.

Scott, D. W. (1979). "On optimal and data-based histograms." *Biometrika*.

Sehar, S., and Naz, I. (2016). "Role of the Biofilms in Wastewater Treatment." *Microbial Biofilms - Importance and Applications*.

Senaputra, A., Jones, F., Fawell, P. D., and Smith, P. G. (2014). "Focused beam reflectance measurement for monitoring the extent and efficiency of flocculation in mineral systems." *AIChE Journal*.

Seo, Y. J., Seol, J., Yeon, S. H., Koh, D. Y., Cha, M., Kang, S. P., Seo, Y. T., Bahk, J. J., Lee, J., and Lee, H. (2009). "Structural, mineralogical, and rheological properties of methane hydrates in smectite clays." *Journal of Chemical and Engineering Data*.

Shaikh, S. M. R., Nasser, M. S., Hussein, I., Benamor, A., Onaizi, S. A., and Qiblawey, H. (2017). "Influence of polyelectrolytes and other polymer complexes on the flocculation and rheological behaviors of clay minerals: A comprehensive review." *Separation and Purification Technology*, Elsevier B.V., 187, 137–161.

Shao, H., Chang, J., Lu, Z., Luo, B., Grundy, J. S., Xie, G., Xu, Z., and Liu, Q. (2019). "Probing Anisotropic Surface Properties of Illite by Atomic Force Microscopy." *Langmuir*.

Shi, D., Zheng, L., Xue, J., and Sun, J. (2016). "DEM Modeling of Particle Breakage in Silica Sands under One-Dimensional Compression." *Acta Mechanica Solida Sinica*, The Chinese Society of Theoretical and Applied Mechanics, 29(1), 78–94.

Shimazaki, H., and Shinomoto, S. (2007). "A method for selecting the bin size of a time histogram." *Neural Computation*.

Sincero, A. P., and Sincero, G. A. (2002). *Physical-chemical treatment of water and wastewater*. *Physical-Chemical Treatment of Water and Wastewater*.

Sjoblom, K. J. (2016). "Coarse-grained molecular dynamics approach to simulating clay behavior." *Journal of Geotechnical and Geoenvironmental Engineering*.

Song, J., Sun, Q., Luo, S., Arwade, S. R., Gerasimidis, S., Guo, Y., and Zhang, G. (2018). "Compression behavior of individual thin-walled metallic hollow spheres with patterned distributions of microporosity." *Materials Science and Engineering A*.

Song, J., Sun, Q., Yang, Z., Luo, S., Xiao, X., Arwade, S. R., and Zhang, G. (2017). "Effects of microporosity on the elasticity and yielding of thin-walled metallic hollow spheres." *Materials Science and Engineering A*.

Song, S., and Trass, O. (1997). "Floc flotation of prince coal with simultaneous grinding and hydrophobic flocculation in a Szego mill." *Fuel*.

Spicer, P. T., and Pratsinis, S. E. (1996). "Shear-induced flocculation: The evolution of floc structure and the shape of the size distribution at steady state." *Water Research*.

Sposito, G. (2018). "Gouy-chapman theory." *Encyclopedia of Earth Sciences Series*.

Sposito, G., Skipper, N. T., Sutton, R., Park, S. H., Soper, A. K., and Greathouse, J. A. (1999). "Surface geochemistry of the clay minerals." *Proceedings of the National Academy of Sciences of the United States of America*.

Sridharan, A., and Jayadeva, M. S. (1982). "Double layer theory and compressibility of clays." *Geotechnique*.

Strom, K. B., Kuhns, R. D., and Lucas, H. J. (2010). "Comparison of Automated Image-Based Grain Sizing to Standard Pebble-Count Methods." *Journal of Hydraulic Engineering*, 136(8), 461–473.

Sturges, H. A. (1926). "The Choice of a Class Interval." *Journal of the American Statistical Association*.

Šulc, R., Lemanowicz, M., and Gierczycki, A. T. (2012). "Effect of flocculant sonication on floc growth kinetics occurring in an agitated vessel." *Chemical Engineering and Processing: Process Intensification*.

Sumbekova, S., Iskakova, A., and Papathanasiou, A. (2019). "Microstructural clustering in multiphase materials and its quantification." *Physica A: Statistical Mechanics and its Applications*.

Tajima, R., and Kato, Y. (2011). "Comparison of threshold algorithms for automatic image processing of rice roots using freeware ImageJ." *Field Crops Research*.

Tan, X. (2013). "Microstructure and Physics-Based Structural Models for Suspended Clay-Exopolymer Flocs." Louisiana State University.

Tan, X., Hu, L., Reed, A. H., Furukawa, Y., and Zhang, G. (2014a). "Flocculation and particle size analysis of expansive clay sediments affected by biological, chemical, and hydrodynamic factors." *Ocean Dynamics*.

Tan, X., Hu, L., Reed, A. H., Furukawa, Y., and Zhang, G. (2014b). "Flocculation and particle size analysis of expansive clay sediments affected by biological, chemical, and hydrodynamic factors Topical Collection on the 11th International Conference on Cohesive Sediment Transport." *Ocean Dynamics*, 64(1), 143–157.

Tan, X. L., Zhang, G. P., Yin, H., Reed, A. H., and Furukawa, Y. (2012). "Characterization of particle size and settling velocity of cohesive sediments affected by a neutral exopolymer." *International Journal of Sediment Research*.

Tan, X., Liu, F., Hu, L., Reed, A. H., Furukawa, Y., and Zhang, G. (2017). "Evaluation of the particle sizes of four clay minerals." *Applied Clay Science*, Elsevier B.V., 135, 313–324.

Tang, Y., Li, H., Liu, X., Zhu, H., and Tian, R. (2015). "Unraveling the size distributions of surface properties for purple soil and yellow soil." *Journal of Environmental Sciences (China)*.

Terrell, G. R., and Scott, D. W. (1985). "Oversmoothed nonparametric density estimates." *Journal of the American Statistical Association*.

Tiraferri, A., and Borkovec, M. (2015). "Probing effects of polymer adsorption in colloidal particle suspensions by light scattering as relevant for the aquatic environment: An overview." *Science of the Total Environment*.

Tombácz, E., and Szekeres, M. (2004). "Colloidal behavior of aqueous montmorillonite suspensions: The specific role of pH in the presence of indifferent electrolytes." *Applied Clay Science*.

Tombácz, E., and Szekeres, M. (2006). "Surface charge heterogeneity of kaolinite in aqueous suspension in comparison with montmorillonite." *Applied Clay Science*.

Tournassat, C., Davis, J. A., Chiaberge, C., Grangeon, S., and Bourg, I. C. (2016). "Modeling the acid-base properties of montmorillonite edge surfaces." *Environmental Science and Technology*.

Towler, B. W., Rupp, C. J., Cunningham, A. L. B., and Stoodley, P. (2003). "Viscoelastic Properties of a Mixed Culture Biofilm from Rheometer Creep Analysis." *Biofouling*.

Tran, D., and Strom, K. (2019). "Floc sizes and resuspension rates from fresh deposits: Influences of suspended sediment concentration, turbulence, and deposition time." *Estuarine, Coastal and Shelf Science*, Elsevier Ltd, 229(September), 106397.

Trefalt, G., Behrens, S. H., and Borkovec, M. (2016). "Charge Regulation in the Electrical Double Layer: Ion Adsorption and Surface Interactions." *Langmuir*.

Vaezi G., F., Sanders, R. S., and Masliyah, J. H. (2011a). "Flocculation kinetics and aggregate structure of kaolinite mixtures in laminar tube flow." *Journal of Colloid and Interface Science*.

Vaezi G., F., Sanders, R. S., and Masliyah, J. H. (2011b). "Flocculation kinetics and aggregate structure of kaolinite mixtures in laminar tube flow." *Journal of Colloid and Interface Science*, Elsevier Inc., 355(1), 96–105.

Verwey, E. J. W., and J. T. G. Overbeek. (1955). "Theory of the stability of lyophobic colloids." *J. Colloid Interface Sci.*, 10(5), 224–225.

Viallat, A., and Abkarian, M. (2014). "Red blood cell: From its mechanics to its motion in shear flow." *International Journal of Laboratory Hematology*.

Vinogradov, A. M., Winston, M., Rupp, C. J., and Stoodley, P. (2004). " Rheology of biofilms formed from the dental plaque pathogen Streptococcus mutans ." *Biofilms*.

Walling, D. E., and Moorehead, P. W. (1989). "The particle size characteristics of fluvial suspended sediment: an overview." *Hydrobiologia*.

Wan, Q., Rao, F., Song, S., García, R. E., Estrella, R. M., Patiño, C. L., & Zhang, Y. (2017). "Geopolymerization reaction, microstructure and simulation of metakaolin-based geopolymers at extended Si/Al ratios.pdf." *Cement and Concrete Composites*, 79, 45.

Wand, M. P. (1997). "Data-Based Choice of Histogram Bin Width." *American Statistician*.

Wang, S., Zhang, L., Yan, B., Xu, H., Liu, Q., and Zeng, H. (2015a). "Molecular and surface interactions between polymer flocculant chitosan g polyacrylamide and kaolinite particles: Impact of salinity." *Journal of Physical Chemistry C*.

Wang, Y., Dan, W., Xu, Y., and Xi, Y. (2015b). "Fractal and morphological characteristics of single marble particle crushing in uniaxial compression tests." *Advances in Materials Science and Engineering*, 2015.

Wang, Z., Nan, J., Ji, X., and Yang, Y. (2018). "Effect of the micro-flocculation stage on the flocculation/sedimentation process: The role of shear rate." *Science of the Total Environment*, Elsevier B.V., 633, 1183–1191.

Weber, K., Sohr, R., Schulz, B., Fleischhacker, M., and Ruhnke, M. (2008). "Secretion of E,E-farnesol and biofilm formation in eight different Candida species." *Antimicrobial Agents and Chemotherapy*.

Wei, H., Gao, B., Ren, J., Li, A., and Yang, H. (2018). "Coagulation/flocculation in dewatering of sludge: A review." *Water Research*, Elsevier Ltd, 143(2015), 608–631.

Weibull, W. (1939). "A statistical theory of the strength of materials."

WEIBULL, W. (1951). "A Statistical Distribution Function of Wide Applicability." *Journal of Applied Mechanics*.

Westerhof, R., Buurman, P., Van Griethuysen, C., Ayarza, M., Vilela, L., and Zech, W. (1999). "Aggregation studied by laser diffraction in relation to plowing and liming in the Cerrado region in Brazil." *Geoderma*.

Wilkinson, N., Metaxas, A., Quinney, C., Wickramaratne, S., Reineke, T. M., and Dutcher, C. S. (2018). "pH dependence of bentonite aggregate size and morphology on polymer-clay flocculation." *Colloids and Surfaces A: Physicochemical and Engineering Aspects*.

Wu, M., and Wang, J. (2020). "A DEM investigation on crushing of sand particles containing intrinsic flaws." *Soils and Foundations*, Japanese Geotechnical Society, 60(2), 562–572.

Wu, W. (2001). "Baseline studies of the clay minerals society source clays: Colloid and surface phenomena." *Clays and Clay Minerals*.

Wu, Y., Li, Y., Luo, S., Lu, M., Zhou, N., Wang, D., and Zhang, G. (2020). "Multiscale elastic anisotropy of a shale characterized by cross-scale big data nanoindentation." *International Journal of Rock Mechanics and Mining Sciences*, Elsevier Ltd, 134(February), 104458.

Yang, C. T., Marsooli, R., and Aalami, M. T. (2009). “Evaluation of total load sediment transport formulas using ANN.” *International Journal of Sediment Research*.

Yariv, S., and Cross, H. (1979). “Geochemistry of colloid systems for earth scientists.” *Geochemistry of colloid systems for earth scientists*.

Ye, L., Manning, A. J., and Hsu, T. J. (2020). “Oil-mineral flocculation and settling velocity in saline water.” *Water Research*.

Yeung, A. K. C., and Pelton, R. (1996). “Micromechanics: A new approach to studying the strength and breakup of flocs.” *Journal of Colloid and Interface Science*.

Yin, H. (2013). “Size Kinetics and Mechanics of Clay-biopolymer Flocs.” Louisana State University.

Youn, S. W., and Kang, C. G. (2005). “FEA study on nanodeformation behaviors of amorphous silicon and borosilicate considering tip geometry for pit array fabrication.” *Materials Science and Engineering A*.

Young, S. -L, Martino, M., Kienzle-Sterzer, C., and Torres, J. A. (1994). “Potentiometric titration studies on xanthan solutions.” *Journal of the Science of Food and Agriculture*.

Yu, W. zheng, Gregory, J., Campos, L., and Li, G. (2011). “The role of mixing conditions on floc growth, breakage and re-growth.” *Chemical Engineering Journal*, Elsevier B.V., 171(2), 425–430.

Zhang, G., Germaine, J. T., Martin, R. T., and Whittle, A. J. (2003). “A simple sample-mounting method for random powder X-ray diffraction.” *Clays and Clay Minerals*, 51(2), 218–225.

Zhang, G., Germaine, J. T., Whittle, A. J., and Ladd, C. C. (2004a). “Soil structure of a highly weathered old alluvium.” *Geotechnique*, 54(7), 453–466.

Zhang, G., Germaine, J. T., Whittle, A. J., and Ladd, C. C. (2004b). “Index properties of a highly weathered old alluvium.” *Geotechnique*, 54(7), 441–451.

Zhang, G., Yin, H., and DeGroot, D. (2013a). “Thixotropism of micron-sized saltwater clay flocs.” *Geotechnique Letters*.

Zhang, G., Yin, H., Lei, Z., Reed, A. H., and Furukawa, Y. (2013b). “Effects of exopolymers on particle size distributions of suspended cohesive sediments.” *Journal of Geophysical Research: Oceans*, 118(7), 3473–3489.

Zhang, H., Yang, L., Zang, X., Cheng, S., and Zhang, X. (2019a). “Effect of shear rate on floc characteristics and concentration factors for the harvesting of Chlorella vulgaris using coagulation-flocculation-sedimentation.” *Science of the Total Environment*, Elsevier B.V., 688, 811–817.

Zhang, J., Shen, X., Zhang, Q., Maa, J. P. Y., and Qiao, G. (2019b). “Bimodal particle size distributions of fine-grained cohesive sediments in a settling column with oscillating grids.” *Continental Shelf Research*, Elsevier Ltd, 174(January), 85–94.

Zhang, M., Zhao, M., Zhang, G., El-Korchi, T., and Tao, M. (2017). “A multiscale investigation of reaction kinetics, phase formation, and mechanical properties of metakaolin geopolymers.” *Cement and Concrete Composites*.

Zhang, Q. H., Yan, B., and Wai, O. W. H. (2009). “Fine sediment carrying capacity of combined wave and current flows.” *International Journal of Sediment Research*.

Zhang, Z., Sisk, M. L., Mashmoushy, H., and Thomas, C. R. (1999). “Characterization of the breaking force of latex particle aggregates by micromanipulation.” *Particle and*

Particle Systems Characterization.

Zhao, C. Y., Kim, T., Lu, T. J., and Hodson, H. P. (2004). “Thermal transport in high porosity cellular metal foams.” *Journal of Thermophysics and Heat Transfer*.

Zhao, C., Zhou, J., Yan, Y., Yang, L., Xing, G., Li, H., Wu, P., Wang, M., and Zheng, H. (2021). “Application of coagulation/flocculation in oily wastewater treatment: A review.” *Science of the Total Environment*, Elsevier B.V., 765(xxxx), 142795.

Zheng, J., and Hryciw, R. D. (2016). “Index Void Ratios of Sands from Their Intrinsic Properties.” *Journal of Geotechnical and Geoenvironmental Engineering*.

Zhou, Y., and Franks, G. V. (2006). “Flocculation mechanism induced by cationic polymers investigated by light scattering.” *Langmuir*.